

Electronic Thesis and Dissertation Repository

6-13-2022 10:30 AM

Performance and Ultimate Limit State of Large-Span Soil-Steel Structures

Kareem Embaby, *The University of Western Ontario*

Supervisor: El Naggari, M. Hesham, *The University of Western Ontario*

A thesis submitted in partial fulfillment of the requirements for the Doctor of Philosophy degree in Civil and Environmental Engineering

© Kareem Embaby 2022

Follow this and additional works at: <https://ir.lib.uwo.ca/etd>



Part of the [Civil Engineering Commons](#), [Geotechnical Engineering Commons](#), and the [Structural Engineering Commons](#)

Recommended Citation

Embaby, Kareem, "Performance and Ultimate Limit State of Large-Span Soil-Steel Structures" (2022). *Electronic Thesis and Dissertation Repository*. 8583.
<https://ir.lib.uwo.ca/etd/8583>

This Dissertation/Thesis is brought to you for free and open access by Scholarship@Western. It has been accepted for inclusion in Electronic Thesis and Dissertation Repository by an authorized administrator of Scholarship@Western. For more information, please contact wlsadmin@uwo.ca.

Abstract

This thesis investigates the structural behavior and soil-structure interaction of large-span soil-steel structures utilizing steel plates with the deepest corrugation profile, 500 mm X 237 mm. The world's largest-span soil-steel bridge, with a span of 32.40 m, was constructed using 12 mm thick steel plates with the deepest corrugation profile and was instrumented extensively to monitor the displacements and stress resultants of the steel structure. Lateral reinforcement steel mesh was attached to the steel structure and the ends of the structure were strengthened by circumferential reinforced concrete collars. Three-dimensional (3D) nonlinear finite element (FE) model was conducted and validated by the field measurements at different construction stages. The calculated deformations and stress resultants captured the same trend of the field measurements. The numerical results indicated that two main critical zones of the steel structure, the crown and at the change of arc radii, were observed to experience high axial stresses, which should be considered carefully in the structural design. The numerical results also revealed that the deployed steel mesh reinforcement and concrete collars reduced the induced stress resultants in cut ends and beveled ends of buried structures with up to 50% in comparison to the cases without strengthening elements. Moreover, the effects of modeling technique on the predicted performance and stress resultants were evaluated. The results demonstrated that imprecise numerical simulation could lead to difference in the results up to 60% with the anticipated results causing significant changes in the design of soil-steel structures. Furthermore, 3D FE model was conducted and validated by experimental data obtained from a fully monitored full-scale soil-steel structure with 10.0 m span and subjected to truck loading under service and ultimate loading conditions. The critical stress resultants obtained from the steel structure at ultimate condition were used to evaluate the ultimate limit states provided by different design codes and standards. The results revealed that the ultimate capacity of the SSS was reached without conforming to all ultimate bounds provided by the current design codes. Finally, ultimate limit state function was proposed to account for the structure instability that may occur to the steel structure under ultimate loading condition.

Keywords

long-span culverts, numerical modeling, ultra-deep, strengthening techniques, ultimate limit state, failure test.

Summary for Lay Audience

Soil-steel structures are widely used nowadays as a solution for roadways, waterways and railways overpassing because of their relative low cost and ease of construction compared to conventional concrete and steel bridges. The soil-steel structures are formed of corrugated steel plates with a wide range of sizes and shapes depending on the application. Recently, the world's deepest corrugated profile, with a total depth of 237 mm, has been developed to achieve large spans up to 32 m. Current design guidelines for these large-span special-featured structures require comprehensive computational techniques to specifically simulate different structural elements and the soil-structure interaction. The current study proposes guidelines and recommendations for simulating large-span soil-steel structures having special features that are used to strengthen the buried steel structure. The ultimate capacity of soil-steel structures is also investigated under the effect of maximum backfill height and topmost live loading. The performance of the steel structure is compared to the limit states prescribed in current design codes and standards. The results revealed that the current ultimate limit state requires additional parameters to account for the structure instability that may occur to the steel structure under ultimate loading condition. The current research proposes an ultimate limit state function that predicted failure in the steel structure under all cases considered in the current analysis before failure occurred in the steel structure.

Co-Authorship Statement

The thesis has been prepared in accordance with the regulations for an Integrated article format thesis stipulated by the School of Graduate and Postdoctoral Studies at the University of Western Ontario. The full-scale instrumentation and monitoring program for the world's largest-span soil-steel structure was performed by ViaCon. The raw data collected from the data acquisition system during the testing program as well as the field and laboratory testing of the soil were provided by Atlantic Industries Ltd. (AIL). All the work involved in this study including; processing of the raw data, analyzing the field and laboratory soil tests, experimental data interpretation and numerical modeling was performed by the author alone under the direct supervision of Dr. El Naggar.

Publications resulted from this study were drafted by the author; supervised, reviewed and edited by Dr. El Naggar; and reviewed by Dr. El Sharnouby. The following is a list of publications published and under review:

- 1- **Embaby K.**, El Naggar H., El Sharnouby M. "Performance of large-span arched soil-steel bridges under soil loading" *Thin-Walled Structures*. Vol. 172 – March 2022 (Chapter 3)
- 2- **Embaby K.**, El Naggar H., El Sharnouby M. "Response Evaluation of Soil-Steel Bridges to Truck Loading" *International Journal of Geomechanics*. Vol. 21, Issue 10 – October 2021 (Chapter 5).
- 3- **Embaby K.**, El Naggar H., El Sharnouby M. "Investigation of Beveled-Ended Large-Span Soil-Steel Structures". **Under review in Engineering Structures** (Chapter 4)
- 4- **Embaby K.**, El Naggar H., El Sharnouby M. "Ultimate Capacity of Large-Span Soil-Steel Structures". **Under review in Tunnelling and Underground Space Technology** (Chapter 6)

Acknowledgments

First and foremost, thanks to God for his many graces and blessings.

I wish to express my deepest gratitude and appreciation to my supervisor Prof. Hesham El Naggar. I would like to thank him for his continuous support and guidance throughout my research project. His expertise and proficiency on the technical side was significant through the research in addition to his encouragement that I was usually seeking. It has been a great privilege and honor to work under his supervision.

I would like also to express my deep appreciation to Dr. Meckkey El Sharnouby for the help and support during my research by sharing the industrial perspective accompanying the research project. The support provided by Atlantic Industries Limited (AIL) through Mitacs accelerate program is also acknowledged with the sincerest gratefulness. ViaCon is also acknowledged for performing the experimental work done in Shamal bridge and sharing the raw data with Atlantic Industries Limited (AIL) to conduct the current research project. I would like also to thank all my colleagues in the department, and specially the geotechnical research center members, for stimulating discussions in different disciplines that enlightened my path, their encouragement and all the fun we had during this period.

Last but certainly not least, I would like to thank my gorgeous wife Haya Salama and my son Zain for the support and patience through the ups and downs, the sleepless nights and hard times throughout this long but rewarding journey. Special thanks to my father, mother and all my family members for their continuous prayers and motivation.

Table of Contents

Abstract.....	ii
Keywords.....	iii
Summary for Lay Audience.....	iv
Co-Authorship Statement.....	v
Acknowledgments.....	vi
Table of Contents.....	vii
List of Tables.....	xi
List of Figures.....	xii
Chapter 1.....	1
Introduction.....	1
1.1 Soil-Steel Structures.....	1
1.2 Research Objectives.....	2
1.3 Scope of Work.....	3
1.4 Thesis Original Contribution.....	4
1.5 Thesis Layout.....	5
1.6 References.....	6
Chapter 2.....	8
Literature Survey.....	8
2.1 Soil-Structure Interaction.....	8
2.2 Configurations of Soil-Steel Structures.....	9
2.3 Corrugated Steel Profiles.....	10
2.4 Strengthening of Soil-Steel Structures.....	10
2.5 Previous Studies.....	12
2.5.1 Service Loading.....	13

2.5.2	Ultimate Loading	19
2.6	Design Codes and Standards.....	21
2.7	Conclusion	24
2.8	References.....	25
Chapter 3	30
	Performance of Large-Span Arched Soil-Steel Structures under Soil Loading	30
3.1	Introduction.....	30
3.2	Description of Field Monitoring Program	34
3.3	Instrumentation Scheme.....	37
3.4	Numerical Modeling.....	37
3.5	Numerical Model Results	43
3.5.1	Structure Deformations.....	44
3.5.2	Axial Stresses.....	45
3.6	Strengthening Techniques.....	48
3.6.1	Circumferential Stiffeners.....	50
3.6.2	Steel Mesh Reinforcement.....	51
3.7	Results and Discussion	54
3.8	Conclusion	58
3.9	References.....	62
Chapter 4	69
	Investigation of Beveled End Large-Span Soil-Steel Structures	69
4.1	Introduction.....	69
4.2	Description of the Bridge.....	71
4.3	Numerical Model Verification.....	74
4.4	Beveled Ended Soil-Steel Structure.....	79

4.5 Results.....	82
4.5.1 Structure Deformations.....	83
4.5.2 Circumferential Stresses	89
4.5.3 Longitudinal Bending Moment.....	90
4.6 Conclusion	92
4.7 References.....	94
Chapter 5.....	99
Response Evaluation of Large-Span Ultra-Deep Soil-Steel Bridges to Truck Loading	99
5.1 Introduction.....	99
5.2 Numerical model validation.....	101
5.2.1 Experimental Details.....	101
5.2.2 Numerical Modeling	103
5.2.3 Results from Validation of Numerical Model	106
5.3 Ultra-Cor soil-steel bridge	110
5.3.1 Numerical Modeling	110
5.3.2 Results.....	112
5.4 Effect of different modeling techniques on predicted response.....	115
5.5 Conclusion	120
5.6 References.....	121
Chapter 6.....	125
Ultimate Capacity of Large-Span Soil-Steel Structures.....	125
6.1 Introduction.....	125
6.2 Numerical Model Validation	127
6.2.1 Experimental Details.....	127
6.2.2 Numerical Modeling	129

6.2.3	Validation Results and Discussion.....	131
6.3	Large-Span Soil-Steel Structure	140
6.3.1	Maximum Flexural Capacity	141
6.3.2	Maximum Backfill Height	144
6.3.3	Maximum Truck Load	150
6.4	Proposed Interaction Equation	154
6.5	Conclusion	157
6.6	References.....	159
Chapter 7	164
Conclusions	164
7.1	Summary	164
7.2	Conclusions.....	165
7.2.1	Service loading.....	165
7.2.2	Ultimate loading.....	169
7.3	Recommendations for Future Research	170
Curriculum Vitae	172

List of Tables

Table 3-1: Summary for soil and structure material properties	43
Table 3-2: Configurations of circumferential stiffeners	51
Table 3-3. Steel mesh reinforcement dimensions in different cases.....	54
Table 4-1: Summary for Soil and Structure material Properties.....	77
Table 5-1: Summary for the Experimental Tests	103
Table 5-2: Summary for Soil and Structure material Properties.....	106
Table 5-3: Summary for the Numerical Tests.....	111
Table 6-1. Summary for Test Scheme	129
Table 6-2. Summary for Soil and Structure Material Properties	131

List of Figures

Fig. 2-1: Large-span soil-steel structure in Grants, New Mexico (after Hahm, 2021)	9
Fig. 2-2: Configurations of soil-steel structures (after CSA, 2019).....	11
Fig. 2-3: Circumferential stiffeners for buried steel structures (a) additional steel beam (Contech, 2017); (b) additional corrugated steel plates (Beben 2020)	12
Fig. 3-1: Transverse section for Shamal bridge (all dimensions in mm) (modified from AIL, 2019).....	36
Fig. 3-2: Photo of the Shamal bridge after construction (Courtesy of AIL, 2019).....	36
Fig. 3-3: Surveying points and strain gauge locations on (a) transverse section; (b) longitudinal section; (c) typical monitoring point (all dimensions in mm) (modified from AIL, 2019).....	38
Fig. 3-4: Numerical model details and dimensions.....	42
Fig. 3-5: Three-dimensional view for arched steel structures and surrounding structural elements	42
Fig. 3-6: Deformed shape for the western structure (scaled up 10 times) (a) half rise of structure; (b) at peaking condition; (c) at final phase	46
Fig. 3-7: Axial stress distribution at peaking condition (a) crest; and (b) valley	47
Fig. 3-8: Axial stress distribution at final stage (a) crest; and (b) valley	48
Fig. 3-9: Three-dimensional view for the numerical model	50
Fig. 3-10: Stiffened angle ribs on the top surface of arched structure (a) CSS-1; (b) CSS-2; (c) CSS-3; (d) CSS-4.....	52
Fig. 3-11: Three-dimensional view for the numerical model including steel mesh reinforcement	54
Fig. 3-12: Deformed shape for the steel structure using steel mesh reinforcement (scaled up 20 times) (a) at Peaking Condition; (b) at Final Phase.....	56
Fig. 3-13: Deformed shape for the steel structure using different SM configurations and CSS (scaled up 20 times) (a) at Peaking Condition; (b) at Final Phase.....	58
Fig. 3-14: Backfill lateral stresses at peaking stage for case (a) RM; (b) CSS-4; (c) SMR-7.....	59

Fig. 3-15: Comparison between Maximum Circumferential Stresses in Steel Structure with and without strengthening elements (a) Maximum Tensile Stresses; (b) Maximum Compressive Stresses	60
Fig. 4-1: Front view for the soil-steel bridge and transverse section (all dimensions are in mm).....	73
Fig. 4-2: Surveying points locations on a transverse section	74
Fig. 4-3: Numerical model details and dimensions.....	76
Fig. 4-4: Three-dimensional Model for Shamal Bridge.....	76
Fig. 4-5: Deformed shape for the western structure (scaled up 10 times) (a) at peaking stage; (b) at final stage	78
Fig. 4-6: Three-dimensional view for the numerical model	80
Fig. 4-7: Three-dimensional view for the concrete collar attached to soil-steel structure.....	82
Fig. 4-8: Three-dimensional view for the steel mesh reinforcement	82
Fig. 4-9: Side view of steel structure including investigated cross-sections.....	83
Fig. 4-10: Deformed shape of steel structure at peaking and final stages with 1.5:1 beveled end (scaled up 30 times) (a) RM; (b) CC; (c) SMR	85
Fig. 4-11: Deformed shape of steel structure at peaking and final stages with 2.0:1 beveled end (scaled up 30 times) (a) RM; (b) CC; (c) SMR	86
Fig. 4-12: Deformed shape of steel structure at peaking and final stages with 2.5:1 beveled end (scaled up 30 times) (a) RM; (b) CC; (c) SMR	87
Fig. 4-13: Distribution of maximum deformations at peaking stage in (a) horizontal direction; (b) vertical direction	88
Fig. 4-14: Distribution of maximum deformations at final stage in (a) horizontal direction; (b) vertical direction	89
Fig. 4-15: Distribution of maximum circumferential stresses at final stage	90
Fig. 4-16: Distribution of maximum longitudinal bending moment at final stage	92
Fig. 5-1: Cross section for the test pit	103
Fig. 5-2: Three-dimensional view for the numerical model	105

Fig. 5-3: Experimental data on backfill soil (a) undrained triaxial test; (b) direct shear test.....	105
Fig. 5-4: Applied force vs. vertical displacement for test (a) C1; (b) D1; (c) E1	108
Fig. 5-5: Circumferential bending moment under test (a) C1; (b) D1; (c) E1	109
Fig. 5-6: Three-dimensional view for the numerical model using Ultra-Cor section	111
Fig. 5-7: Vertical stress distribution due to live load	112
Fig. 5-8: Stress resultants variation due to live load (a) axial thrust; (b) bending moment	113
Fig. 5-9: Vertical stress distribution due to live load	114
Fig. 5-10: Vertical stress distribution with Depth.....	114
Fig. 5-11: Percentage difference in axial stresses and deformations for different soil cover heights for (a) modeling interface conditions; (b) consideration of geometric nonlinearity; (c) soil constitutive model; (d) consideration of construction stages	117
Fig. 5-12: Crown vertical deformation under different modeling techniques at different soil cover heights.....	119
Fig. 5-13: Crown axial stresses under different modeling techniques at different soil cover heights at (a) crest; (b) valley.....	120
Fig. 6-1: Cross-section for the test pit.....	129
Fig. 6-2: Three-dimensional view for the numerical model	131
Fig. 6-3: Load-displacement relationship for test (a) E5a; (b) E5b	135
Fig. 6-4: Circumferential stress distribution in case of test E5b at (a) crown ($\zeta=0$); (b) shoulder ($\zeta=4.0$ m)	136
Fig. 6-5: Bending Moment Distribution for test (a) E5a; (b) E5b	139
Fig. 6-6: Axial Thrust Distribution for test (a) E5a; (b) E5b	140
Fig. 6-7: Specimen configuration and test setup (a) front view; (b) side view; (c) three-dimensional numerical model.....	142
Fig. 6-8: Test results (a) load-deflection curve; (b) moment-deflection curve; (c) Von Mises stresses on deformed shape (scaled up 5 times)	144
Fig. 6-9: Three-dimensional numerical model under variable backfill height.....	145

Fig. 6-10: Deflection of soil-steel structure at different backfill heights	146
Fig. 6-11: Vertical arching effect on SSS (a) vertical stress distribution in soil; (b) Af distribution	147
Fig. 6-12: Results from FE model at maximum backfill height; (a) yield points on steel structure; (b) axial thrust diagram; (c) bending moment diagram	149
Fig. 6-13: Three-dimensional numerical model subjected to (a) CL-625 truck; (b) Komatsu 980E-5	151
Fig. 6-14: Axial stresses-wall strength ratios at different cover heights (a) CHBDC; (b) AASHTO	153
Fig. 6-15: Performance of SSS (a) deformed shape; (b) interaction equation based on CHBDC and AASHTO	155
Fig. 6-16: Proposed interaction equation values	157

1 Introduction

1.1 Soil-Steel Structures

Soil-steel structures (SSS) have been used in a wide range of applications for several decades. Many terms are used to define the SSS such as: culverts, soil-steel bridges, buried structures and steel conduits (CSPI, 2017). The performance of SSS depends on the interaction of two main elements: steel structure and surrounding soil. The backfill soil works on distributing its own weight and additional surcharge loads along the periphery of the structure based on soil arching phenomenon (Terzaghi, 1943). Soil arching phenomenon can be defined as the resistance of stiffer zones to the relative deformations that may be encountered by more flexible zones of soil, causing additional stresses on the rigid zones. Accordingly, soil arching phenomenon depends mainly on the relative stiffness of the steel buried structure and the surrounding backfill.

Buried steel structures utilize corrugated steel plates with different corrugation profiles depending on the required axial and flexural strength and stiffness. The performance of short-span SSS utilizing shallow (up to 51 mm depth) and deep (up to 150 mm) corrugated steel plates have been well-characterized by several research studies (CSA, 2019). As the engineering technology advanced and industrial demands increased, the deepest corrugation profile with a total depth of 237 mm, has been developed to withstand large-span SSS and to attain flexural capacity that can sustain significant earth and truck loading (Williams et al., 2012).

Current design codes and standards require refined analysis for large-span SSS with precise numerical simulation for the nonlinear behavior of soil-structure interaction in addition to different strengthening techniques and ends treatments to evaluate the induced stress resultants in the steel structure under different construction phases (e.g. Canadian Highway Bridge Design Code (CSA 2019); American Association of State Highway and Transportation Officials (AASHTO 2019) LRFD Bridge Design specifications; Corrugated Steel Pipe Institute (CSPI 2017) Handbook of Steel Drainage and Highway Construction Products; Swedish Design Method (Pettersson and Sundquist 2014)). Moreover, current design limit states provided by design codes and standards are based on studies of short-span SSS utilizing shallow and deep corrugated steel plates. Based on the fact that the stiffness of the steel structure affects the distribution of stresses, there is a need for investigating the performance of SSS utilizing the deepest corrugation profile under both service and ultimate loading conditions.

1.2 Research Objectives

The performance of large-span SSS utilizing the deepest corrugation profile requires qualitative investigation on the performance of the steel structure under different loading conditions. Furthermore, current design limit states provided by design codes and standards were developed and based on short-span SSS utilizing shallow and deep corrugation profiles. To better understand the behavior of large-span SSS, the following objectives were set for this research:

- i. Evaluate the performance of large-span SSS utilizing the deepest corrugation profile and in the presence of different strengthening elements.

- ii. Investigate the influence of different strengthening techniques on reducing the deformations and induced stress resultants of buried steel structure.
- iii. Explore the performance of large-span SSS at different slopes of beveled-ends and the influence of different strengthening techniques.
- iv. Demonstrate the vertical stress distribution of truck loading along shallow soil cover over large-span SSS.
- v. Quantify the influence of different modeling approaches on predicting the behavior of buried steel structures.
- vi. Assess current design limit states in predicting the ultimate capacity of large-span SSS under different loading conditions.
- vii. Propose design guidelines and recommendations for large-span SSS under ultimate limit state.

1.3 Scope of Work

The current research reports the results of a monitoring program for the world's largest-span SSS constructed in Dubai, UAE, in 2019 (AIL, 2019). The performance of the SSS is evaluated under the effect of soil loading. Three-dimensional nonlinear finite element model is established and validated by the field monitoring results. The validated numerical model is used to evaluate the influence of strengthening techniques. The performance of SSS at beveled ends is investigated and the effect of stiffening elements is demonstrated. Furthermore, a three-dimensional nonlinear finite element model is conducted and validated by experimental results obtained from an instrumented full-scale SSS subjected

to service and ultimate loading conditions (Lougheed, 2008). A parametric study is conducted to evaluate the ultimate capacity of large-span SSS under different loading conditions. Design guidelines are proposed to evaluate the capacity of large-span SSS under different loading conditions.

1.4 Thesis Original Contribution

The performance of the world's largest-span SSS utilizing the deepest corrugated profile is presented for the first time through field monitoring data (AIL, 2019) and numerical results extracted from three-dimensional nonlinear finite element model simulating all soil and structural elements involved in constructing the project. The validated numerical model was used to investigate for the first time the behavior of SSS comprising different end treatment conditions and the ability of different strengthening techniques in stabilizing and controlling the behavior of the buried steel structures is presented through this study. Moreover, the current study presents the influence of several modeling techniques on predicting the performance of large-span SSS as required by current design codes and standards. Finally, the research investigated for the first time the internal behavior and the stability of buried steel structures under ultimate limit state. The advanced numerical investigation for buried steel structures under ultimate loading conditions empowered the research study to provide design guideline and ultimate limit state to be used in evaluating the safety of the utilized corrugated steel section.

1.5 Thesis Layout

The thesis consists of seven chapters that are organized according to the guidelines of the School of Graduate and Postdoctoral Studies of the university of Western Ontario. The description of each chapter is presented below.

Chapter 1 presents a brief description of soil-steel structures and the general motivation and focus of thesis. The chapter also provides the objectives of this research and scope of work for this study.

Chapter 2 reviews the state of the art and practice with respect to large-span SSS. It presents a brief description of design limit states provided in current design codes and standards. The chapter highlights the gap in the current literature and the motivation for the current research.

Chapter 3 presents the instrumentation and monitoring program of the world's largest-span SSS comprising the deepest corrugation profile. A three-dimensional nonlinear finite element model is developed and validated by the measured deformations and axial stresses of the steel structure. It also evaluates the influence of different strengthening techniques on enhancing the performance of buried steel structures.

Chapter 4 describes the validation program of the finite element model for the world's largest-span SSS at the cut ends. The ability of the numerical modeling scheme in simulating the ends of the SSS with concrete collars attached at its ends is elaborated. The chapter also investigates the influence of different slopes at SSS beveled ends, and the effect of different stiffening elements appended at the ends.

Chapter 5 investigates the response of an instrumented full-scale test for a large-span SSS under the effect of truck loading. A three-dimensional nonlinear finite element model is established and validated by the results obtained for different testing configurations. The validated model is used to investigate the performance of large-span SSS utilizing the deepest corrugation profile under the effect of truck loading. Moreover, the validated model is used in demonstrating the effect of incongruous numerical simulation on predicting the performance of the buried steel structure.

Chapter 6 presents a three-dimensional nonlinear finite element model validated by field measurements obtained from large-span SSS subjected to ultimate loading conditions. The validated model is used to investigate the ultimate capacity of large-span SSS utilizing the deepest corrugation profile. A parametric study is conducted considering different earth and truck loading conditions at the ultimate limit state. The parametric study is used to develop design guidelines and recommendation for the ultimate limit state.

Chapter 7 summarizes the main conclusions drawn from the previous chapters, and provides some recommendations for future studies

1.6 References

- AASHTO (American Association of State Highway and Transportation Officials). 2019. AASHTO LRFD Bridge Design Specification, customary U.S. units, 8th Ed. Washington, D.C.: AASHTO
- Atlantic Industries Limited (AIL). 2019. Personal Communication.

- CHBDC (Canadian Highway Bridge Design Code). 2019. Canadian Standards Association. CAN/CSA-S6-19., Mississauga, ON.: CHBDC
- CSPI (Corrugated Steel Pipe Institute). 2017. Handbook of Steel Drainage and Highway Construction Products, Canadian Edition, Cambridge, ON.: CSPI.
- Evans, C. H. 1984. An examination of arching in granular soils. M.S. thesis. Cambridge, MA, US: Department of Civil Engineering, MIT.
- Loughheed, A. 2008. "Limit states testing of a buried deep-corrugated large-span box culvert." M.S. thesis. Kingston, ON, Canada : Department of Civil Engineering, Queen's University. <http://hdl.handle.net/1974/1663>
- Pettersson L. and H. Sundquist. 2007. "Design of soil-steel composite bridges." TRITA-BKN Rep. No. 112, Royal Institute of Technology, KTH, Stockholm, Sweden.
- Terzaghi, K. 1943. Theoretical soil mechanics. New York, USA: Wiley and Sons. DOI: [10.1002/9780470172766](https://doi.org/10.1002/9780470172766)
- Williams, K., S. Mackinnon and J. Newhook. 2012. New and innovative developments for design and installation of deep corrugated buried flexible steel structures. The 2nd European conference on buried flexible structures. Poznan, Poland

2 Literature Survey

2.1 Soil-Structure Interaction

Several studies were performed to investigate the performance of the buried steel structures and surrounding backfill soil. The interaction between the buried steel structure and surrounding soil is governed by the relative stiffness between soil and structure (Terzaghi, 1943). The mass of soil at the lower stiffness zone tends to yield and deform, while the stiffer zone will oppose this deformation causing additional soil pressure. This phenomenon is called soil arching. The type of soil arching can be distinguished depending on the compressibility of the structure and the surrounding soil (Evans, 1979). The case of structures with higher compressibility relative to the surrounding soil, the soil pressure above the structure is lower than the own weight of the soil prism above the structure, which is so-called “positive soil arching”. On the other hand, if the soil is more compressible than buried structure, the buried structure tends to prevent the deformation of surrounding soil, leading to excess soil pressure above the structure in addition to the own weight of the soil prism above it. This situation is called “negative soil arching”. The same phenomenon occurs with more complex and larger-spans soil-steel structures. Fig. 2-1 shows the ability of large-span soil-steel structure system to support huge earth and mining shovels loads depending on the ability of backfill soil in distributing the applied load along the circumference of the steel structure. The pictured structure was constructed in Grants, New Mexico with a span of 14.3 m and soil cover more than 3.6 m.



Fig. 2-1: Large-span soil-steel structure in Grants, New Mexico (after Hahm, 2021)

2.2 Configurations of Soil-Steel Structures

Soil-steel structures encompass different configurations to be used for different purposes (CSA, 2019). Fig. 2-2 shows different SSS configurations that can be chosen based on several design aspects. The size and configuration of the structure affect the relative stiffness between the steel structure and surrounding soil, which controls the soil arching phenomenon and the distribution of stresses around the buried structure. With the increase of structures' size, open soil-steel structures, such as arched and box, are used more widely in highway and mining projects. However, the current literature lacks quantitative analysis of large-span soil-steel structures performance under both service and ultimate loading conditions.

2.3 Corrugated Steel Profiles

Steel plates are formed in a corrugated profile to increase both axial and flexural stiffness and strength in comparison to flat steel plates. Corrugation profile is named based on its pitch and depth. The pitch is the distance between two consecutive crests, while the depth is the radial distance between crest and valley of the profile. According to ASTM A796/A796M-21 (ASTM), corrugation profiles vary from depth of 6.35 mm up to the recently developed profile of 237 mm depth (Williams et al. 2012). The pitch varies between 38 mm up to 500 mm. The deepest corrugation profile was classified as “Type III deep corrugated structural plate” as per Corrugated Steel Pipe Products (CSPI 2017) and as “Deeper corrugation” as per Canadian Highway Bridge Design Code (CSA 2019).

2.4 Strengthening of Soil-Steel Structures

Several strengthening techniques may be used to increase the capacity of buried steel structures to support surrounding earth and truck loadings. According to existing design codes and recommendations (McGrath et al. 2002; AASHTO 2019; CSA 2019), soil-steel structures can be strengthened using circumferential stiffeners and/or longitudinal stiffeners. Circumferential stiffeners can be placed on the top arch of the structure where large bending moments are initiated during construction to increase the flexural capacity. Circumferential stiffeners can be steel beams or corrugated steel plates bolted to the crest of the main corrugated steel plate as shown in Fig. 2-3. ASTM B864 (ASTM 2019) specifies a list of circumferential stiffeners for aluminum structures and should be extruded from aluminum alloys, but no similar specification are provided for steel structures. On the other hand, longitudinal stiffeners are reinforced concrete beams attached to the shoulders of the structures. The main purpose of the longitudinal stiffeners is to distribute the

construction loads along the total length of the buried structure and to prevent distortion of the structure during construction (McGrath et al. 2002). Maleska et al. (2021) investigated the dynamic performance of Tolpinrud railway tunnel in Norway under the effect of seismic excitations. The study evaluated the influence of different simulation techniques of the corrugated steel plates and the effect of longitudinal reinforced concrete beams in strengthening the buried steel structure. The analysis demonstrated that reinforced concrete longitudinal beams would have a minor effect of on the induced stress resultants and deformations as a result of seismic loadings on the buried steel structure.

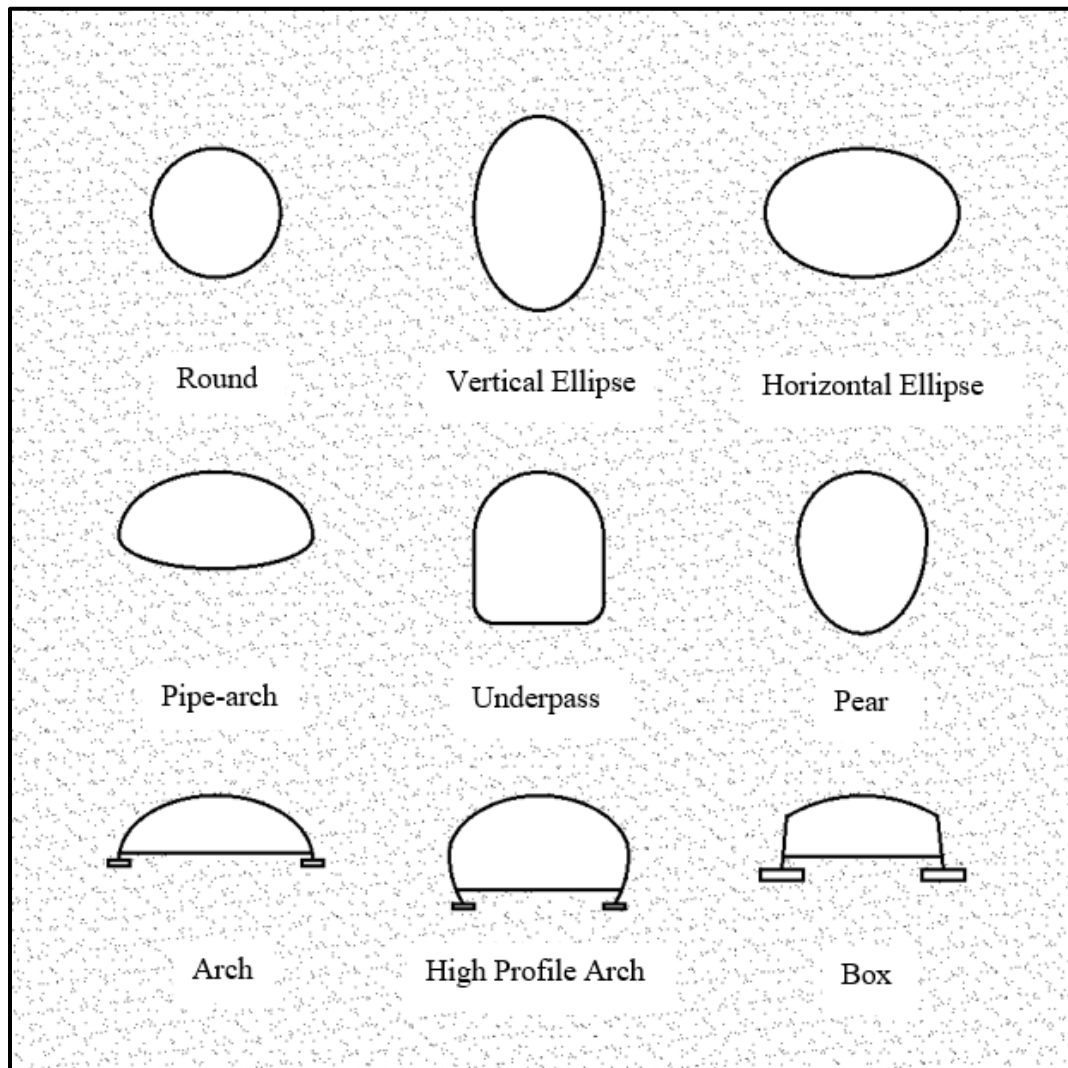


Fig. 2-2: Configurations of soil-steel structures (after CSA, 2019)

2.5 Previous Studies

Several studies evaluated the performance of soil-steel structures under different loading conditions. The research methods adopted in these studies can be categorized into direct and indirect methods. The direct methods include full-scale testing of soil-steel structures under the effect of soil loading, truck loading, train loading, and ultimate loading conditions. The indirect methods involve using different numerical approaches to simulate the soil-structure interaction.

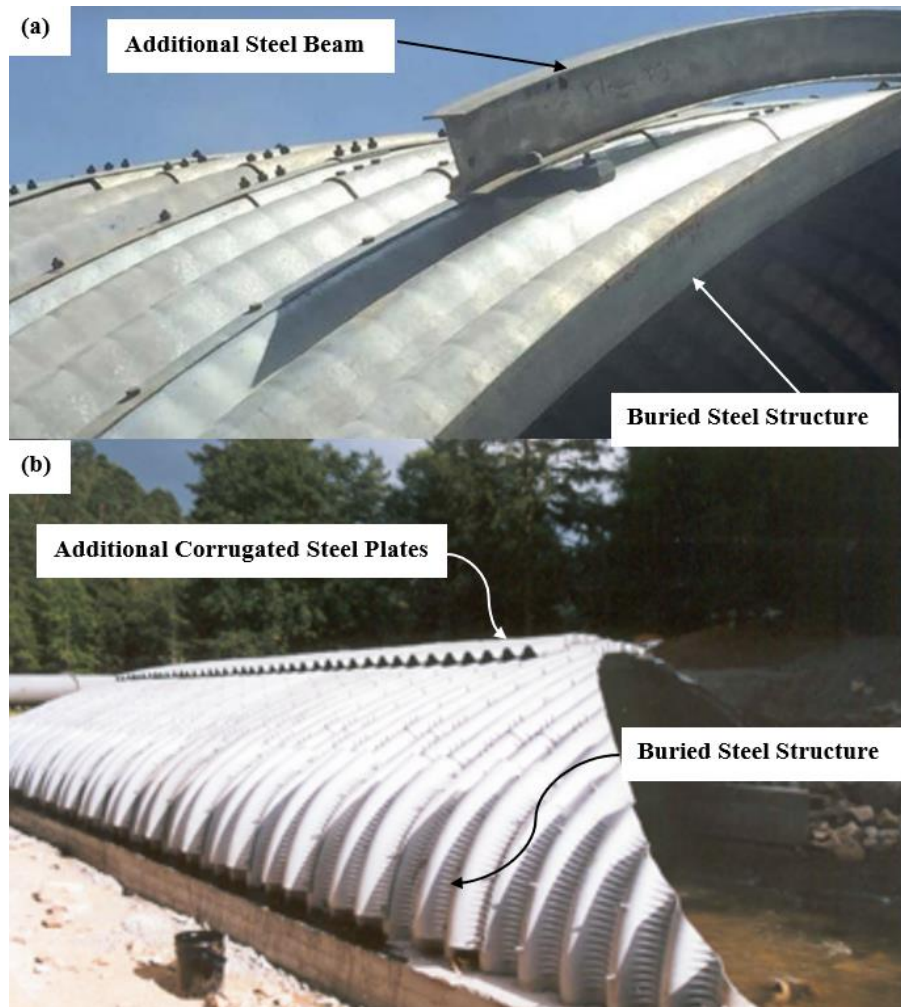


Fig. 2-3: Circumferential stiffeners for buried steel structures (a) additional steel beam (Contech, 2017); (b) additional corrugated steel plates (Beben 2020)

2.5.1 Service Loading

2.5.1.1 Direct methods

A few full-scale studies were conducted to investigate the performance of arched culverts under the effect of earth loads and live loads. Lefebvre et al. (1976) instrumented an arched soil-steel structure with span 15.50 m, 8.0 m rise and 13.40 m high embankment. The structure was founded on a dense glacial till layer overlying stiff bed rock. Squeeze blocks were inserted inside the foundation system in order to reduce the stiffness of the structure with respect to the adjacent soil to permit more displacement to the structure when subjected to the earth loads. Thirty-two pressure cells were installed between the steel structure and the adjacent soil in addition to thirty-five strain gauges welded to the structure. The measurements obtained from the instrumentation showed that the sides of the structure deformed towards the air side of the structure during backfilling around the structure, while the crown of the structure deformed upwards. However, after completing the placement of fill over the structure, the vertical displacement was still lower than the initial deformation. Due to the soil arching, the vertical soil pressure on the structure was only 25% of the overburden pressure. Nevertheless, the lateral soil pressure was greater than the vertical pressure.

Webb et al. (1999) conducted full-scale field tests on a 9.5 m span arched soil-steel structure with no circumferential or longitudinal stiffeners to evaluate the load and resistance factor design specifications. The embankment height above the structure was 1.5 m. The performance of the steel structure was monitored under truck loading placed at different locations and relative densities of the backfill soil. A total of 26 targets were attached to the body of the structure and used for the detailed laser measurements to

evaluate the performance of the structure under different conditions. The results demonstrated that the crown of the structure deformed upwards during backfilling the embankment, then it deformed downwards once the first layer was placed above the structure. The final deformation at the structure crown was 80 mm and 72 mm for both compacted and uncompacted backfill, respectively. The truck load tests demonstrated that the actual soil pressure distribution on the structure body was different than the assumed uniform pressure used in the current design practice. The actual pressure distribution created larger bending moment values that could govern the culvert design. The results also showed that the maximum bending moments due to live load developed at locations outside the tandem axles.

Beben and Manko (2008) investigated the performance of a 10 m span soil-steel structure and 4.02 m rise and total embankment height of 1.30 m above the structure. The soil above the structure was strengthened by a 0.2 m reinforced concrete slab in order to distribute the truck loading on a larger area instead of concentrating the load over the crown of the structure. The strains in the steel structure and the vertical displacements were monitored during the tests. The results demonstrated that the measured displacements were much smaller than the computed displacement using two different numerical models under the same load. This difference was attributed to the fact that the numerical model did not simulate the interface conditions between the reinforced concrete slab and the surrounding soil. In addition, the experimental tests were conducted on the structure after 4 years of being in service.

Lougheed (2008) conducted a full-scale test on a 10.0 m span soil-steel structure. The rise of the steel structure was 2.4 m and the dimensions of the testing pit were 16.0 m wide, 8.0

m long and a total height of 4.0 m. The performance of the steel structure alone (i.e., no backfill soil) was investigated at the beginning by applying two concentrated point loads. Later, the stress resultants and deformations of the steel structure were monitored under the effect of truck loading and plate loading at different backfill heights. A total of twenty loading tests were performed on the soil-steel structure within the serviceability limit range. The study focused on the influence of the cover height on the SSS stiffness. The results demonstrated the nonlinear vertical stress distribution along the soil cover and the dissipation of applied vertical stresses by engaging more soil in the horizontal plane. It was also found that the induced stress resultants in the steel structure in case of single axle loading was higher than the case of tandem axle loading due to engaging more soil around the applied load that facilitated the distribution of the vertical stresses.

Flener (2010a, b) investigated the performance of two soil-steel structures under the effect of soil loading and static truck loading. The two structures had spans of 8.0 m and 14.0 m with rise of 2.4 m and 3.5 m. The structures were divided into two zones in the longitudinal direction. One zone included additional circumferential corrugated steel plates attached at the crown of the steel structure while the other zone had no additional strengthening elements. The study demonstrated the influence of strengthening soil-steel structures with circumferential stiffeners. The results showed that the axial strains and crown vertical deformations were reduced by more than 50% in case of attaching circumferential stiffeners to the steel structure in comparison to the case with no strengthening elements. Moreover, it was found that the measured stress resultants in the steel structure exceeded the design values stated in the design codes such as Canadian Highway Bridge Design

Code (CSA, 2000) and the Swedish design method (Pettersson & Sundquist, 2014). In addition, the measured stress resultants were up to four times the design values.

The first soil-steel bridge constructed utilizing the deepest corrugated profile was located in Newfoundland, Canada with an inside span of 13.30 m and 5.30 m rise (Vallee 2015). The total length of the structure was 55.0 m with mechanically stabilized earth (MSE) walls at both ends of the structure to retain the backfill. The structure performance was monitored during and after construction by attaching strain gauges, thermocouples and deflection prisms at 7 monitoring points along the periphery of the structure. The structure deformations and stress resultants were recorded under soil backfill and truck loading. The measured stress resultants in the steel structure due to earth loading were compared to the design values in CHBDC (CSA, 2006). The results indicated significant difference in the design stress resultants provided by CHBDC in comparison to the measured values. The difference in bending moment and axial thrust values demonstrated that the simplified methods provided by design codes may not be compatible with the soil-steel structures utilizing deepest corrugation profiles.

2.5.1.2 Numerical methods

Several numerical investigations have been conducted to evaluate the influence of soil arching and live load on the culvert performance. However, a few studies investigated the performance of SSS utilizing the deepest corrugated profile. Elshimi et al. (2014) conducted a three-dimensional nonlinear finite element analysis considering a 10 m span and 2.4 m rise deep corrugated arched SSS subjected to a standard truck load. The numerical model was validated utilizing the experimental results obtained by Lougheed (2008). The numerical results agreed with the experimental results, and the difference in

the structure deformations and bending moment at the crown varied between 4% and 17%. The numerical model was then used to investigate the influence of traffic in several traffic lanes on the soil-steel structure. The results showed that two-lanes loading should be considered in the design as it resulted in maximum deformations and bending moment values in the wall of the steel structure. The maximum deformation and bending moment occurred at the crown when two adjacent trucks were located just above the crown. Although placing the two trucks above the shoulder provided higher bending moment and thrust at the shoulder, the difference between the results was less than 10% under the two schemes of loading. Moreover, Elshimi, (2011) investigated the influence of simulating corrugated steel plates using orthotropic plate modeling in comparison to the explicit corrugation modeling. The study demonstrated the ability of orthotropic modeling in capturing the same trend as explicit modeling and field measurements under truck loading conditions with a difference 6-10% of the measured values.

Beben & Stryczek (2016) developed a three-dimensional numerical model to simulate the soil-steel bridge of 10.0 m span and 4.02 m rise below a reinforced concrete relieving slab. The soil-steel structure was subjected to three loading conditions using two heavy trucks at three different locations. The numerical model was validated using the experimental results obtained by Beben & Manko (2008). An equivalent rectangular cross-section was used to simulate both the corrugated profile of the steel structure and the reinforced relieving slab. The backfill soil was modeled as solid elements using Drucker-Prager material model. The results showed that the calculated displacements were higher than the experimental results with a range of 60-71% and the stresses varied by as high as 63%. The numerical model was used to investigate the influence of the relieving slab. The

comparison conditions (with and without the slab) demonstrated that the relieving slab reduced the displacements and stresses of the steel structure. The slab redistributed the truck loads on a larger area that lead to reduction in the stress resultants on the steel cross-sections.

Maleska & Beben (2019) investigated the performance of large-span SSS with a clear span of 17.67 m and vertical rise of 6.05 m. The walls of the steel structure were stiffened by additional corrugated steel plates attached to the circumference of the steel structure. The void between both corrugated steel sections was filled with plain concrete to increase the flexural and axial stiffnesses of the structure. The measured deformations of the steel structure during backfilling stages were used to validate the numerical analysis. A three-dimensional numerical analysis was conducted with simulating the corrugated profile of the steel structure and the circumferential corrugated steel plates. The validated numerical model was used to evaluate the influence of attaching circumferential corrugated steel plates to the steel structure and the case of filling the void between the corrugated steel plates. The results demonstrated significant reduction in the induced stress resultants and deformations (up to 40%) in comparison with the case of no strengthening elements.

Moreover, the performance of the European largest-span soil-steel bridge comprising the deepest corrugation profile was investigated considering the effect of two 4-axle trucks with 32 tons each (Miskiewicz et al. 2020). The span of the bridge was 25.74 m and its rise was nearly 9.0 m. The SSS was simulated numerically using the actual corrugation profile of the steel plates and compared to the measured deformations and axial stresses. The numerical results were in a good agreement with the measured values with a difference less than 5%. However, the material properties of the backfill soil were highly over-estimated,

and the soil was assumed be a linear elastic material. Moreover, the analysis was performed only on the truck loading and neglected the influence of earth loading and the accumulation of axial stresses in the steel structure.

2.5.2 Ultimate Loading

2.5.2.1 Direct methods

Pettersson (2007) investigated the performance of 6.1 m span SSS under the effect of single and tandem axle loading. The performance of the steel structure was evaluated under service and ultimate loading condition. The results of the study were used in proposing design equations for predicting the induced stress resultants in the steel section under the effect of surrounding soil and truck loading. For the case of ultimate loading condition, the maximum applied load was recorded just before the steel structure failed. However, the corrugated steel profile was only 55 mm deep, and the measured stress resultants did not consider the nonlinear distribution of the axial stresses.

Lougheed (2008) assessed the ultimate capacity of a 10.0 m span soil-steel structure under plate loading conditions after investigating the performance of the steel structure under service loading conditions. The structure was subjected to tandem axle loading by applying the load through 0.25 m X 0.6 m bearing plates. The magnitude of the load was increased until bearing capacity failure occurred in the soil cover below the plates before yielding the steel structure at maximum applied load of 800 kN. The loading plates were replaced then by larger size bearing plates with dimensions of 0.37 m X 0.95 m to enforce the steel structure to reach the ultimate limit state. The maximum applied load that the structure sustained was recorded at 1100 kN. The induced bending moment values along the periphery of the structure was recorded at the ultimate limit state and compared to the

expected values according to the CHBDC (CSA, 2014) based on the applied load. The results indicated significant variation between both measured and design bending moment values indicated in the CHBDC. The results also showed that local buckling occurred in the steel cross-section below the loading plates due to the ultimate stress resultants induced in the steel section.

2.5.2.2 Numerical methods

Elshimi (2011) simulated a 10.0 m span soil-steel structure using finite element method under ultimate limit state. The SSS was subjected to tandem axle loading until failure was encountered in the steel structure. The numerical model was validated by the controlled instrumented full-scale test performed by Loughheed (2008). The study demonstrated the significance of considering the corrugation profile in the numerical simulation in addition to the geometric nonlinearity in predicting the ultimate capacity of the soil-steel structure. The results showed that neglecting the geometric nonlinearity could lead to overestimating the ultimate capacity of the soil-steel structure by more than 36%. The propagation of yield zones in the steel structure was also recorded during the loading stages of the structure. Nevertheless, the ultimate induced circumferential stresses were not recorded and compared to the design limit states existing in different design codes and standards.

Wadi et al. (2020) evaluated the ultimate capacity of 18.1 m span SSS numerically under the effect of plate loading. The corrugation profile of the steel plates was 381 mm x 140 mm and the vertical height of the structure was 5.6 m. Three-dimensional and two-dimensional finite element analyses were conducted to indicate the maximum applied plate load the structure can sustain at different locations. The results indicated that the ultimate load decreases as the transverse distance between the crown of the structure and the applied

load increases. It was found that the structure exhibited an asymmetric buckling mode when the applied load was shifted in the transverse direction. The induced stress resultants in the steel structure were recorded just before reaching yield stresses. However, the induced stress resultants at the ultimate conditions were not recorded and were not compared to the limit state equations provided in the design codes.

2.6 Design Codes and Standards

Existing design codes and standards stipulate simplified design procedures for specific cases of soil-steel structures (e.g. Canadian Highway Bridge Design Code (CSA 2019); American Association of State Highway and Transportation Officials (AASHTO 2019) LRFD Bridge Design specifications; Corrugated Steel Pipe Institute (CSPI 2017) Handbook of Steel Drainage and Highway Construction Products; Swedish Design Method (Pettersson and Sundquist 2014)). The simplified design procedures include simplified equations that are used to determine the induced axial thrust and bending moment values in the steel structure. For all other types of buried structures, current design codes require explicit numerical simulation for the SSS and surrounding soil using refined methods such as finite element and finite difference analyses. Rigorous numerical analysis is required to include all construction stages and the accumulation of induced stresses in the steel structure. Moreover, the nonlinear behavior of both steel structure and surrounding backfill soil is also required for the significance on evaluating the performance of the structure.

Based on the calculated stress resultants in the steel structure, either through simplified equations or numerical analysis, the steel structure is designed to satisfy ultimate, serviceability and fatigue limit states. The evaluation of the ultimate limit state for the safety of the structure configuration and its steel cross-section involves an interaction

equation that combines the effects of bending moment and axial thrust. Equation (1) represents the limit state interaction equation required by CHBDC (CSA, 2019); AASHTO (AASHTO, 2019); and CSPI (CSPI, 2017).

$$\left[\frac{N_f}{N_{pf}} \right]^2 + \left[\frac{M_f}{M_{pf}} \right] \leq 1.0 \quad (1)$$

$$N_{pf} = \phi \sigma_y A \quad \& \quad M_{pf} = \phi \sigma_y Z$$

where: M_f is the factored circumferential bending moment in the steel section per unit length in the longitudinal direction; N_f is the factored axial thrust per unit length in the longitudinal direction; M_{pf} is the factored plastic moment capacity of the corrugated steel cross-section; N_{pf} is the factored axial compressive strength of the corrugated steel cross-section without considering buckling mode of failure; ϕ is the plastic hinge for completed steel structure; σ_y is the steel yield stress; A is the corrugated steel cross-sectional area per unit length in the longitudinal direction; Z is the plastic section modulus of the corrugated steel cross-section. The interaction equation of the steel cross-section does not consider the structure instability that may be encountered by in-plane or snap-through buckling modes.

The global buckling failure mode for buried steel structures is evaluated according to CHBDC (CSA, 2019) by following one of the following two equations based on the radius of curvature of the structure wall (Abdel-Sayed, 1978):

$$\text{For } R_{wall} \leq R_e: \quad f_b = \phi_t F_m \left[\sigma_y - \frac{(\sigma_y KR)^2}{12Er^2\rho} \right] \quad (2)$$

$$\text{For } R_{wall} > R_e: \quad f_b = \frac{3\phi_t \sigma F_m E}{\left[\frac{KR}{r} \right]^2} \quad (3)$$

where, R_{wall} is the radius of curvature for the structure wall; R_e is the equivalent radius of the structure; f_b is the maximum compressive stresses in the structure wall; ϕ_t is resistance factor for compressive strength; F_m is a reduction factor for modifying buckling stresses in case of multiple structures; K is a factor representing relative stiffness between structure and surrounding soil; R is the structure rise; E is the modulus of elasticity of the steel material; r is the radius of gyration of the structure wall; and ρ is a reduction factor for buckling stresses.

According to AASHTO (AASHTO, 2019), the global buckling is averted by comparing the factored induced axial stresses by the nominal resistance that the structure could attain using the following equation (Moore, 1994):

$$f_b = \frac{1.2 \phi_b C_n (EI)^{\frac{1}{3}} (\phi_s E_s K_b)^{\frac{2}{3}} R_h}{A} \quad (4)$$

where, ϕ_b is resistance factor for general buckling; C_n is scalar calibration factor for nonlinear effects (0.55); I is moment of inertia for structure wall; ϕ_s is resistance factor for soil; E_s is modulus of elasticity for backfill soil; K_b is factor based on Poisson's ratio; and R_h is a correction factor for backfill geometry.

On the other hand, the Swedish Design Method (Pettersson and Sundquist 2014) stipulates interaction equation for the check against the development of plastic hinges in the steel structure taking in consideration additional parameters, i.e.,:

$$\left[\frac{N_f}{X_y N_{rf}} \right]^2 + \left[k_{yy} \frac{M_f}{M_{rf}} \right] \leq 1.0 \quad (5)$$

$$X_y = \frac{N_{cr}}{N_u} \quad \& \quad k_{yy} = \frac{1.0}{1 - X_y \frac{N_f}{N_{cr,el}}}$$

where: X_y is a reduction factor for flexural buckling; N_{cr} is the critical buckling load per unit length in the longitudinal direction; $N_u = N_p$ is the axial compressive strength per unit length in the longitudinal direction; $N_{rf} = N_{pf}$ is the factored axial compressive strength of the corrugated steel cross-section; k_{yy} is interaction factor for second order effects of the axial forces on deformed members and depends on the class of the section; $N_{cr,el}$ is the buckling load for buried structure under ideal elastic conditions taking in consideration the relative stiffness between the steel structure and surrounding soil.

2.7 Conclusion

It can be concluded that according to the current literature, the performance of large-span SSS utilizing the deepest corrugation profile requires qualitative investigation on the performance of the steel structure under both service and ultimate loading conditions. Current design codes and standards require precise numerical simulation for special featured soil-steel structures including different strengthening techniques to evaluate the soil-structure interaction and the induced stress resultants in the steel structure under different construction phases. However, limited studies in the present literature were performed to evaluate the influence of different modeling techniques on predicting the stress resultants of the structure. In addition, further studies are required to investigate the behaviour of soil-steel structures with beveled ends and the different supporting systems to retain the steel structure and the surrounding backfill. Moreover, the current design limit states stipulated by design codes and standards require explicit investigation for the case of large-span soil-steel structures. This knowledge gap related large span SSS provide the

motivation to investigate the performance of large-span soil-steel structures and evaluate their ultimate capacity under both earth and truck loading of the steel structure.

2.8 References

- Abdel-Sayed G. 1978. "Stability of flexible conduits embedded in soil." *Canadian Journal of Civil Engineering*. 5. 324-333
- AASHTO (American Association of State Highway and Transportation Officials). 2019. *AASHTO LRFD Bridge Design Specification, customary U.S. units, 7th Ed.* Washington, D.C.: AASHTO
- ASTM A796/A796M – 21. 2021. "Standard Practice for Structural Design of Corrugated Steel Pipe, Pipe-Arches, and Arches for Storm and Sanitary Sewers and Other Buried Applications." ASTM International, West Conshohocken, PA. DOI: 10.1520/A0796_A0796M-21.
- ASTM B864-19. 2019. "Standard Specification for Corrugated Aluminum Box Culverts." ASTM International, West Conshohocken, PA, 2019. DOI: 10.1520/B0864_B0864M-19
- Beben D. 2020. "Soil-steel bridges: Design, Maintenance and Durability." *Geotechnical, Geological and Earthquake Engineering*. 49. Springer.
- Beben, D. and A. Stryczek. 2016. "Numerical analysis of corrugated steel plate bridge with reinforced concrete relieving slab." *Journal of Civil Engineering and Management*, 22 (5), 585-596. DOI: <https://doi.org/10.3846/13923730.2014.914092>

- Beben, D. and Z. Manko. 2008. Static load tests of a corrugated steel plate arch with relieving slab. *Journal of Bridge Engineering*. 13(4), 362-376. [https://doi.org/10.1061/\(ASCE\)1084-0702\(2008\)13:4\(362\)](https://doi.org/10.1061/(ASCE)1084-0702(2008)13:4(362))
- CHBDC (Canadian Highway Bridge Design Code). 2000. “Buried Structures”. Canadian Standards Association. CAN/CSA-S6-00., Mississauga, ON.: CHBDC
- CHBDC (Canadian Highway Bridge Design Code). 2006. “Buried Structures”. Canadian Standards Association. CAN/CSA-S6-06., Mississauga, ON.: CHBDC
- CHBDC (Canadian Highway Bridge Design Code). 2014. Canadian Standards Association. CAN/CSA-S6-14., Mississauga, ON.: CHBDC
- CHBDC (Canadian Highway Bridge Design Code). 2019. Canadian Standards Association. CAN/CSA-S6-19., Mississauga, ON.: CHBDC
- Contech Engineered Solutions. 2014. “BridgeCor Overview”. Contech Engineered Solutions LLC, a QUIKRETE Company. West Chester, US.
- CSPI (Corrugated Steel Pipe Institute). 2017. *Handbook of Steel Drainage and Highway Construction Products, Canadian Edition*, Cambridge, ON.: CSPI.
- Evans, C. H. 1984. An examination of arching in granular soils. M.S. thesis. Cambridge, MA, US: Department of Civil Engineering, MIT.
- Elshimi, T. M. 2011. Three-dimensional nonlinear analysis of deep-corrugated steel culverts. Ph.D. thesis, Kingston, ON, Canada: Department of Civil Engineering. Queen's University.

- Elshimi, T. M., R. W. I. Brachman, and I. D. Moore. 2014. "Effect of truck position and multiple truck loading on response of long-span metal culverts." *Can. Geotech. J.* [dx.doi.org/10.1139/cgj-2013-0176](https://doi.org/10.1139/cgj-2013-0176)
- Flener, E. 2010 (a). "Soil-steel interaction of long-span box-culverts – performance during backfilling." *Journal of Geotechnical and Geoenvironmental Engineering*, 136(6), 823-832. [https://doi.org/10.1061/\(ASCE\)GT.1943-5606.0000287](https://doi.org/10.1061/(ASCE)GT.1943-5606.0000287)
- Flener, E. 2010 (b). "Testing the response of box-type soil-steel structures under static service loads." *Journal of Bridge Engineering*, 15(1), 90-97. [10.1061/\(ASCE\)BE.1943-5592.0000041](https://doi.org/10.1061/(ASCE)BE.1943-5592.0000041)
- Hahm J. 2021. Design Considerations for Using Flexible Buried Bridges in Lieu of Conventional Bridges. PDH Articles. Contech Engineered Solutions
- Lefebvre, G., M. Laliberte, L. Lefebvre, Lafleur J. and C. Fisher. 1976. Measurement of soil arching above a large diameter flexible culvert. *Canadian Geotechnical Journal*. 13(1), 58-71. <https://doi.org/10.1139/t76-006>
- Loughheed, A. 2008. "Limit states testing of a buried deep-corrugated large-span box culvert." M.S. thesis. Kingston, ON, Canada: Department of Civil Engineering, Queen's University. <http://hdl.handle.net/1974/1663>
- Maleska T. and D. Beben. 2019. "Numerical analysis of a soil-steel bridge during backfilling using various shell models." *Engineering Structures*. 196. <https://doi.org/10.1016/j.engstruct.2019.109358>

- Maleska T., D. Beben, J. Nowacka. 2021. “Seismic vulnerability of s soil-steel composite tunnel – Norway Tolpinrud Railway Tunnel Case Study.” *Tunnelling and Underground Space Technology incorporating Trenchless Technology Research*. 110. <https://doi.org/10.1016/j.tust.2020.103808>
- McGrath, T. J., I. D. Moore, E. T. Selig, M. C. Webb and B. Taleb. 2002. *Recommended Specifications for large-span culverts*. National Cooperative Highway Research Program. Washington, D.C.: NCHRP.
- Miskiewicz M., B. Sobczyk, P. Tysiac. 2020. “Non-destructive testing of the longest span soil-steel bridge in eurpoe – field measurements and FEM calculations.” *Materials*. 13, 3652. <http://dx.doi.org/10.3390/ma13163652>
- Moore I.D. 1994. “Three-dimensional response of a shallow buried metal culvert.” 4th International Conference on Short and Medium Span Bridges. Halifax, Nova Scotia, Canada. 95-105.
- Pettersson L. 2007. “Full scale tests and structural evaluation of soil steel flexible culverts with low height of cover.” Ph.D. thesis, Division of Structural Engineering and Bridges, KTH Royal Institute of Technology.
- Pettersson L. and H. Sundquist. 2007. “Design of soil-steel composite bridges.” TRITA-BKN Rep. No. 112, Royal Institute of Technology, KTH, Stockholm, Sweden.

- Pettersson L., H. Sundquist. 2014. “Design of soil steel composite bridges.” Report 112, 5th Edition. Division of Structural Engineering and Bridges, KTH Royal Institute of Technology.
- Terzaghi, K. 1943. Theoretical soil mechanics. New York, USA: Wiley and Sons. DOI: [10.1002/9780470172766](https://doi.org/10.1002/9780470172766)
- Vallee, J. H. F. 2015. Investigation of increased wall stiffness on load effect equations for soil metal structures. M.S. thesis, Halifax, Nova Scotia, Canada; Department of Civil Engineering. Dalhousie University
- Wadi A., L. Pettersson, R. Karoumi. 2020. “On predicting the ultimate capacity of a large-span soil-steel composite bridge.” International Journal of Geosynthetics and Ground Engineering. 6:48. <https://doi.org/10.1007/s40891-020-00232-z>
- Webb, M. C., E. T. Selig, J. A. Sussmann and T. J. McGrath. 1999. Field tests of a large-span metal culvert. Washington, DC: Transportation Research Record: Journal of the Transportation Research Board. 1656(1), 14-24. <https://doi.org/10.3141/1656-03>
- Williams, K., S. Mackinnon and J. Newhook. 2012. New and innovative developments for design and installation of deep corrugated buried flexible steel structures. The 2nd European conference on buried flexible structures. Poznan, Poland

3 Performance of Large-Span Arched Soil-Steel Structures under Soil Loading

3.1 Introduction

Soil-steel structures are widely used nowadays as an efficient solution for roadways and railways overpassing. They offer cost-effective and easy to construct alternative to conventional concrete and steel bridges. Small span arched soil-steel bridges are commonly used for short span bridge applications and their performance is well-characterized. Recently, the world's deepest corrugation profile, with total depth of 237 mm, has been developed to achieve large spans and has been used for applications encompassing spans of up to 32 m. However, the performance of the large-span arched soil-steel bridges, its soil-structure interaction and the distribution of soil stresses on the steel structure surface are yet to be investigated.

Several studies have been performed on buried steel culverts to evaluate their soil-structure interaction behaviour and the distribution of soil pressure on their top and side surfaces. The soil pressure distribution is primarily affected by the relative stiffness of structure to the surrounding soil, which is known as soil arching (Terzaghi, 1943). The soil arching can be either active arching or passive arching depending on the installation method around the culvert and the relative flexibility of the structure and the surrounding soil (Evans 1984). In active arching condition, the settlement of soil adjacent to the culvert is lower than the soil prism above the culvert; and in passive arching the settlement of the adjacent soil is higher than the soil prism above the culvert.

The performance of buried steel culverts is investigated through either direct or indirect methods. The direct methods are based on analyzing instrumented full-scale soil-steel bridges and involved culverts with spans up to 18.15 m and corrugation profiles with total depth less than 140 mm and 380 mm wavelength (Lefebvre et al. 1976; Sargand et al. 1994; Webb et al. 1999; Pettersson 2007; Beben and Manko 2008; Mak et al. 2009; Flener 2010; Wadi et al. 2018; Maleska and Beben 2019; Wysokowski 2021). The influence of the soil arching around steel culverts in addition to the culvert performance due to truck loads were investigated. On the other hand, numerous indirect methods (finite element analysis-based) were conducted to investigate the performance of steel culverts. They included two-dimensional models (Flener 2010; Katona 1978; Macheliski et al. 2006) or three-dimensional models using equivalent orthotropic shell theory (Moore and Brachman 1994; Girges and Abdel-sayed 1995; Moore and Taleb 1999; Beben and Stryczek 2016). Many factors that may affect the performance of arched culverts, including: the impact of truck loads on different types of structures, existence of relieving slab above the crown and relative stiffness of surrounding soil were explored.

A limited number of studies simulated the exact configuration of the steel corrugated profile using isotropic plate behavior (Wadi et al. 2018; Maleska and Beben 2019; El-Sawy 2003; Elshimi et al. 2013; Wadi et al. 2020; Maleska et al. 2021). The influence of the culvert span was investigated under several soil cover heights and it was reported that as the structure span increases, the deformations increase and the total stress resultants for the structure under both soil weight and truck loads increase (Elshimi 2011). However, the maximum span arched soil-steel structure analyzed in existing direct and indirect studies

was 18.15 m, and more studies are still needed to better understand the behaviour of larger spans under the effect of soil loading.

Over the last few decades, the demand on soil-steel bridges increased significantly leading to the development of the world's deepest corrugation profile of 237 mm depth and 500 mm pitch (Williams et al. 2012). This corrugation profile was classified as "Type III deep corrugated structural plate" as per Corrugated Steel Pipe Products (CSPI 2017) and as "Deeper corrugation" as per Canadian Highway Bridge Design Code (CSA 2019). The first soil-steel bridge constructed utilizing the deepest corrugated profile was located in Newfoundland, Canada (Vallee 2015). It had an inside span of 13.30 m and rise of 5.30 m, and it was instrumented to monitor its performance. The bridge was simulated numerically using two-dimensional non-linear finite element analysis and the calculated responses were compared with the measured deformations and stress resultants. However, the numerical model was unable to predict the performance of the steel structure during and after construction. Both axial thrusts and deformations values did not agree with the field measurements. Moreover, the performance of the European largest-span soil-steel bridge comprising the same corrugation profile was inspected under the effect of two 4-axle trucks with 32 tons each (Miskiewicz et al. 2020). The span of the bridge of 25.74 m with a European record and rise of nearly 9.0 m. The performance of the bridge was simulated numerically using the actual corrugation profile of the steel plates. However, the material properties of the backfill soil were highly over-estimated, in addition to the assumption of linearly elastic behavior of the soil. To the best knowledge of the authors of this paper, there is no adequate numerical evaluation for a soil-steel bridge using the deepest corrugated steel plates that successfully predicted the response of the structure.

Many design codes and standards stipulated simplified design procedures for specific cases of soil-steel structures (e.g. Canadian Highway Bridge Design Code (CSA 2019); American Association of State Highway and Transportation Officials (AASHTO 2019) LRFD Bridge Design specifications; Corrugated Steel Pipe Institute (CSPI 2017) Handbook of Steel Drainage and Highway Construction Products; Swedish Design Method (Pettersson and Sundquist 2014)). On the other hand, all other types of buried structures, including large-span arched soil-steel structure and dual radii arched structures, require precise numerical simulation to determine internal forces and deformations during and at the end of construction. Several modeling aspects are obligated in the numerical simulation to represent a conservative behavior of the buried structures (Beben 2020). Embaby et al. (2021) (chapter 5) investigated the influence of different modeling techniques on predicting the performance of buried structures, including: large deformation geometric nonlinearity, stress-dependency nature of backfill, soil-structure interaction and backfilling sequence. However, the current literature lacks utilizing those modeling aspects on a three-dimensional numerical simulation for very large spans buried structures.

The main objective of this research is to evaluate the structural behavior and establish the performance characteristics of very large span soil-steel structures utilizing the deepest corrugation profile as well as their interaction with the surrounding soil mass. In addition, this study demonstrates the effectiveness of proper numerical modeling of large-span soil-steel bridges to reliably analyze and design special featured soil-steel structures as per the code specifications. In order to achieve these objectives, a three-dimensional nonlinear finite element model was developed to simulate the performance of three field-monitored full-scale large span steel arched soil-steel bridges (including the largest arched steel

culvert in the world with a span of 32.4 m) (AIL, 2019). The results from the field monitoring program are used to validate the numerical model, which is then used to evaluate the effectiveness of different strengthening techniques that could be employed to enable the steel structure to withstand high backfill loads over large spans.

3.2 Description of Field Monitoring Program

The Shamal Bridge constructed in Dubai, UAE, in 2019 comprised three large span arched steel structures utilizing the deepest corrugation profile. The spans of these structures were 32.40 m, 32.40 m and 23.76 m. This bridge earned the Guinness World Record for being the world's largest span buried structure. The rise of each structure was 9.57 m with a total length of 12.0 m. The corrugation profiles used for the culverts were 500 mm pitch x 237 mm depth with 12 mm thickness for both western and middle structures and 10 mm thickness for the eastern structure. The soil cover height above the crown was 2.94 m and was strengthened with two layers of woven polyester high strength geotextile. The sides of the structures were braced with 10 mm steel reinforcements bars each 200 mm in the longitudinal direction, connected with 8 mm steel bars each 600 mm in the transverse direction. This reinforcement was buried in the surrounding soil to reduce the lateral deformations of the structure during backfilling. Due to access constraints, the gap between the two large span structures (i.e. Western and middle structures) was filled with a controlled low strength material (i.e. cement-stabilized soil) 5.0 m thick with an average unconfined compressive strength of 8.5 MPa after 7 days. The same material was placed adjacent to the far eastern and western concrete footings instead of backfill soil to increase the stiffness of these zones and reduce the lateral spreading of the foundation system. Fig.3-1 presents the transverse section of the bridge including all three structures and the

surrounding structural elements. Fig. 3-2 displays a photo of the Shamal bridge at the end of construction.

The steel structures were founded on deep foundations comprising 1.0 m diameter reinforced concrete piles with embedded depth ranging between 23.0 m and 26.0 m. The reinforced concrete piles penetrated through 5.0m of medium dense to dense sand followed by 12.0m of very dense sand underlain by loose Gravel. Standard Penetration Tests (SPT) were conducted each 50 cm at the top 3.0 m, then each 1.0 m for the rest of boreholes. The results of SPTs were used to estimate the stiffness and strength parameters of the native soil. Groundwater level was found at 5.0 m below the existing ground surface.

The three structures were backfilled using well-graded sand with gravel (SW), per ASTM D2487-11 (ASTM 2015), A-1-b per ASTM D3282-15 (ASTM 2015), with 4% fines. The particle sizes D_{10} , D_{30} and D_{60} were 0.14, 1.18 and 9.36 mm, respectively. Backfill around the structures was placed in lifts of 30 cm thick layers and then compacted to 95-100% optimum density according to standard proctor test in compliance with the construction requirements of AASHTO LRFD Bridge Design Specifications (AASHTO 2014) and CHBDC (CSA 2014). The bridge was constructed following the embankment installation method with the native ground surface at the top of the foundation system. The backfilling around steel structures commenced concurrently without exceeding 1.5 m difference in backfill heights around each structure at any stage of backfilling.

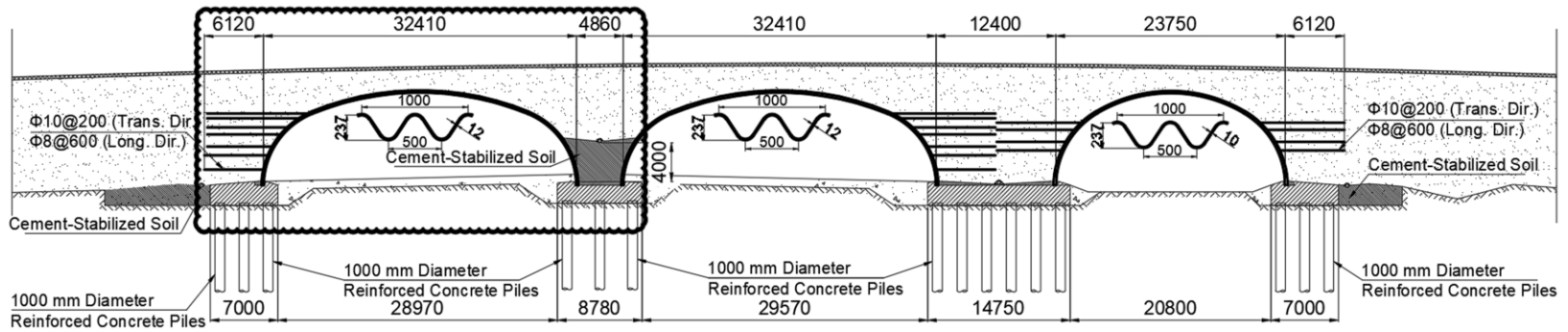


Fig. 3-1: Transverse section for Shamal bridge (all dimensions in mm) (modified from AIL, 2019)



Fig. 3-2: Photo of the Shamal bridge after construction (Courtesy of AIL, 2019)

3.3 Instrumentation Scheme

The performance of the steel body of the bridges was continuously monitored by surveying points located at three transverse sections (each section has 17 points) within each structure using a geodetic laser device as shown in Fig. 3-3. The geodetic laser device was located away from the influence zone of the bridge and directed towards optical prisms attached to the bottom side of the valley. The three-dimensional deformations of the steel structure were evaluated during backfilling based on fixed three reference points between the laser device and the optical prisms. In addition, 34 electro-resistant two-directional strain gauges were attached to the inner side of the western structure at nearly 6.54 m from one end of the bridge (Section 2) to monitor the stress resultants during and after construction under the effect of surrounding soil. At each position, 2 strain gauges were installed to the air side of the steel structure as shown in Fig. 3-3c, one at the crest and one at the valley of the corrugation to evaluate the induced stress resultants in the steel structure. Additional dummy gauges were installed to provide thermal compensation during measurements. These dummy gauges prevent errors due to uneven temperature on both sides of the structure. The monitoring program started just after the installation of the steel structures, thus the response of the structure under its own weight was not monitored.

3.4 Numerical Modeling

Three-dimensional non-linear model was developed using the finite element program Midas GTS NX (2020). Fig. 3-4 shows a strip of 6.0 m simulated with symmetric boundary conditions to represent the total width of the bridge (12.0 m). The model simulated the corrugation profile of the steel culvert using four-noded rectangular shell elements as

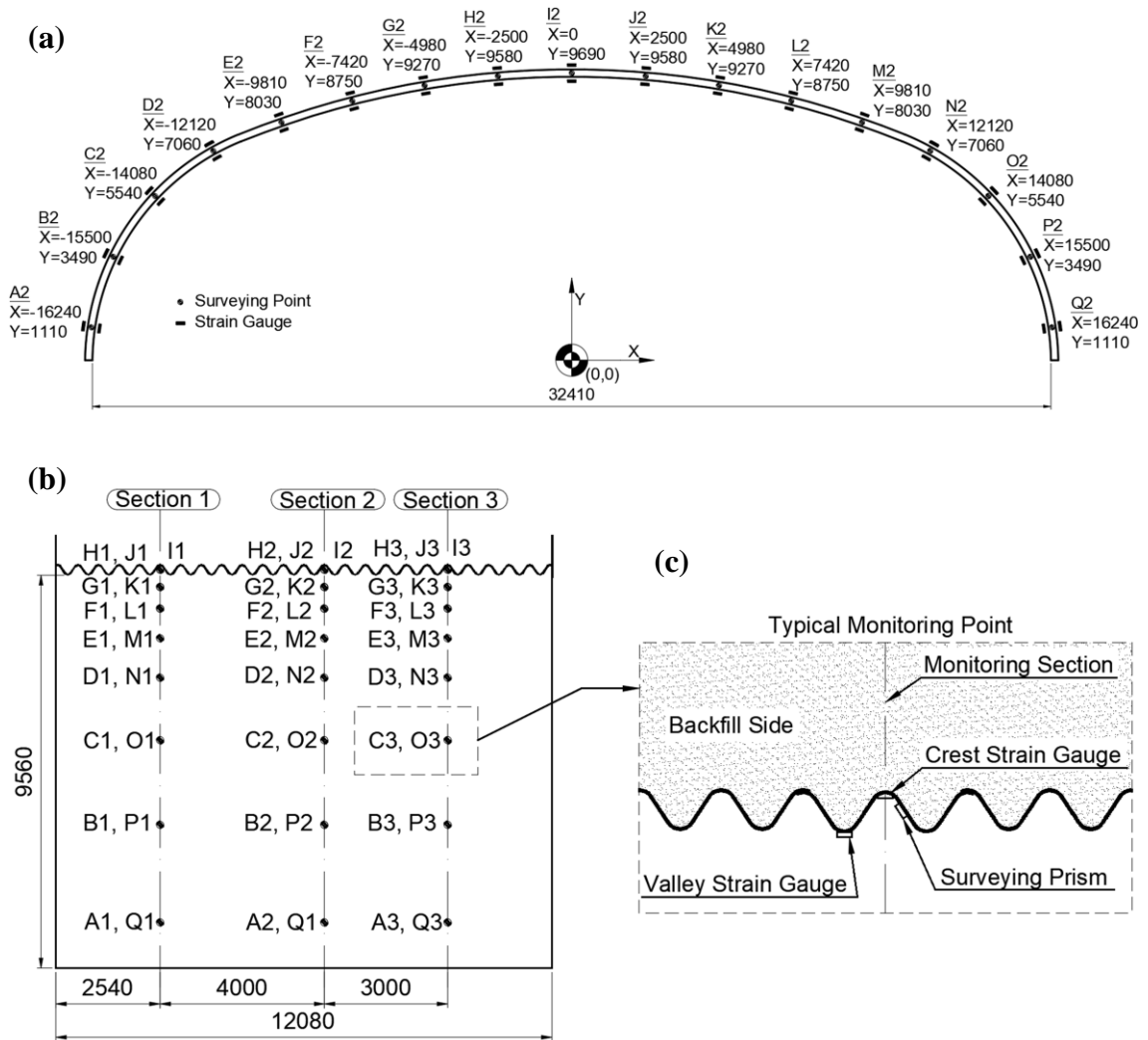


Fig. 3-3: Surveying points and strain gauge locations on (a) transverse section; (b) longitudinal section; (c) typical monitoring point (all dimensions in mm) (modified from AIL, 2019)

shown in Fig. 3-5. Linear elastic-perfectly plastic model with Von-mises failure criterion was used to simulate the steel material behavior. The soil surrounding the steel structures and below the foundation system was simulated using a hybrid mesh of four-noded tetrahedron, six-noded pentahedron and eight-noded hexahedron solid elements.

Modified Mohr-Coulomb failure criterion was used for simulating the performance of the native ground soil and surrounding backfill material. The modified Mohr-Coulomb failure criteria accounts for the non-linear elastic behavior, in addition to shear hardening of friction angle as a function of the plastic shear-strain. Geometric nonlinearity was considered in the current study based on the updated Lagrangian formulation. Linear elastic material model was used for the reinforced concrete piles, footings, cement-stabilized soil and steel mesh around the steel structures. Steel mesh was simulated as two-dimensional three-noded triangular and four-noded rectangular plane-stress elements with equivalent thickness of nearly 0.4 mm. Geogrid elements were not considered in simulating the steel mesh reinforcement as geometric nonlinear large deformations of these elements can not be evaluated in Midas GTS NX. The total number of elements used were 746,870 elements.

Default boundary conditions were used during the analysis of all construction phases of the model (i.e., symmetric boundary conditions at the back side, lateral support at other sides and total fixity at the bottom). The effect of the boundary conditions on the deformations and stress resultants of the steel structures was eliminated by extending the boundaries to more than three times the clear span of the culverts (105 meters) and two times the piles length from the bottom side as shown in Fig. 3-4. In addition, sensitivity analysis was performed to ensure the stability of results at finer element sizes to properly simulate the soil-steel structure performance. The maximum element sizes used for the steel structure was less than 0.25 m (1:128 the span of the bridge). The size of solid elements representing the backfill soil increases gradually from 0.25 m near the steel structure, to 1.0 m away from the influence zone of the structure (1:32 the span of the bridge). Furthermore, the construction stages were analyzed by applying the total backfill

height in 23 construction stages in addition to considering the difference in backfill height around the steel structures for each stage. The first 3.0 m was simulated in 3 construction stages, while the rest of backfill height was divided into less than 0.5 m backfill layers. A uniformly distributed pressure of 34.5 kPa was applied to the surface of each backfill layer to simulate the impact of compaction procedures during construction (Katona 1979; Ezzeldin and Naggar 2021). This distributed pressure is deactivated when activating the next backfill layer and the corresponding compaction load.

Table 3-1 shows the material properties for different elements used in the numerical simulation. The properties of the backfill soil were obtained from internal soil report investigating the backfill soil used in the current project experimentally (Tarmac 2018). Unconsolidated-undrained triaxial compression tests and direct shear tests were conducted on the soil samples to obtain both stiffness and strength parameters. The elastic modulus for the cement-stabilized soil was evaluated from the unconfined compressive strength results after 7 days and the relationship between the relative density and flexural modulus (Gonzalez et al. 2010), i.e.

$$E_{f\ 28\ days} = 1150\sim 1400 * UCS_{28\ days} = 1200 * UCS_{28\ days} \text{(Austroads 2017)} \quad (1)$$

$$UCS_{7\ days} = UCS_{28\ days} * \left[P_1^{1 - \frac{1}{(1 + \frac{t-t_0}{P_2})}} \right] \quad \text{(Wen et al. 2014)} \quad (2)$$

Where, $UCS_{7\ days}$ and $UCS_{28\ days}$ are the unconfined compressive strength after 7 days and 28 days in psi, respectively; t is the time of curing in months (7 days/30.5 days per month); t_0 is time in months for 28 days (28 days/30.5 days per month); P_1 and P_2 are regression parameters (1.59 and 1.61, respectively).

To investigate the influence of relative movement between steel structure, steel mesh reinforcement and surrounding soil in case of existing steel mesh reinforcement attached to the structure, the western soil-steel structure was simulated numerically using two techniques. The first technique involved generating interface elements between steel structure and surrounding soil, in addition to steel mesh reinforcement with lower and upper soil layers using three-noded and four-noded plane interface elements with three-directional translations degrees of freedom and no axial rotation degree of freedom. The material nonlinearity for the interface elements was defined using Coulomb-friction model. The stiffness and strength properties for the interface elements, including the interface friction angle, were taken as a ratio (0.6) of the surrounding soil properties (Midas 2020; Allen et al. 1988). The common nodes between steel mesh reinforcements and steel structure were merged together as the steel mesh is actually attached to the steel structure at different levels. The second technique simulated the same soil-steel structure with steel mesh reinforcement attached to the structure without interface elements (i.e. soil and structure are bonded together, steel mesh and surrounding soil are bonded together, with no relative movement). The techniques yielded very close results in the induced axial stresses in the steel structure with less than 4% difference. Nevertheless, the case of assuming fully bonded steel mesh and structure with the surrounding soil underestimates the upward vertical deformation with less than 0.1% of the rise of the structure. The case of no interface between the steel structure with the surrounding soil; and steel mesh reinforcement with lower and upper soil layers was considered in the current study to achieve convergence of the numerical model. The rigid connections between the steel mesh reinforcement and steel structure prevented the relative deformations between the structure

and surrounding soil at different levels, which resulted in the same structure performance as the case of rigid interface. The connection between the steel structures and the pile caps was simulated as bonded connection by merging the nodes of the structures with those of the pile caps as shown in Fig. 3-5. The rotation of the structure at this connection is transmitted to the footing through vertical deformations along the corrugation profile of the structure.

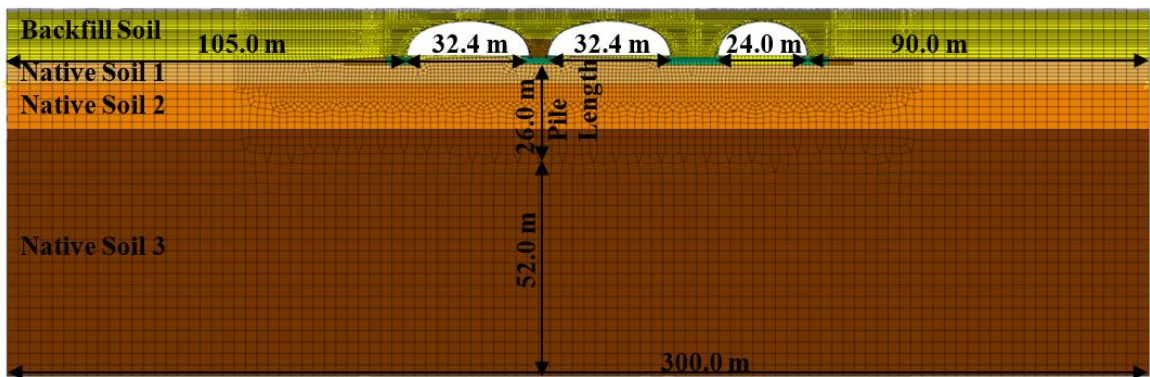


Fig. 3-4: Numerical model details and dimensions

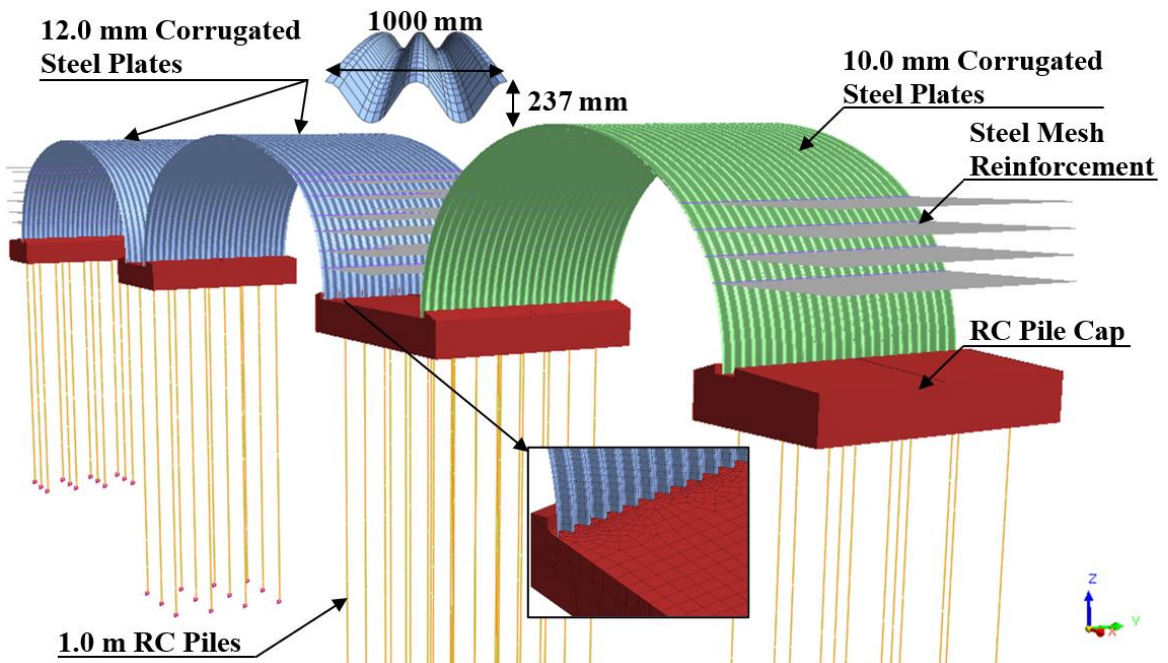


Fig. 3-5: Three-dimensional view for arched steel structures and surrounding structural elements

Table 3-1: Summary for soil and structure material properties

Name	Concrete	Steel	Backfill Soil	Native Soil 1/2/3	Low Strength Material
Material Model Type	Linear Elastic	Von-Mises	Modified Mohr-Coulomb	Modified Mohr-Coulomb	Linear Elastic
Poisson's Ratio	0.2	0.3	0.35	0.3	0.3
Unit Weight (kN/m ³)	23.0	78.5	22.0	21.5	24
Elastic Modulus in Loading (E ₅₀) (MPa)	30000	200000	60	40/60/100	14500
Elastic Modulus in unloading/reloading (E _{ur}) (MPa)	-	-	120	80/120/200	14500
Reference Confining Pressure (kPa)	-	-	100	100	-
Yield Stress (MPa)	-	500	-	-	-
Friction Angle (Degrees)	-	-	43	38/40/45	-
Dilatancy Angle	-	-	6	6/10/10	-
Cohesion (kPa)	-	-	3	2/5/5	-

3.5 Numerical Model Results

The performance of the three steel structures during and after construction was analyzed and compared with the field measurements of displacements and stresses (AIL, 2019). The current study focuses on the behavior of the western structure with span 32.40 m and 12.0 mm thick steel corrugated plates. The numerical results were compared to both deformations and axial stresses obtained from Section 2 (6.54 m from one end) of the western structure. Two main responses occurred during backfilling around the structures. The first response occurred at 9.57 m backfill height, and is referred to as peaking condition. The second response occurred at the final phase of construction, after adding 2.94 m above the crown. The results are then used then to estimate the circumferential bending moments and axial thrust along the structures.

3.5.1 Structure Deformations

The numerical simulation successfully captured the same trend of the steel structure response through all construction stages. The calculated deformations were observed at each stage and compared with the measured deformations. Fig. 3-6 presents the calculated and measured deformations of the structure (scaled up 10 times of the actual deformations) at backfill height of half the rise of structure, peaking condition and final stage. The field measurements reported herein were recorded immediately after installing and compacting the last backfill layer above the structure. The measured and calculated results showed that the case of 5.0 m backfill height did not exhibit significant deformations in the body of the structure. Both measured and calculated responses demonstrated that the maximum upward deformation occurred at 9.57 m backfill height around the structure without any backfill soil above the crown (soil cover). After adding the soil cover above the crown, the structure behaved differently, and the upward deformation decreased gradually and eventually the deformation became downwards.

Furthermore, the numerical model captured the unsymmetrical behavior of the steel structure, which was observed in the field. The unsymmetrical behavior is due to the presence of cement-stabilized soil and the middle steel structure at the eastern side of the analyzed structure, while steel mesh reinforcement was embedded in the surrounding soil at the western side. Meanwhile, the numerical model underestimated both the upward and downward crown vertical deformations during and after construction. However, the differences between calculated and measured vertical deformations were less than 0.4% of the total rise of the structure. The maximum upward and inward vertical deformation of the structure during and after construction were less than 1% of the structure rise, which is

in compliance with the requirements of CHBDC (CSA 2019) code limit of 2%. The decrease in the crown vertical deformation is partly attributed to the presence of steel mesh reinforcement and cement-stabilized soil on both sides of the structure as discussed later in the current study.

3.5.2 Axial Stresses

Circumferential stresses were measured during field testing from attached strain gauges to the bottom face of the steel plates. The circumferential stresses (σ) were evaluated from the generalized Hooke's law based on the plane stress assumption using the following equations:

$$\sigma = \frac{E_s}{(1+\nu)(1-2\nu)} * [\varepsilon_{11}(1 - \nu) + \nu(\varepsilon_{22} + \varepsilon_{33})] \quad (3)$$

$$\varepsilon_{33} = \left[\frac{\nu}{\nu-1}\right](\varepsilon_{11} + \varepsilon_{22}) \quad (4)$$

where, ε_{11} , ε_{22} and ε_{33} are the strains in the element three directions required to obtain the principal stresses; E_s and ν are the steel's young's modulus and Poisson's ratio, respectively. Figs. 3-7 and 3-8 compare the experimental and calculated axial stress distribution along the structure for both crest and valley zones at the peaking and final stages, respectively. The comparison demonstrated that the numerical model correctly captured the same pattern for both crest and valley axial stresses. Two critical zones were observed based on the shown stress distribution that induce maximum tensile and compressive stresses. The first zone is located at the crown as expected, while the second critical zone is located at the shoulders of the structure, 40 degrees from the crown (7.50 m in the horizontal direction). The numerical model captured the location of both critical zones correctly with maximum compressive and tensile axial stresses. During construction,

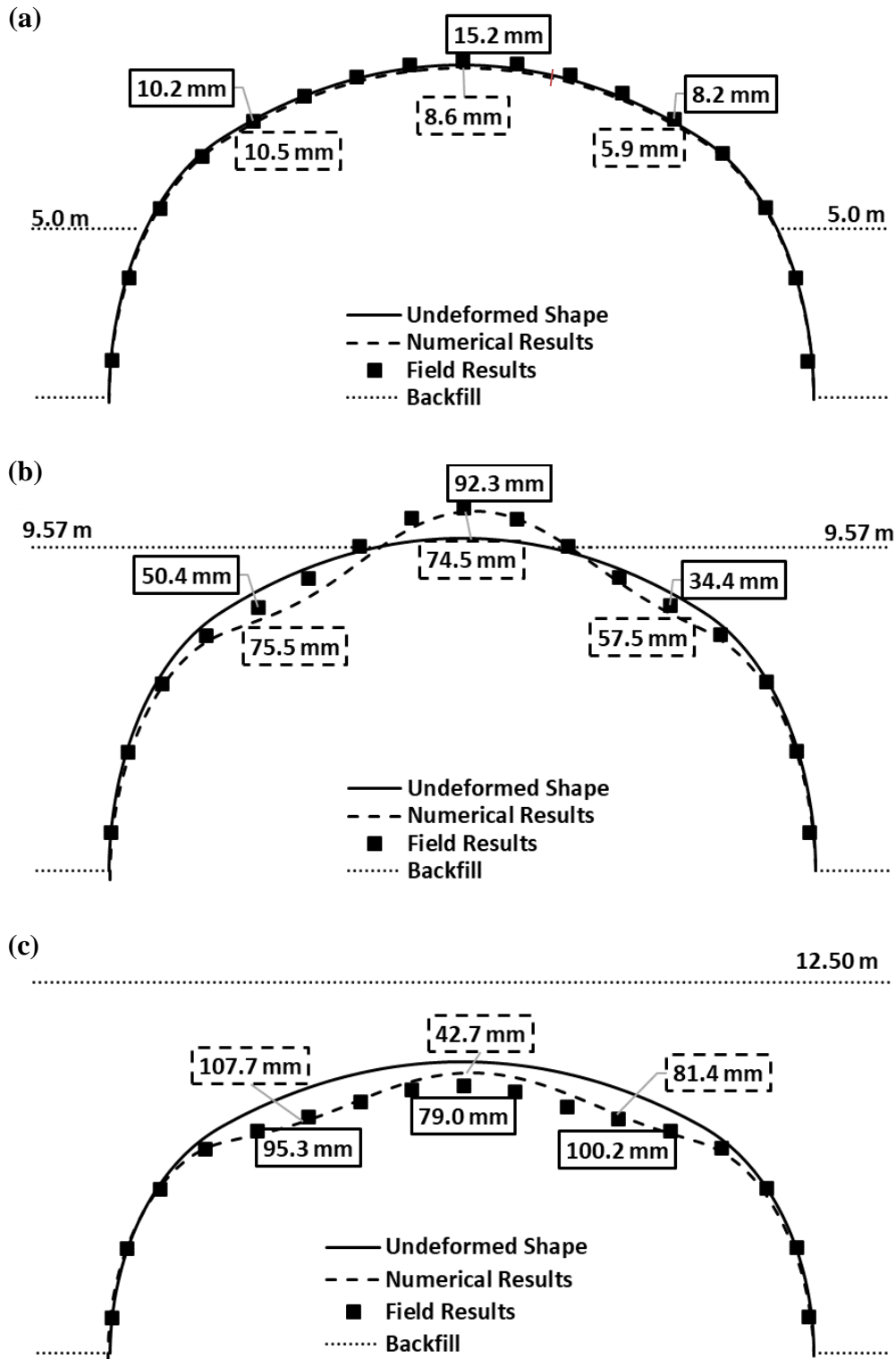


Fig. 3-6: Deformed shape for the western structure (scaled up 10 times) (a) half rise of structure; (b) at peaking condition; (c) at final phase

the maximum tensile stresses occurred at the crest of the crown and at the valley of the shoulders reaching nearly 180 MPa at the maximum peaking condition. The maximum tensile stress decreased gradually as soil cover height increased above the crown and reached nearly zero at the two critical zones by the end of construction. The same two zones experienced the highest compressive stress during construction at the valley of the crown and the crest of the shoulder with maximum stress of 210 MPa.

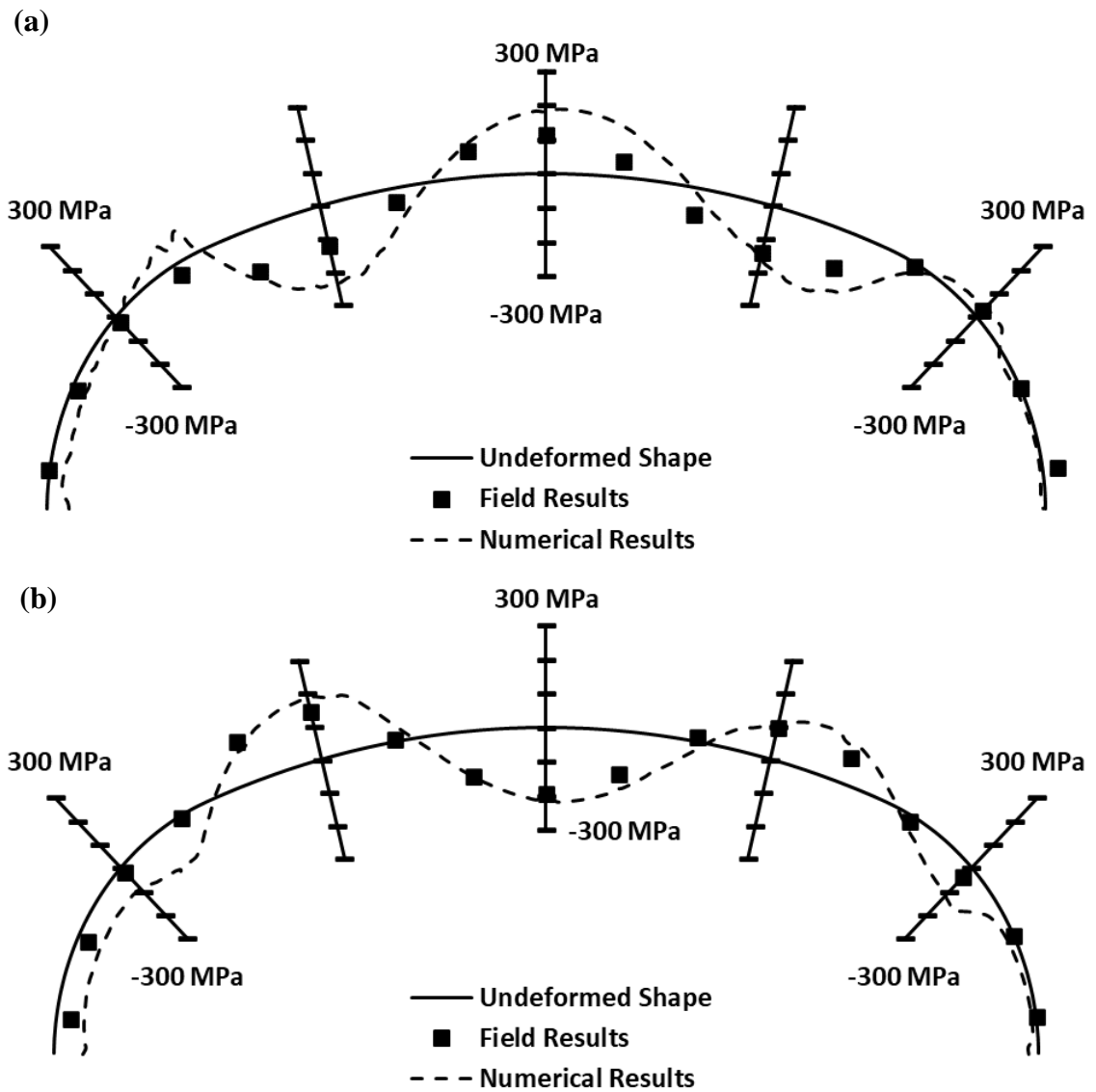


Fig. 3-7: Axial stress distribution at peaking condition (a) crest; and (b) valley

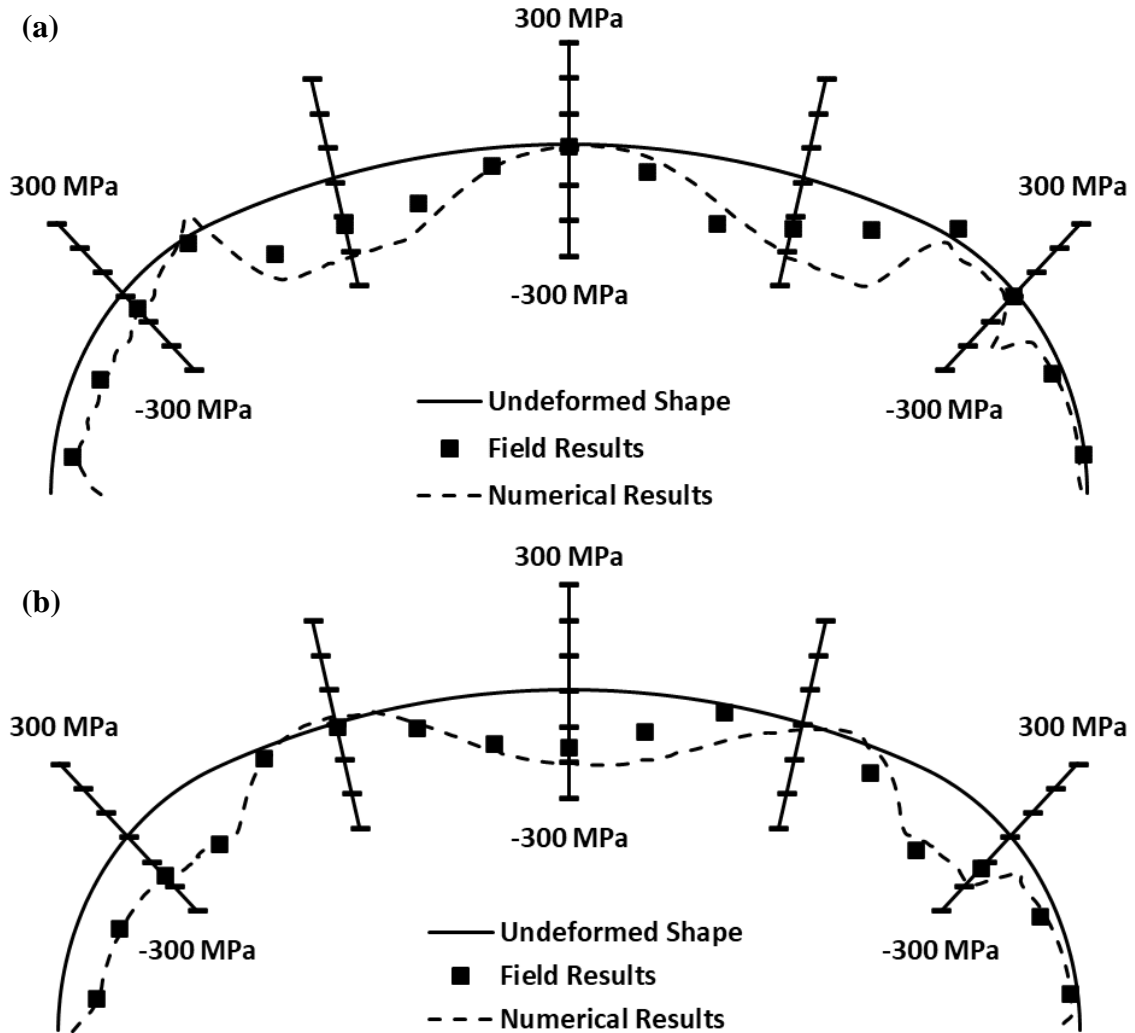


Fig. 3-8: Axial stress distribution at final stage (a) crest; and (b) valley

3.6 Strengthening Techniques

Large-span arched soil-steel structures are subjected to bending moments that may control the design of the steel structure. These bending moment values are attributed to construction loadings and traffic live loads. According to existing design codes and recommendations (McGrath et al. 2002; AASHTO 2019; CSA 2019), large span buried structures can be strengthened using circumferential stiffeners and/or longitudinal stiffeners. Circumferential stiffeners can be placed on the top arch of the structure where

large bending moments are initiated during construction to increase the flexural capacity. Circumferential stiffeners can be steel angles or corrugated steel plates bolted to the crest of the main corrugated steel plate. On the other hand, longitudinal stiffeners are reinforced concrete beams attached to the shoulders of the structures.

The main purpose of the longitudinal stiffeners is to distribute the construction loads along the total length of the buried structure and to prevent distortion of the structure during construction. Maleska et al. (2021) demonstrated the minor effect of reinforced concrete longitudinal beams on the induced stress resultants and deformations as a result of seismic loadings on the buried structures. Corrugated steel ribs and corrugated steel sibs filled with concrete around soil-steel structures showed significant effect on reducing the deformations and axial stress resultants in the buried structures (Maleska and Beben 2019). Nevertheless, the influence of steel-angled circumferential stiffeners in addition to the reinforcement steel mesh in the surrounding soil was not presented in the current literature. Although a list of circumferential stiffeners was proposed through ASTM B864 (ASTM 2019), these stiffeners were specified to aluminum structures and should be extruded from aluminum alloys. The following section demonstrates the influence of circumferential angled steel plates and reinforcement steel mesh on the performance of arched steel structure with the same configuration implemented in Shamal bridge.

Fig. 3-9 shows a three-dimensional nonlinear finite element model without strengthening elements to the steel structure, referred to as Reference Model (RM). A uniformly distributed surcharge load of 34.5 kPa is specified at the top of each backfill layer to simulate the backfill compaction load (Katona 1979; Ezzeldin El Naggar 2021). Von Mises failure criterion and modified Mohr-coulomb failure criterion were used to simulate the

nonlinear behaviour of the steel and soil backfill, respectively. Geometric nonlinearity was employed based on updated Lagrangian formulation to account for the large deformations in the structure. Relative movement was permitted between steel structure and surrounding soil using interface elements with a strength reduction factor of 0.6 (Midas 2020; Allen et al. 1988). The input parameters for the backfill soil and steel elements were considered from Table 3-1. The numerical models used in the current analysis did not consider the influence of the foundation system and the properties of the native ground soil. The current analysis focused only on the influence of each stiffener technique on the performance of the structure, and consequently, provides an indication on how it improves the behavior of the actual structure above the actual site conditions.

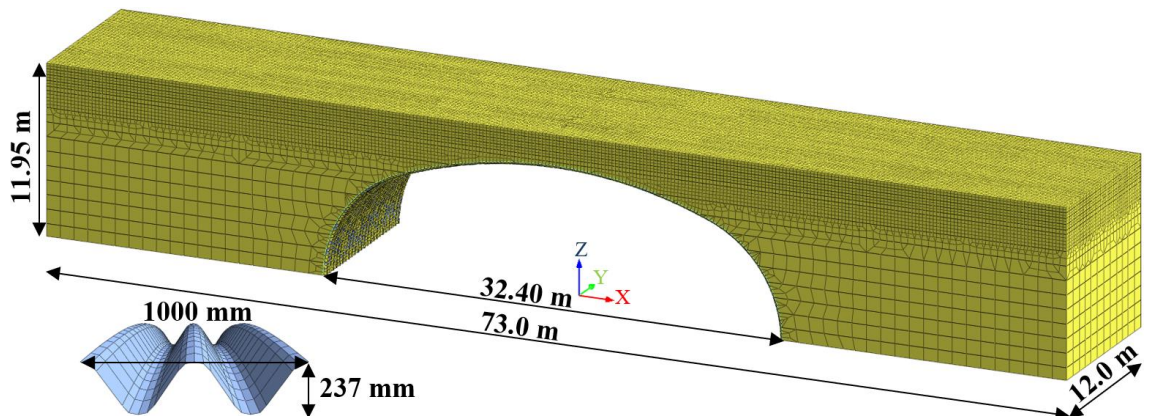


Fig. 3-9: Three-dimensional view for the numerical model

3.6.1 Circumferential Stiffeners

Four different configurations were considered for the case of circumferential stiffeners designated as CSS-1, CSS-2, CSS-3 and CSS-4. The four configurations comprised steel angled ribs attached to the crest of the corrugation and covering the whole circumference of the structure. CSS-1 consists of stiffened ribs of 60 mm X 60 mm with 6 mm thick plates attached to the structure each 1.0 m in the longitudinal direction. CSS-2 considered steel

angles of 120 mm X 60 mm with 6 mm thick plates each 1.0 m. CSS-3 reduced the spacing between the steel ribs to 0.5 m using the same steel angles of 120 mm X 60 mm. Meanwhile, CSS-4 comprised steel angles 150 mm X 60 mm with 0.5 m spacing between each stiffener. Fig. 3-10 and table 3-2 show the configuration of steel stiffeners for each case of strengthening. Beam elements were used in the numerical model to simulate the steel angle stiffeners. The steel angled ribs were assumed fully bonded with the steel structure in the current analysis with no relative deformation permitted that may be encountered in the bolted connections.

Table 3-2: Configurations of circumferential stiffeners

Case	Steel Rib Dimensions (mm)	Spacing (mm)	Second Moment of Area per m ($\times 10^6$) (mm ⁴ /m)
CSS-1	60x60x6	1000	0.23
CSS-2	120x60x6	1000	1.59
CSS-3	120x60x6	500	3.18
CSS-4	150x60x6	500	5.85

3.6.2 Steel Mesh Reinforcement

The steel mesh used in the Shamal bridge was 10 mm steel bars spaced at 200 mm in the longitudinal direction and 8 mm steel bars spaced at 600 mm in the transverse direction. In the numerical models, the reinforcing steel mesh is simulated using plane stress elements with equivalent thickness of nearly 0.4 mm thick. The equivalent thickness was evaluated by maintaining the same axial stiffness as the 10 mm steel bars embedded in the transverse direction, where the transverse direction is considered the strong direction of the steel mesh reinforcement. The steel mesh reinforcement is repeated every 1.0 m in the vertical direction. The numerical models did not consider relative deformation between the steel mesh reinforcement and the surrounding soil for the minor influence encountered for both

deformations and induced stresses in the steel structure as mentioned in the previous sections.

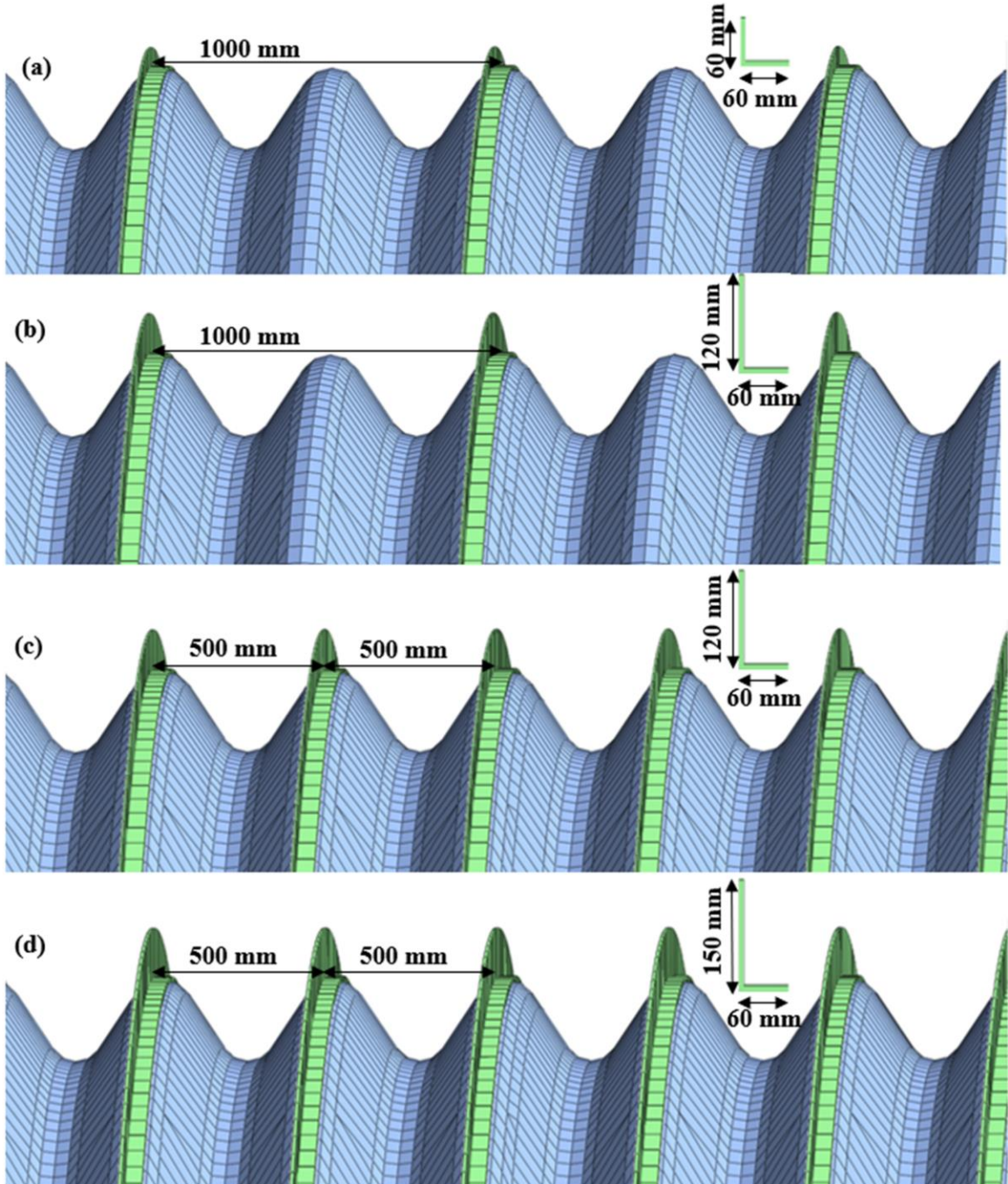


Fig. 3-10: Stiffened angle ribs on the top surface of arched structure (a) CSS-1; (b) CSS-2; (c) CSS-3; (d) CSS-4

To validate the numerical simulation approach of the steel mesh reinforcement as plane stress elements, three comprehensive three-dimensional models were conducted including the exact steel mesh configurations embedded in the backfill soil. The performance of the steel structure calculated using plane stress elements for the steel mesh reinforcement was compared to the case of simulating the exact configuration of the steel mesh. Fig. 3-11 shows the numerical model with the steel mesh configuration embedded in the backfill at different levels. The steel bars were simulated using two-noded beam elements. Three cases were investigated with different longitudinal spacings between transverse steel bars to investigate the feasibility of simplifying various steel mesh configurations employing plane stress elements. The spacing between transverse steel bars was assumed in the three cases as 200 mm; 400 mm; and 800 mm; and the corresponding numerical models comprising plane stress elements had equivalent thicknesses of 0.4 mm; 0.2 mm; and 0.1 mm, respectively. The comparison of the results demonstrated that using plane stress elements could simulate the same structural behaviour as that represented by the exact configuration of steel mesh reinforcement. The difference in deformations and stress resultants between the two modeling approaches was negligible (less than 1%). This small difference is due to the very low relative deformation occurring between the steel mesh and the surrounding soil.

The influence of the steel mesh transverse dimension on the steel structure performance is demonstrated by varying the steel mesh embedded length in the surrounding backfill normalized by the steel rise. In addition, the effect of the spacing between transverse steel bars in the longitudinal direction is investigated. Table 3-3 presents nine different cases for embedded lengths and steel mesh configurations used in the current study. The steel mesh

elements were merged to the steel structure to account for the rigid connection between them and the steel structure.

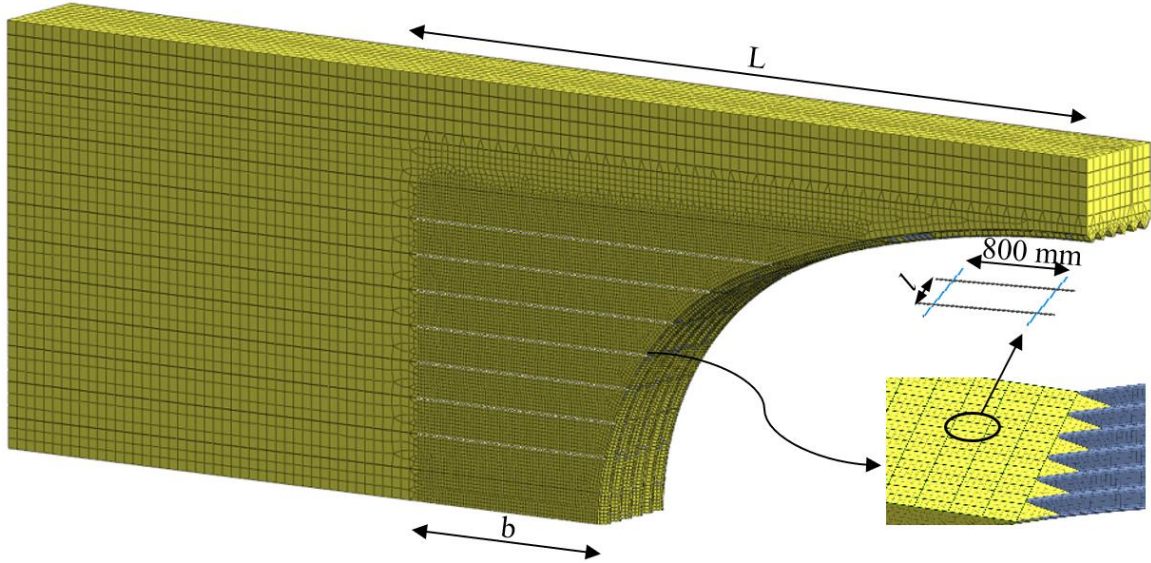


Fig. 3-11: Three-dimensional view for the numerical model including steel mesh reinforcement

Table 3-3. Steel mesh reinforcement dimensions in different cases

Case	Distance from Base (b) (m)	Distance from Crown (L) (m)	L/H	Steel Bars Long. Spacing (<i>l</i>) (mm)
SMR-1	-1.0	15.20	1.59	200
SMR-2	1.0	17.20	1.80	200
SMR-3	3.0	19.20	2.00	200
SMR-4	4.0	20.20	2.11	200
SMR-5	5.0	21.20	2.22	200
SMR-6-a	6.0	22.20	2.32	200
SMR-6-b	6.0	22.20	2.32	400
SMR-6-c	6.0	22.20	2.32	800
SMR-7	7.0	23.20	2.42	200

3.7 Results and Discussion

Fig. 3-12 and 3-13 display the deformed shape of the steel structure for: no strengthening (RM); circumferential stiffeners (CSS); and steel mesh reinforcement (SMR). The

structure deformation was recorded at both peaking stage and final stage. Fig. 3-12 and 3-13 showed that the steel structure in RM case exhibited large lateral deformation at the shoulders in comparison to CSS and SMR. This relatively large lateral deformation led to large upward crown deformation reaching 1.5% of the rise of the steel structure at the peaking stage. However, the ratio between maximum vertical deformation to the structure rise did not exceed 0.5% in case of CSS and SMR. Fig. 3-13 also reveals that as the flexural rigidity of the circumferential stiffeners increased from CSS-1 to CSS-4, the upward crown deformation decreased. Nevertheless, the impact of different steel stiffeners configurations on the structure deformations was not significant. On the other hand, SMR performed better in terms of reducing the upward crown deformation at the peaking stage. However, as the spacing between transverse steel bars increased, the axial stiffness of the steel mesh decreased, leading to excess lateral pressure on the steel structure and an increase in the upward deformation at the peaking phase. The embedment length of SMR controlled the stresses on the steel structure by distributing the lateral stresses of the backfill in the transverse direction. The influence of the SMR was nearly constant as the embedment depth increased to more than 4.0 m inside the backfill.

Fig. 3-14 shows the lateral stress distribution (S_{xx}) in the backfill for the RM, CSS-4 and SMR-7 on the deformed shape scaled up 20 times. The top layer at 9.0 m backfill height exhibited large lateral stresses leading to the upward crown deformation. The maximum lateral stresses were observed in case of RM reaching a value of 230 kPa. In the case of SMR-7, the lateral stresses at the 9th layer did not exceed 130 kPa. This is due to the presence of the steel mesh reinforcement that stabilized the wedge surrounding the steel structure.

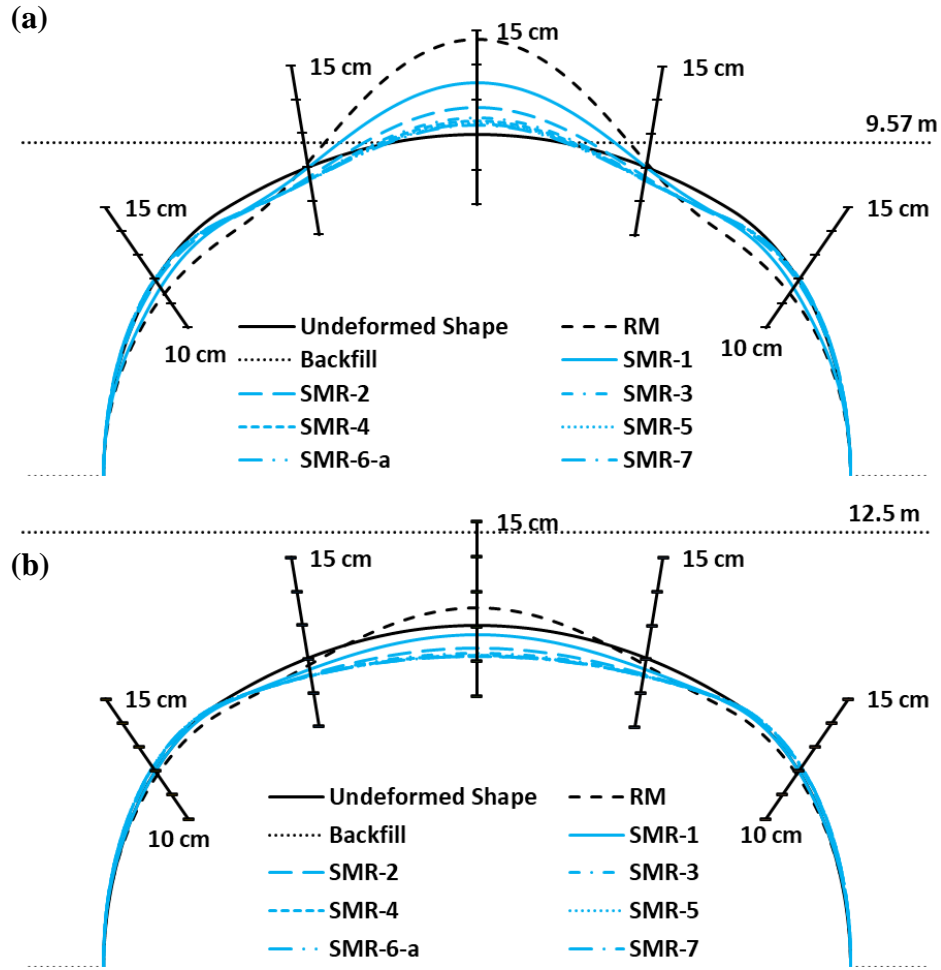


Fig. 3-12: Deformed shape for the steel structure using steel mesh reinforcement (scaled up 20 times) (a) at Peaking Condition; (b) at Final Phase

Fig. 3-15 demonstrates the influence of different strengthening configurations on the axial compressive and tensile stresses in the steel structure. The circumferential stiffeners (CSS) effectiveness in reducing the axial stresses in the steel structure increased noticeably as their flexural rigidity increased. The axial stresses decreased by 4% in both compressive and tensile stresses in case of CSS-1 and decreased by up to 35% in case of CSS-4. The following equations were developed from best-fitting curves with coefficient of

determination (R^2) of nearly 98%, showing the reduction percentage in the circumferential stresses for both peaking and final stages based on the rigidity of the attached stiffeners:

$$R_{CSS,P}(\%) = 2 \times 10^{-13} I_{xx}^2 - 4 \times 10^{-6} I_{xx} - 3.08 \quad (5)$$

$$R_{CSS,F}(\%) = 3 \times 10^{-13} I_{xx}^2 - 7 \times 10^{-6} I_{xx} - 7.63 \quad (6)$$

where, I_{xx} is the second moment of area of the steel stiffener in mm^4 per unit meter. The equations were developed based on the investigated range of second moment of area values presented in table 3-2.

The steel mesh reinforcement (SMR) had higher influence on the axial stresses in the steel structure at the peaking stage in comparison with the final stage. Fig. 3-15 shows that the SMR reduced the axial stresses significantly at the peaking stage in comparison with the CSR. The axial stresses in the steel structure decreased because the embedded depth of the SMR covered the backfill zone above the shoulders of the structure (SMR-1 & SMR-2), resulting in 40% reduction in the axial stresses compared to the RM case. However, as the embedded depth exceeded the base of the structure (i.e., SMR-3 to SMR-7), the influence of the SMR was nearly the same with no additional reduction in the stress resultants of the structure. This demonstrates the effect of the backfill soil above the shoulders of the structure in controlling its performance during construction. The maximum reduction in both compressive and tensile axial stresses in the steel structure was observed in case of SMR-7, which reached 50%. This stress reduction improved the performance of the steel structure up to the end of construction (compressive axial stresses at the final stage was reduced by nearly 20%).

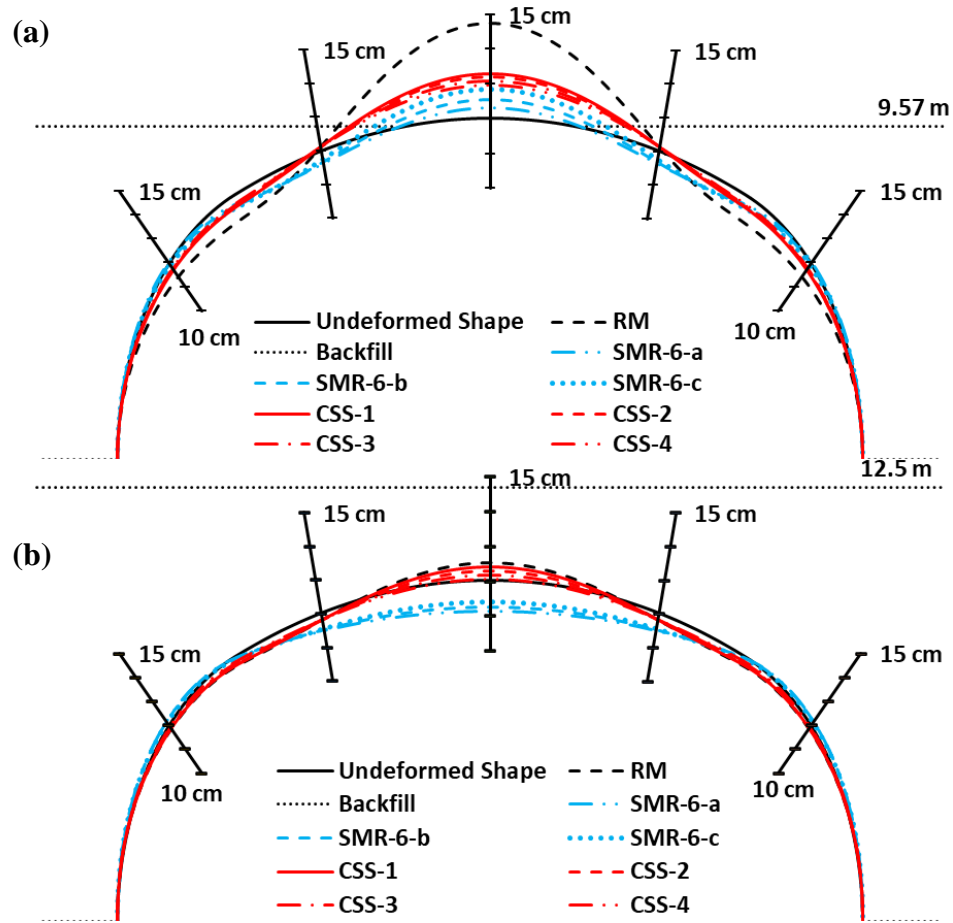


Fig. 3-13: Deformed shape for the steel structure using different SM configurations and CSS (scaled up 20 times) (a) at Peaking Condition; (b) at Final Phase

3.8 Conclusion

The performance of large span arched soil-steel structures using the deepest corrugation profile was investigated for the first time under the impact of surrounding backfill. The world's largest-span arched soil-steel structure with clear span exceeding 32.40 m was used in the current investigation. Monitoring plan consisting of strain gauges and surveying points was followed during construction till the final stage. Three-dimensional non-linear finite element model was used to simulate the behavior of the steel structures and both deformations and axial stresses were compared to the measured data. The following conclusions may be drawn from the presented results:

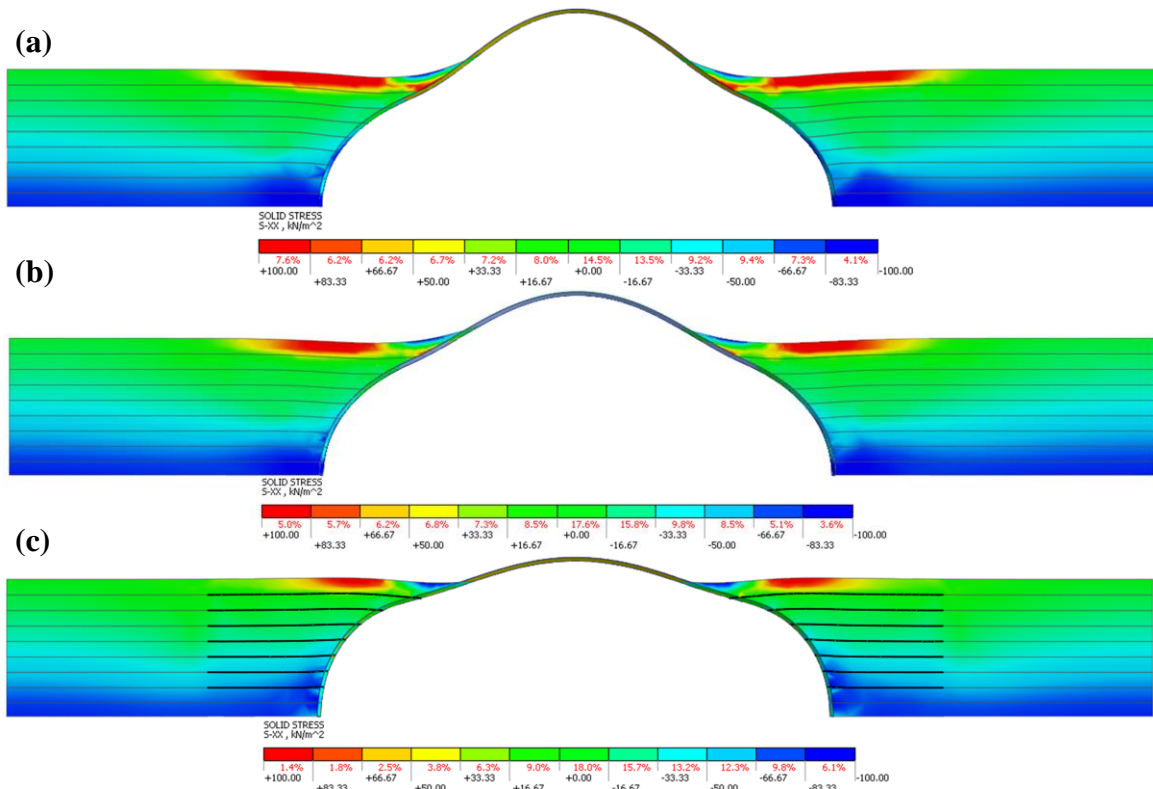


Fig. 3-14: Backfill lateral stresses at peaking stage for case (a) RM; (b) CSS-4; (c) SMR-7

- The field monitoring data demonstrated the capability of the deepest corrugation profile, to safely support the largest span arched soil-steel bridge in the world with clear span of 32.40 meters during and by the end of construction under the effect of soil loading. The study shows possible ways of shape controlling, and together with careful design process, it can be possible to provide soil-steel structures withstanding larger-spans.
- Three-dimensional nonlinear numerical model was conducted using MIDAS GTS NX including the exact configuration of corrugated profile. The numerical model simulated all the structural elements used to support the bridge and both material and geometric nonlinearity were considered in the current

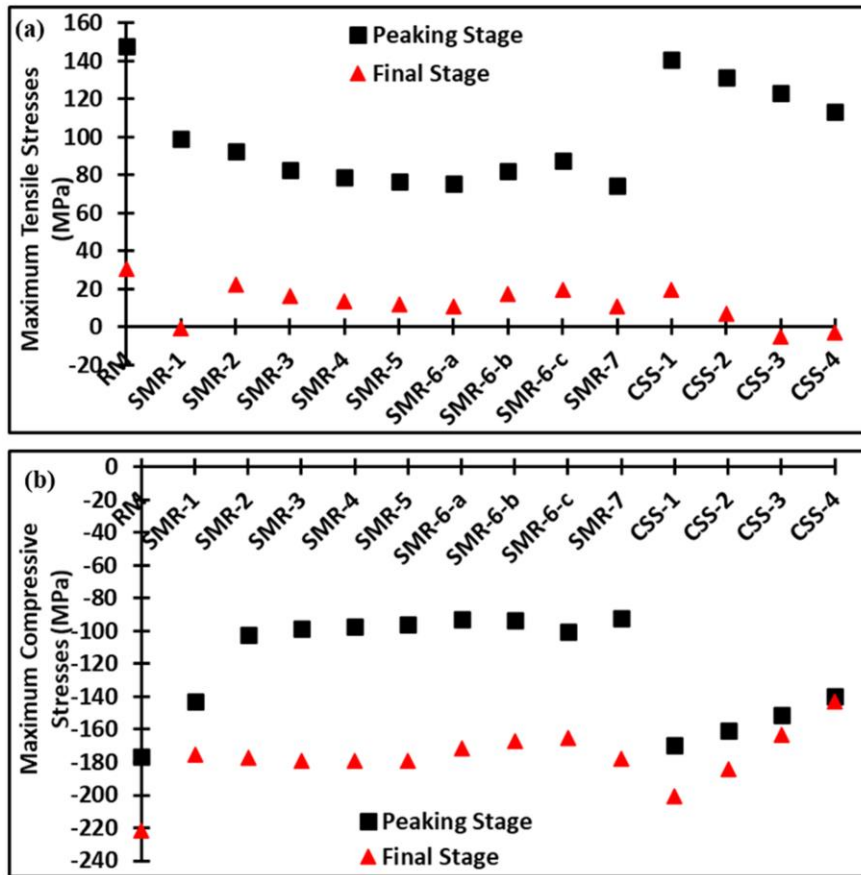


Fig. 3-15: Comparison between Maximum Circumferential Stresses in Steel Structure with and without strengthening elements (a) Maximum Tensile Stresses; (b) Maximum Compressive Stresses

study. The numerical model successfully captured the performance of the structure during and at the end of construction under the impact of surrounding backfill soil.

- Two main critical zones of the steel structure, the crown and at the change of arc radii (40 degrees from the top arc on each side), were observed to experience high axial stresses that may cause the cross-section to yield in addition to global instability and should be carefully considered in the structural design.

- Based on the assumption of considering no relative deformation permitted between steel mesh reinforcement and surrounding soil, it was found that reinforced steel mesh reduced significantly the deformations and stress resultants in the steel structure during and after construction with nearly 50% reduction in the axial compressive stresses at the peaking phase. Nevertheless, the reduction percentage in the upward vertical deformation decreases by increasing the longitudinal spacing of steel bars and decreasing the embedment length in the backfill soil.

- Circumferential steel stiffeners lessen both upward and downward vertical deformation of steel structure with maximum crown deformation less than 0.5% of the structure rise. The reduced vertical deformation is due to the contribution of circumferential steel stiffeners to resisting downward deformations after adding the soil cover above the structure. An equation is proposed to estimate the percentage reduction in the induced axial stresses in steel structure based on the rigidity of the steel stiffeners.

- The results obtained from the conducted numerical analysis and field measurements showed the validity of using steel mesh reinforcement in rigidifying large-span soil-steel structures. It can be concluded also that steel mesh reinforcement can be utilized around buried structures as an alternative strengthening approach to reduce the induced stress resultants in the steel structure during and after construction.

3.9 References

- Atlantic Industries Limited (AIL). 2019. Personal Communication.
- AASHTO (American Association of State Highway and Transportation Officials). 2014. AASHTO LRFD Bridge Design Specification, customary U.S. units. Washington, D.C.: AASHTO
- AASHTO (American Association of State Highway and Transportation Officials). 2019. AASHTO LRFD Bridge Design Specification, customary U.S. units, 7th Ed. Washington, D.C.: AASHTO
- ASTM B864-19. 2019. "Standard Specification for Corrugated Aluminum Box Culverts." ASTM International, West Conshohocken, PA, 2019. DOI: [10.1520/B0864_B0864M-19](https://doi.org/10.1520/B0864_B0864M-19)
- ASTM D2487-11. 2015. "Standard practice for classification of soils for engineering purposes (Unified Soil Classification System)." ASTM International, West Conshohocken, PA. DOI: 10.1520/D2487-11
- ASTM D3282-15. 2015. "Standard practice for classification of soils and soil-aggregate mixtures for highway construction purposes". ASTM International, West Conshohocken, PA. DOI: 10.1520/D3282-15
- Allen R. L., J. M. Duncan, and R. T. Snacio. 1988. "An Engineering Manual for Sheet Pile Walls". Blacksburg, VA: Department of Civil Engineering, Virginia Tech.

- Austroads. 2017. Guide to Pavement Technology: Part 2: Pavement Structural Design. Sydney, Australia: Austroads Ltd.
- Beben D. 2020. “ Soil-steel bridges: Design, Maintenance and Durability.” Geotechnical, Geological and Earthquake Engineering. 49. Springer.
- Beben, D. and Z. Manko. 2008. Static load tests of a corrugated steel plate arch with relieving slab. Journal of Bridge Engineering. 13(4), 362-376. [https://doi.org/10.1061/\(ASCE\)1084-0702\(2008\)13:4\(362\)](https://doi.org/10.1061/(ASCE)1084-0702(2008)13:4(362))
- Beben, D. and A. Stryczek. 2016. "Numerical analysis of corrugated steel plate bridge with reinforced concrete relieving slab." Journal of Civil Engineering and Management, 22 (5), 585-596. DOI: <https://doi.org/10.3846/13923730.2014.914092>
- CHBDC (Canadian Highway Bridge Design Code). 2014. Canadian Standards Association. CAN/CSA-S6-14., Mississauga, ON.: CHBDC
- CHBDC (Canadian Highway Bridge Design Code). 2019. Canadian Standards Association. CAN/CSA-S6-14., Mississauga, ON.: CHBDC
- CSPI (Corrugated Steel Pipe Institute). 2017. Handbook of Steel Drainage and Highway Construction Products, Canadian Edition, Cambridge, ON.: CSPI.
- Elshimi, T. M. 2011. Three-dimensional nonlinear analysis of deep-corrugated steel culverts. Ph.D. thesis, Kingston, ON, Canada: Department of Civil Engineering. Queen's University.

- Elshimi, T. M., R. W. I. Brachman, and I. D. Moore. 2013. "Effect of truck position and multiple truck loading on response of long-span metal culverts." *Can. Geotech. J.* [dx.doi.org/10.1139/cgj-2013-0176](https://doi.org/10.1139/cgj-2013-0176)
- El-Sawy, K. 2003. "Three-dimensional modeling of soil-steel culverts under the effect of truckloads." *Thin-walled Structures*, 41, 747-768. DOI: [https://doi.org/10.1016/S0263-8231\(03\)00022-3](https://doi.org/10.1016/S0263-8231(03)00022-3)
- Embaby, K., H. El Naggar, and M. El Sharnouby. 2021. "Response evaluation of large-span ultra-deep soil-steel bridges to truck loading." *Int. J. Geomech.*, 21(10). [https://doi.org/10.1061/\(ASCE\)GM.1943-5622.0002159](https://doi.org/10.1061/(ASCE)GM.1943-5622.0002159)
- Evans, C. H. 1984. An examination of arching in granular soils. M.S. thesis. Cambridge, MA, US: Department of Civil Engineering, MIT.
- Ezzeldin, I. and H. El Naggar. 2021. Three-dimensional finite element modeling of corrugated metal pipes. *Transportation Geotechnics*. 27. <https://doi.org/10.1016/j.trgeo.2020.100467>
- Flener, E. 2010. Soil-steel interaction of long-span box-culverts – performance during backfilling." *Journal of Geotechnical and Geoenvironmental Engineering*, 136(6), 823-832. [https://doi.org/10.1061/\(ASCE\)GT.1943-5606.0000287](https://doi.org/10.1061/(ASCE)GT.1943-5606.0000287)
- Girges, Y. and G. Abdel-sayed. 1995. "Three-dimensional analysis of soil-steel bridges." *Canadian Journal of Civil Engineering*, 22, 1155-1163. DOI: 10.1139/195-133

- Gonzalez, A., A. Howard, R. D. Carteret. 2010. Cost effective structural treatments for rural highways: cemented materials. Sydney, Australia: Austroads Ltd.
- Katona, M. 1978. "Analysis of long-span culverts by the finite element method." Transportation Research Board 678, Transportation Research Board, Washington D.C. 59-66.
- Katona, M., D. Meinhert, R. Orillac, and C. Lee. 1979. "Structural evaluation of new concepts for long-span culverts and culvert installations." Washington, D.C.: FHWA
- Lefebvre, G., M. Laliberte, L. Lefebvre, Lafleur J. and C. Fisher. 1976. Measurement of soil arching above a large diameter flexible culvert. Canadian Geotechnical Journal. 13(1), 58-71. <https://doi.org/10.1139/t76-006>
- Machelski, C., G. Antoniszyn, B. Michalski. 2006. "Live load effects on a soil-steel bridge founded on elastic supports." Studia Geotechnica et Mechanica, 28, 2-4, 65-82
- Mak, A. C., R. W. I. Brachman, I. D. Moore. 2009. "Measured response of a deeply corrugated box culvert to three dimensional surface loads." In Proc., Transportation Research Board Annual Conference, Washington, D.C.: TRB, 09-3016
- Maleska T. and D. Beben. 2019. "Numerical analysis of a soil-steel bridge during backfilling using various shell models." Engineering Structures. 196. <https://doi.org/10.1016/j.engstruct.2019.109358>

- Maleska T., D. Beben, J. Nowacka. 2021. “Seismic vulnerability of s soil-steel composite tunnel – Norway Tolpinrud Railway Tunnel Case Study.” *Tunnelling and Underground Space Technology incorporating Trenchless Technology Research*. 110. <https://doi.org/10.1016/j.tust.2020.103808>
- McGrath, T. J., I. D. Moore, E. T. Selig, M. C. Webb and B. Taleb. 2002. *Recommended Specifications for large-span culverts*. National Cooperative Highway Research Program. Washington, D.C.: NCHRP.
- Midas GTS-NX. 2020. <https://www.midasoftware.com/geo/gtsnx/products/midasgtsnx>
- Miskiewicz M., B. Sobczyk, P. Tysiac. 2020. “Non-destructive testing of the longest span soil-steel bridge in eurpoe – field measurements and FEM calculations.” *Materials*. 13, 3652. <http://dx.doi.org/10.3390/ma13163652>
- Moore, I. and B. Taleb. 1999. "Metal culvert response to live loading performance of three-dimensional analysis." *Transportation Research Board* 1656, Transportation Research Board, Washington D.C. 37-44
- Moore, I. and R. Brachman. 1994. "Three-dimensional analysis of flexible circular culverts." *Journal of Geotechnical Engineering*, 120 (10), 1829-1844. DOI: [https://doi.org/10.1061/\(ASCE\)0733-9410\(1994\)120:10\(1829\)](https://doi.org/10.1061/(ASCE)0733-9410(1994)120:10(1829))
- Pettersson L. 2007. “Full scale tests and structural evaluation of soil steel flexible culverts with low height of cover.” Ph.D. thesis, Division of Structural Engineering and Bridges, KTH Royal Institute of Technology.

- Pettersson L., H. Sundquist. 2014. "Design of soil steel composite bridges." Report 112, 5th Edition. Division of Structural Engineering and Bridges, KTH Royal Institute of Technology.
- Sargand, S. M., G. A. Hazen, T. Masada. 1994. Long-term field study of a deep-corrugated metal box type culvert. *Canadian Geotechnical Journal*. 31(2), 175-180. <https://doi.org/10.1139/t94-023>
- Tarmac. 2018. "Construction and execution of emirates road at RAK." Project No. R/7078-311906/77/2016. Dubai, UAE
- Terzaghi, K. 1943. *Theoretical soil mechanics*. New York, USA: Wiley and Sons. DOI: 10.1002/9780470172766
- Vallee, J. H. F. 2015. Investigation of increased wall stiffness on load effect equations for soil metal structures. M.S. thesis, Halifax, Nova Scotia, Canada; Department of Civil Engineering. Dalhousie University
- Wadi, A., L. Pettersson, R. Karoumi. 2018. "FEM simulation of a full-scale loading-to-failure test of a corrugated steel culvert." *Steel and Composite Structures*, 27(2), 217-227. 10.12989/scs.2018.27.2.217
- Wadi A., L. Pettersson, R. Karoumi. 2020. "On predicting the ultimate capacity of a large-span soil-steel composite bridge." *International Journal of Geosynthetics and Ground Engineering*. 6:48. <https://doi.org/10.1007/s40891-020-00232-z>

- Webb, M. C., E. T. Selig, J. A. Sussmann and T. J. McGrath. 1999. Field tests of a large-span metal culvert. Washington, DC: Transportation Research Record: Journal of the Transportation Research Board. 1656(1), 14-24. <https://doi.org/10.3141/1656-03>
- Wen, H., B. Muhunthan, J. Wang, X. Li, T. Edil and J. M. Tinjum. 2014. Characterization of cementitously stabilized layers of use in pavement design and analysis. National Cooperative Highway Research Program. Washington, D.C.: NCHRP. DOI: <https://doi.org/10.17226/22247>
- Williams, K., S. Mackinnon and J. Newhook. 2012. New and innovative developments for design and installation of deep corrugated buried flexible steel structures. The 2nd European conference on buried flexible structures. Poznan, Poland

4 Investigation of Beveled End Large-Span Soil-Steel Structures

4.1 Introduction

Soil-steel structures (SSS) are currently used worldwide as an economical alternative solution for underground roadway and waterway networks. Numerous steel corrugated profiles have been investigated in the present literature and their performance is well characterized under different loading conditions. In the last decade, the deepest corrugation profile was introduced with total depth of 237 mm and 500 mm pitch (Williams et al. 2012). The main purpose for developing the Ultra-Cor profile is to withstand very large span soil-steel structures and overpass wider waterways. Large-span SSS may require beveled ends according to different design aspects and site conditions. Nevertheless, the current literature lacks extensive investigation on the performance of large-span SSS comprising beveled ends and supported by different strengthening elements.

The behavior of SSS has been investigated through the current literature under the effect of soil weight and truck loading. Full-scale soil-steel bridges were constructed and evaluated during backfilling and by the end of construction (Lefebvre et al. 1976; Sargand et al. 1993; Webb et al. 1999; Beben and Manko 2008; Mak et al. 2009; Flener 2010). Quantitative studies have been conducted to simulate the SSS performance numerically using either two-dimensional finite element modeling (Katona 1978; Machelski et al. 2006); or three-dimensional modeling (Moore and Brachman 1994; Girges and Abdelsayed 1995; Moore and Taleb 1999; El-Sawy 2003; Beben and Stryczek 2016; Elshimi et al. 2013; Embaby et al. 2021 (Chapter 5)). Nevertheless, the stability of the steel structure

and surrounding soil at the inlets was not investigated in the previous studies and the numerical models were restrained from the lateral deformations perpendicular to the sides.

Tomala and Vegerby-Hanssenn (2017) investigated the performance of a SSS having 28 degrees skew angle and a beveled end of 1V:1.5H (1 vertical to 1.5 horizontal). The structure had span of 4.77 m and 3.83 m rise. The investigation program included three-dimensional FEM model simulating the beveled ends of the steel structure. The results showed large deformations associated with beveling the ends of the structure and additional strengthening elements were required to attain global stability for the SSS. Lateral geogrid was provided to reduce lateral earth pressure in addition to concrete collars to strengthen the flexural capacity of the cut rings. However, the numerical simulation didn't consider the actual configuration of the corrugated steel profile. Moreover, the study lacks a validation program with the full-scale field results.

Maleska and Beben (2019) evaluated the performance of SSS strengthened with circumferential corrugated steel plate and filled with concrete mix. The structure had span of 17.67 m and rise of 6.05 m. The inlets of the structure were beveled at a slope of 1V:1.5H. Three-dimensional FEM was generated including the exact corrugated profile of the steel structure and the additional circumferential corrugated steel plates. The calculated deformations of the structure were compared to the field data and used for the validation program. The influence of the circumferential corrugated steel plates was investigated by comparing the performance of the structure with the case of no strengthening techniques. The study showed significant reduction in the structure deformation and the induced stresses in the steel structure by the addition of strengthening elements. However, the performance of the structure at the beveled ends was not investigated through the study. In

addition, the boundary conditions of the model at the inlets were restrained at all directions to attain stability to the structure and surrounding soil.

Current design codes and standards require design for headwalls and concrete collars under the effect of any possible loading conditions, including differential settlement, earth pressure and piping (Canadian Highway Bridge Design Code (CSA 2019) and American Association of State Highway and Transportation Officials (AASHTO 2019)). Nevertheless, design codes lack specific criteria for evaluating the performance of the strengthening elements at the beveled ends. In addition, with the increase of the structures' spans recently, qualitative investigation is required for the strengthening elements at the beveled ends and their influence on the global stability of the SSS.

The current study presents numerical simulation for a large-span SSS having different beveled ends using three-dimensional finite element software Midas GTS NX (2020). In addition, the influence of using different strengthening techniques on the performance of the SSS at the beveled ends was then investigated. To achieve these objectives, the modeling approach and criteria is validated with the measured deformations of the world's largest span SSS with a span of 32.4 m, where the steel structures are supported by concrete collars at the inlets.

4.2 Description of the Bridge

Three large-span arched SSS were constructed in Dubai, UAE, in 2019 using the deepest corrugation profile. Two identical SSS have effective span of 32.39 m, earning the Guinness World Record for the world's largest-span soil-steel bridge, while the third structure has 23.76 m span. The rise of the structures is 9.57 m and a total longitudinal

length of 12.0 m. The corrugation profile of the steel plates is 500 mm pitch X 237 mm depth with 12 mm thick plates for the 32.39 m spans and 10 mm thick for the 23.76 m span. The cover height above the structures ranged between 2.5 m to 3.0 m. The structures were supported laterally in the transverse direction using steel mesh reinforcement of 10 mm steel reinforcement bars each 200 mm in the longitudinal direction, connected together with 8 mm steel bars each 600 mm in the transverse direction. The concrete foundations of the three steel structures are rested on 1.0 m diameter reinforced concrete piles with spacing ranging between 2.5 m and 3.5 m and depths ranging between 23.0 m and 26.0 m. The spacing between the western and middle structures is filled with a controlled low strength material with an average compressive strength of 8.5 MPa after 7 days. The low strength material was used for a 5.0 m thick in addition to the zones adjacent to the eastern and western concrete footings to prevent spreading of foundation system during and after the end of construction. The steel structures were backfilled with conventional granular backfill soil layers of well-graded sand with gravel mixture (SW), with less than 4% fines. The maximum dry unit weight was 21.67 kN/m^3 and a friction angle of 43° . The backfill soil was compacted every 300 mm thick layers to more than 95% optimum density according to AASHTO LRFD Bridge Design Specifications (AASHTO, 2014) and CHBDC (CSA, 2014). Fig. 4-1 presents the three soil-steel structures used in constructing Shamal bridge and the transverse section for the western structure evaluated in the current study. The figure shows also concrete collar with dimensions of 400 mm in the vertical direction; and 1090 mm in the longitudinal direction. The concrete collar is attached to the steel structure at the inlets using anchor bolts embedded through the beam.

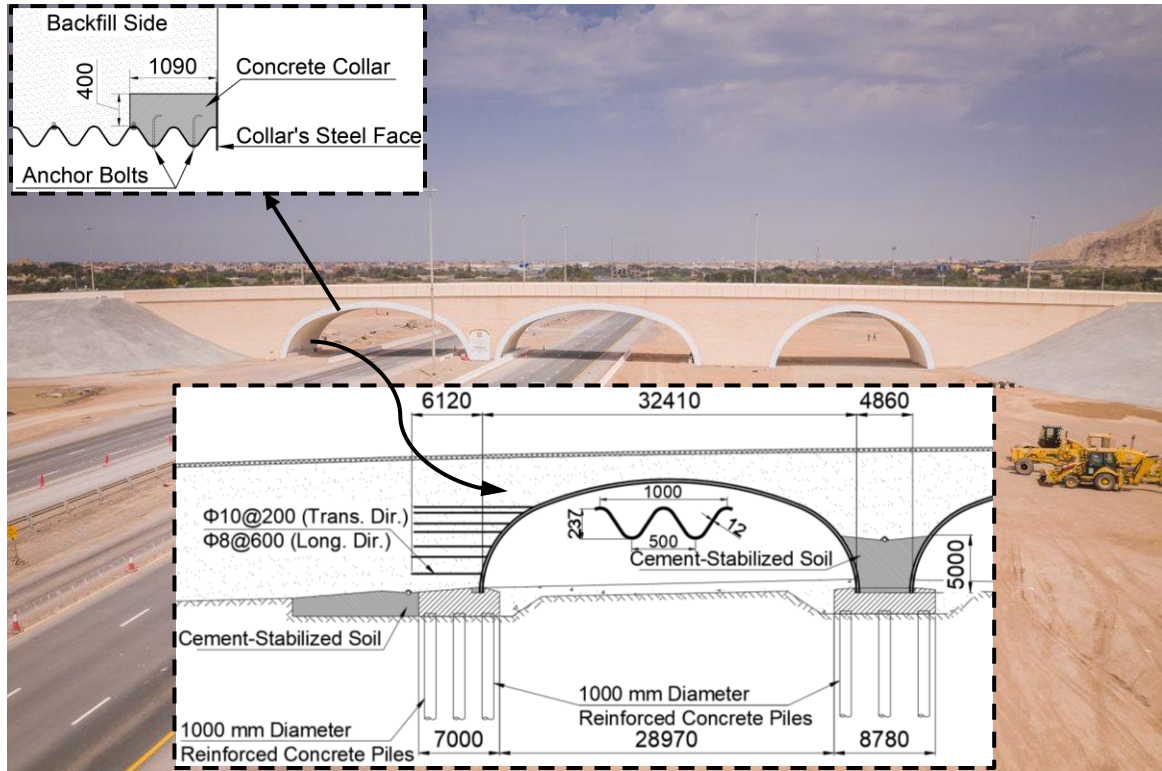


Fig. 4-1: Front view for the soil-steel bridge and transverse section (all dimensions are in mm)

The performance of the structures was monitored by providing 17 surveying points at three transverse sections of each structure. The three transverse sections located at distances of 2.54 m, 6.54 m and 9.54 m from the inlet of the SSS. Geodetic laser device was measuring three-dimensional deformations of the steel structure during and after construction by focusing on optical prisms attached to the bottom side of the structures. Fig. 4-2 shows the distribution of the surveying points along each transverse section. Embaby et al. (2022) (Chapter 3) reported comprehensive information about the site conditions and monitoring plan and the current study focused only on the performance of the structure at the transverse section at 2.54 m from the inlet side.

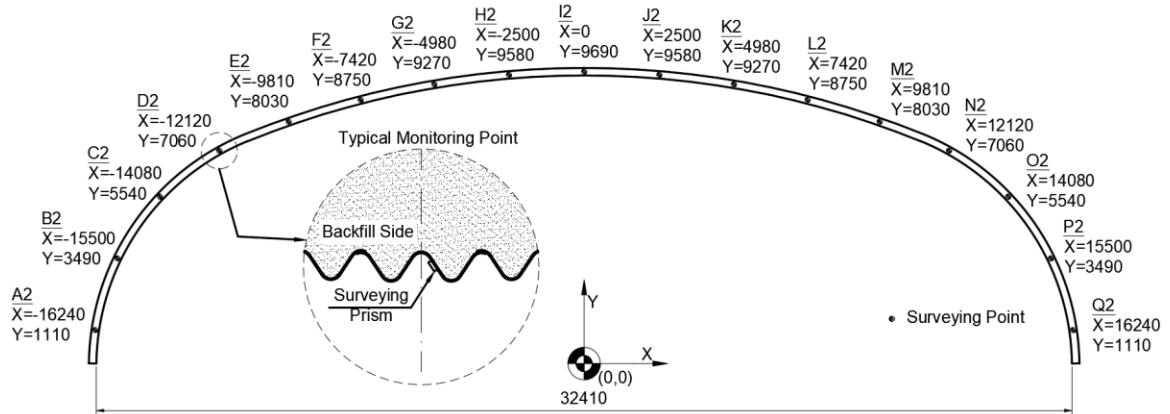


Fig. 4-2: Surveying points locations on a transverse section

4.3 Numerical Model Verification

Fig. 4-3 presents three-dimensional nonlinear finite element model using Midas GTS NX (2020). The model simulated a strip of 6.0 m with symmetric boundary conditions to represent the full longitudinal length of the bridge. Default boundary conditions were applied to the model by retrain the nodes at the edges laterally and total fixity at the bottom of the model. The effect of the boundary conditions on the deformations and axial stresses of the steel structures was eliminated by extending the boundaries of the model. The corrugation profile of the steel structure was modeled using three-noded triangular and four-noded rectangular shell elements as shown in Fig. 4-4. The soil and concrete elements were simulated using four-noded tetrahedron, six-noded pentahedron and eight-noded hexahedron solid elements. Three-noded plane-stress elements were used in simulating the steel mesh reinforcement embedded through the backfill soil. The steel mesh reinforcement was attached to the steel structures using two-noded beam elements representing the steel angles.

The nonlinear behavior of the backfill soil was simulated using Modified Mohr-Coulomb constitutive model, which is sometimes known as Hardening Soil model. Von mises failure criterion was considered for the arched steel structures. Linear elastic material model was used to simulate the steel mesh reinforcement, low-strength material and the concrete material used in the 1.0 m diameter reinforced concrete piles, pile caps and concrete collars. The plane-stress elements used in simulating the steel mesh reinforcement had equivalent thickness of nearly 0.4 mm to account for the axial stiffness of the transverse 10 mm steel bars. Geometric nonlinearity large deformations was considered in the current study based on the updated Lagrangian formulation.

Table 4-1 shows the material properties for backfill and native soil in addition to the structural elements used in the current analysis. The material properties for the backfill soil were obtained from laboratory tests performed on the backfill soil used in the project (Tarmac, 2018). Twenty-eight construction stages were modeled during construction of the bridge, considering different backfill heights around the steel structure at each stage. The compaction of backfill soil was simulated by applying uniform normal pressure of 34.5 kPa on each soil layer (Katona et al. 1979; Ezzeldin and El Naggar 2021). The applied pressure is deactivated with the addition of the layer above. The total number of elements and nodes used for the current study are 1,155,811 and 251,318 respectively. Additional details of the numerical simulation and input parameters are reported by Embaby et al. (2022) (Chapter 3).

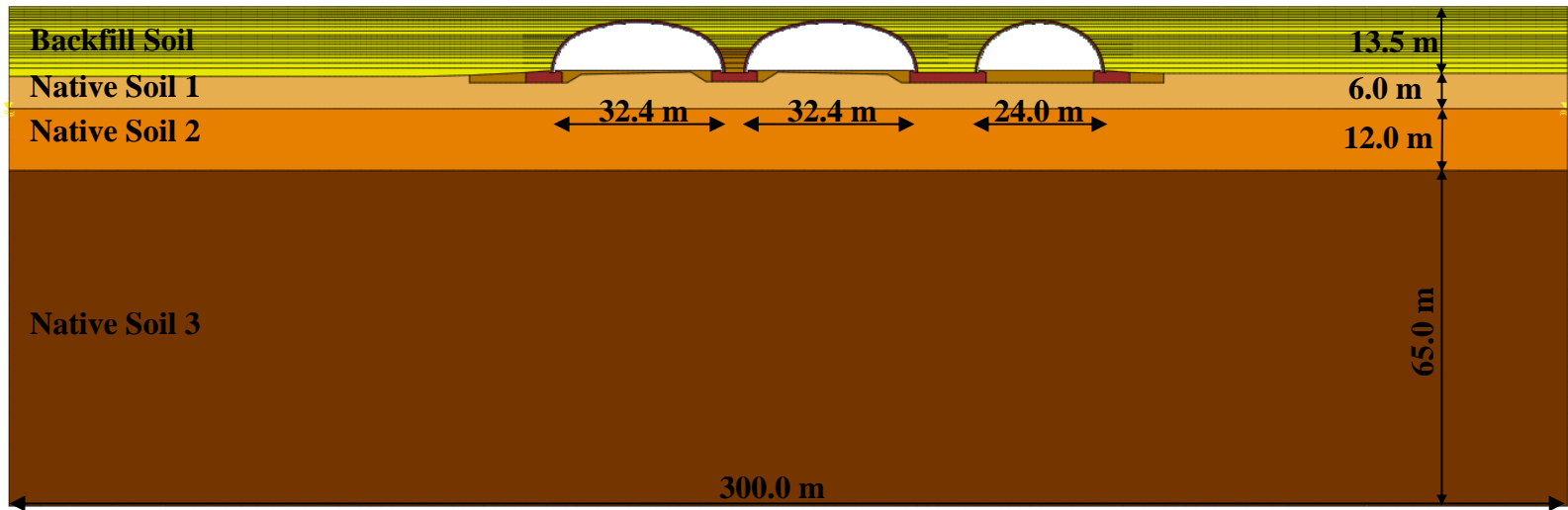


Fig. 4-3: Numerical model details and dimensions

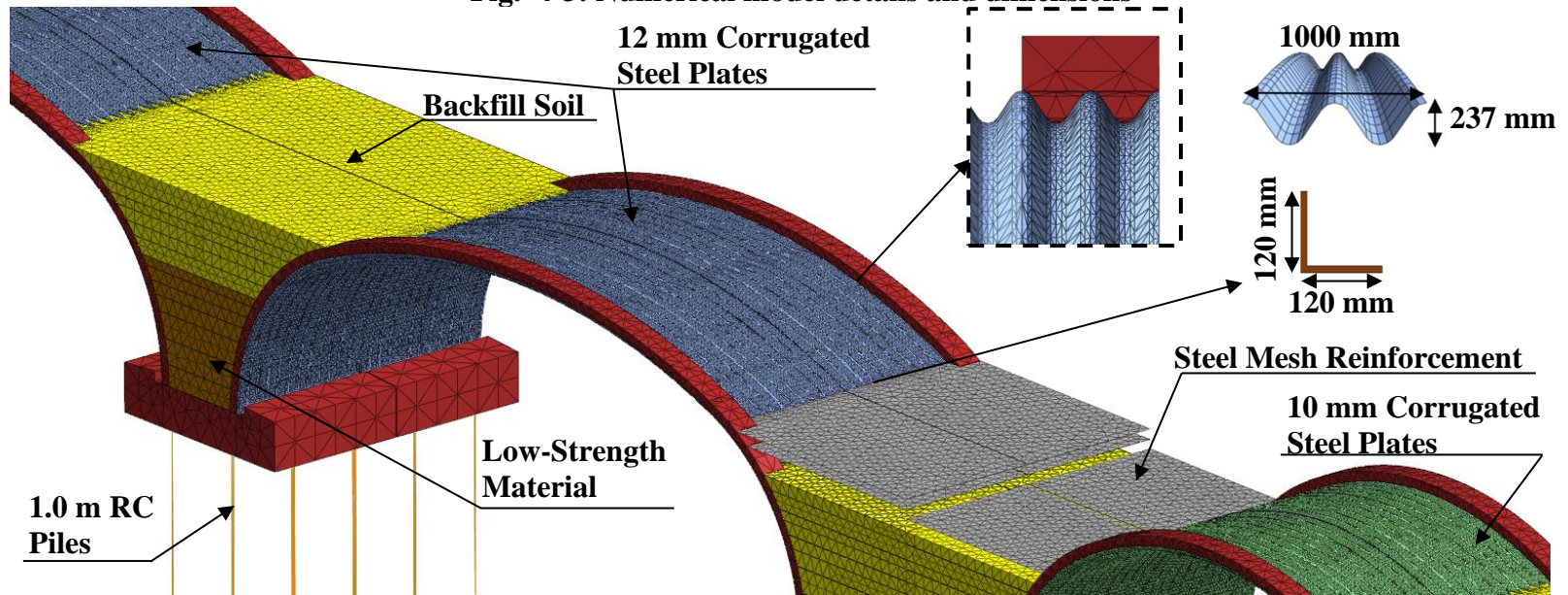


Fig. 4-4: Three-dimensional Model for Shamal Bridge

Table 4-1: Summary for Soil and Structure material Properties

Name	Concrete	Steel	Backfill Soil	Native Soil 1/2/3	Low Strength Material
Material Model Type	Linear Elastic	Von-Mises	Modified Mohr-Coulomb	Modified Mohr-Coulomb	Linear Elastic
Poisson's Ratio	0.2	0.3	0.35	0.3	0.3
Unit Weight (kN/m ³)	23.0	78.5	22.0	21.5	24
Elastic Modulus in Loading (E ₅₀) (MPa)	30000	200000	60	40/60/100	14500
Elastic Modulus in unloading/reloading (E _{ur}) (MPa)	-	-	120	80/120/200	14500
Yield Stress (MPa)	-	500	-	-	-
Friction Angle (Degrees)	-	-	43	38/40/45	-
Dilatancy Angle	-	-	6	6/10/10	-
Cohesion (kPa)	-	-	3	2/5/5	-

The steel structure was monitored during construction until the final stage. The results showed that there are two critical stages, peaking stage and final stage. Peaking stage occurred at backfill height of 9.57 m and just before adding soil cover above the structure, while the final stage is after adding nearly 3.0 m cover height. The current study focuses on the performance of a transverse section located at 2.54 m from the inlet of the structure. The evaluated cross-section is nearly 1.54 m from the concrete collar. Fig. 4-5 presents the calculated and measured deformations of the western steel structure scaled up by 10 times. The figure shows that the numerical model succeeded to capture the same trend of deformed shape of the structure at different construction stages. The difference between the calculated and measured vertical deformation did not exceed 0.5% of the rise of the steel structure. The maximum vertical deformation at 1.5 m from the concrete collar was less than 0.8% of the rise of the structure, which satisfies the requirements of CHBDC

(CSA, 2019) code limit of 2%. The results demonstrate the ability of the numerical approach in simulating the concrete collars and predicting the performance of the steel structure during and at the end of construction.

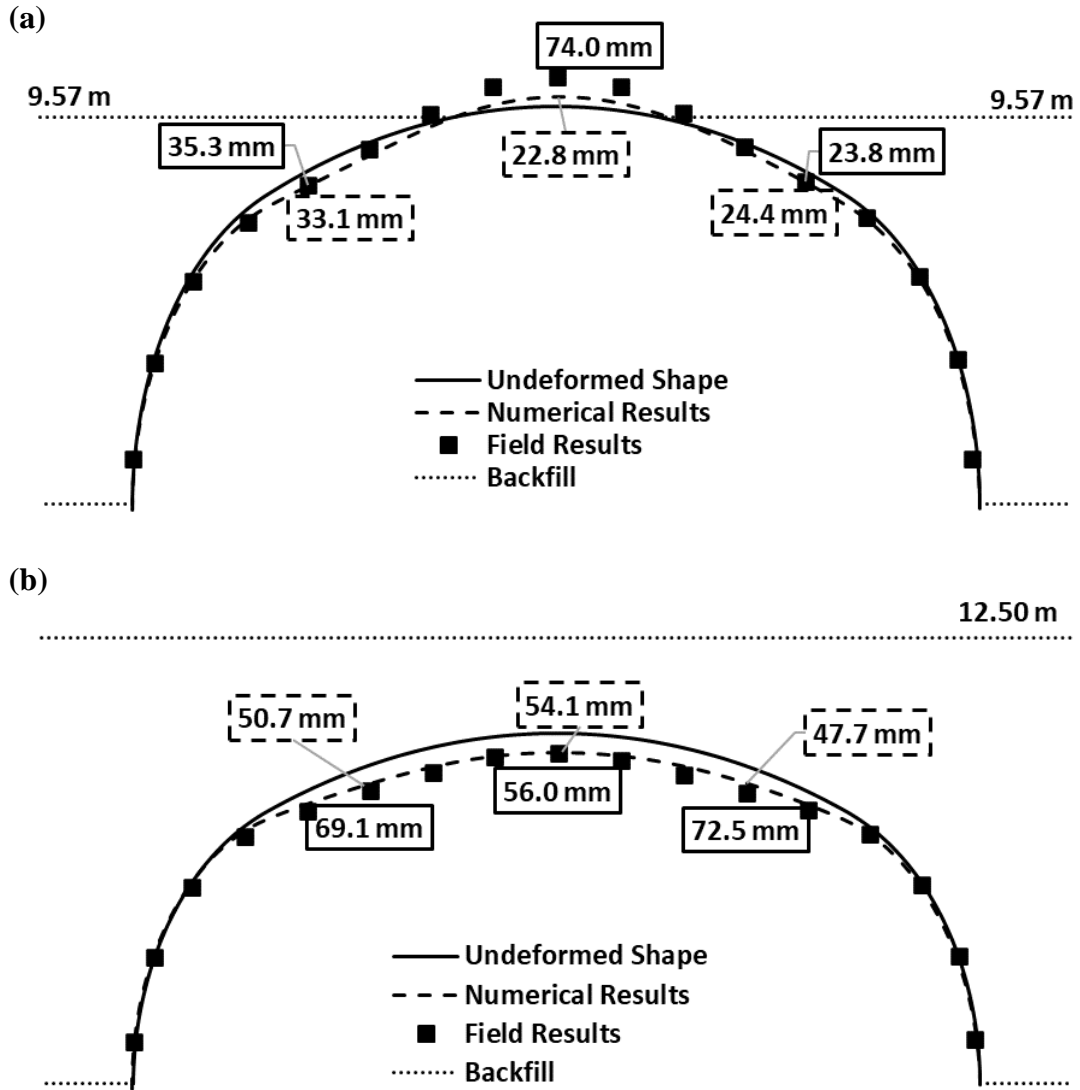


Fig. 4-5: Deformed shape for the western structure (scaled up 10 times) (a) at peaking stage; (b) at final stage

4.4 Beveled Ended Soil-Steel Structure

The validated numerical modeling approach is employed herein to investigate the stability of beveled-end large-span soil-steel structures (SSS) and the surrounding soil. Three-dimensional finite element model was conducted by considering the geometric configuration of the world's largest span SSS, Shamal Bridge (Embaby et al., 2022) (Chapter 3). The stability of the steel structure and the surrounding soil is evaluated by simulating 3 different slopes: 1.5V:1.0H (1.5 vertical to 1.0 horizontal); 2.0V:1.0H; 2.5V:1.0H. The performance of the steel structure at the beveled end is investigated under the case of no supporting elements (RM); in case of adding concrete collar (CC); and the case of steel mesh reinforcement attached to the steel structure (SMR).

Fig. 4-6 shows the three-dimensional FE model for the SSS with beveled end. Three-node shell elements were used to simulate the corrugation profile of the steel plates, while six-node pentahedron solid elements were used to simulate the surrounding soil around the steel structure. Von Mises failure criterion and modified Mohr-Coulomb failure criterion were used to simulate the nonlinear behavior of the steel structure and backfill soil, respectively. Sensitivity analysis was performed to evaluate the suitable element sizes where stability in the results is reached. The maximum element size for the steel structure was 0.25 m. The solid elements sizes ranged between 0.25 m near the steel structure to 1.0 m away from the influence zone of the structure. The vertical boundaries of the numerical model were restrained against horizontal displacements and the bottom boundary was restrained at all directions. The degrees of freedom at the beveled end of the numerical model were not restrained at any direction and the stability of this zone depends only on the stability of the slope. Staged construction analysis is considered to simulate the

accumulation of the internal stresses in the steel structure during different construction stages. Geometric nonlinear large deformation is considered in the current analysis based on updated Lagrangian formulation to account for the large deformations occurring to the steel structure during construction.

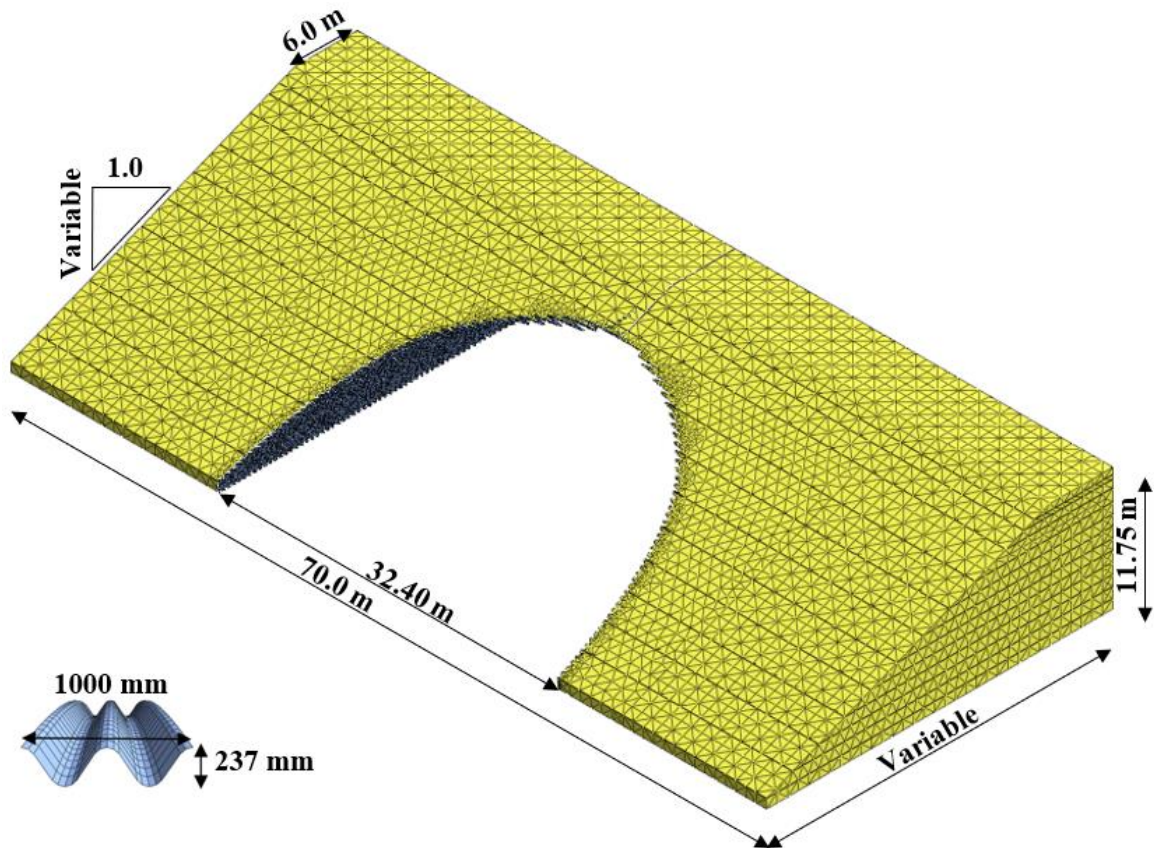


Fig. 4-6: Three-dimensional view for the numerical model

Fig. 4-7 presents the case of concrete collar attached to the arched steel structure. The main purpose of the concrete collar is to retain the incomplete steel rings, referred to as cut rings, and connect them to the complete full rings. The concrete collar is simulated using linear elastic constitutive model. Six-node pentahedron solid elements were used in simulating the configuration of the element. The common nodes between the concrete collar and the

steel structure were fully bonded together as the concrete collar is actually attached to the steel structure using anchor bolts embedded in the concrete beam and bolted with the steel structure. The concrete collar has dimensions of 600 mm starting from the crest of the corrugated profile; and 650 mm perpendicular to the slope of the beveled end. The concrete collar elements are activated just after installing the steel structure and before starting backfilling.

Fig. 4-8 shows the case of steel mesh reinforcement placed every 1.0 m in the vertical direction. The used steel mesh reinforcement is 10 mm steel bars spaced at 200 mm in the longitudinal direction and 8 mm steel bars spaced at 600 mm in the transverse direction. The steel mesh is attached to the steel structure by welding them to 120 X 120 X 12 mm steel angles that are connected to the steel structure using bolted connections. In the numerical model, the steel angles were simulated using two-noded beam elements and rigidly connected to the steel structure. The steel mesh reinforcement was simulated using three-noded and four-noded plane stress elements with equivalent thickness of 0.4 mm that represents of the same axial stiffness of the 10 mm steel bars that are embedded in the transverse direction. The simulation technique of using plane stress elements was validated by Embaby et al. (2022) (Chapter 3) with the technique of using the actual configuration of the steel bars. The validation program has showed good agreement between the results obtained from the case of using plane stress elements as for the steel mesh reinforcement with the case of using beam elements representing the steel bars configuration with a difference in deformations and stress resultants less than 1% between the modeling approaches. The steel mesh reinforcement has 6.0 m embedded depth in the surrounding

soil measured from the base support of the steel structure. The material properties of the structural elements and surrounding soil were obtained from Table 4-1.

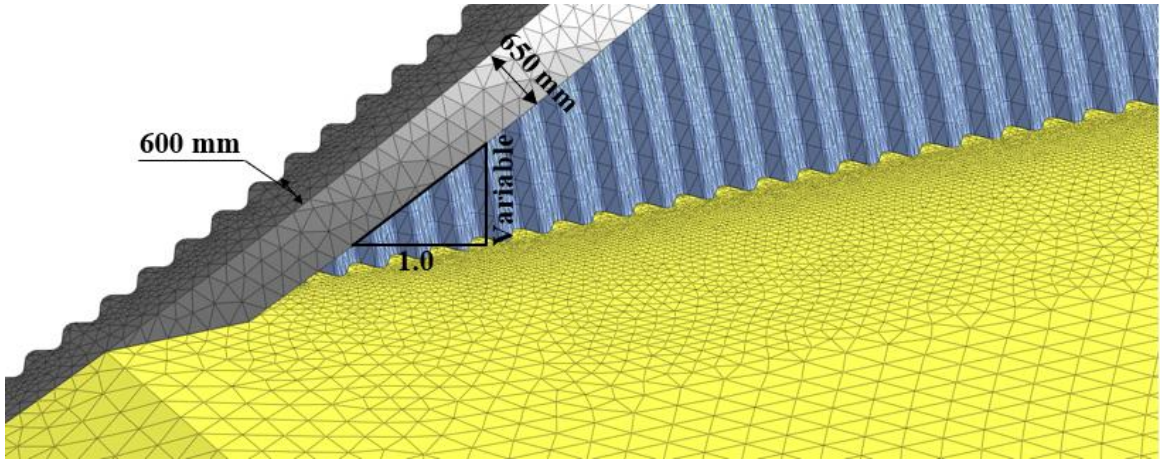


Fig. 4-7: Three-dimensional view for the concrete collar attached to soil-steel structure

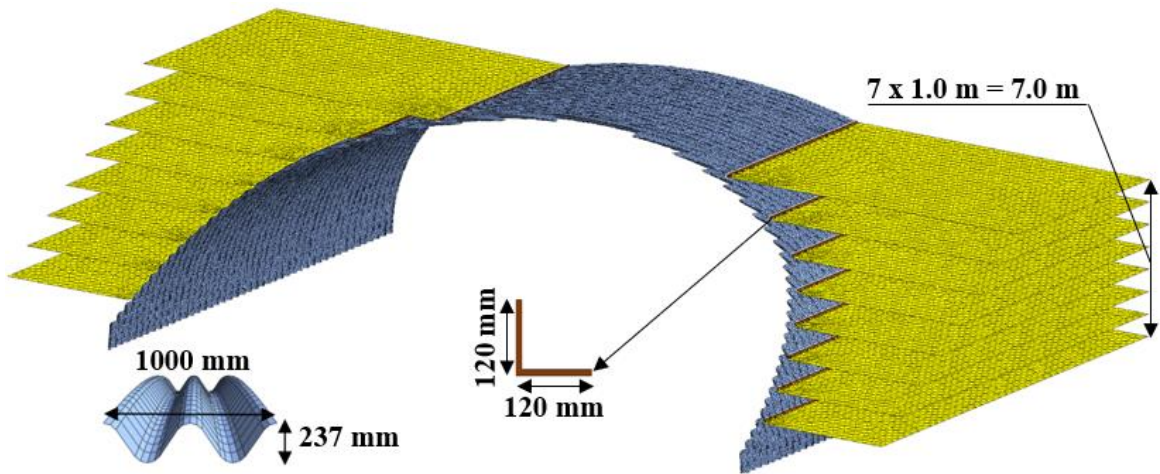


Fig. 4-8: Three-dimensional view for the steel mesh reinforcement

4.5 Results

Fig. 4-9 shows the side view for the steel structure and the locations of the investigated cross-sections. The performance of the steel structure was analyzed at both peaking stage

and final stage. The peaking stage occurred at backfill height of 9.0 m, just below the rise of the steel structure. The final stage represents the addition of 2.0 m above the crest of the corrugated steel profile at the crown. The structure deformations and longitudinal stresses were recorded at a cross-section away from the influence zone of the beveled end with a distance equal to the rise of the steel structure, referred to as Full Ring. The performance of the full ring connected to the beveled end was investigated and referred to as First Full Ring. The longitudinal performance of the steel structure along the beveled end was explored at distances normalized by the horizontal length of the slope. The deformations and longitudinal stresses along the transverse cross-sections were recorded and used in demonstrating the influence of the beveled end slopes and the additional strengthening techniques.

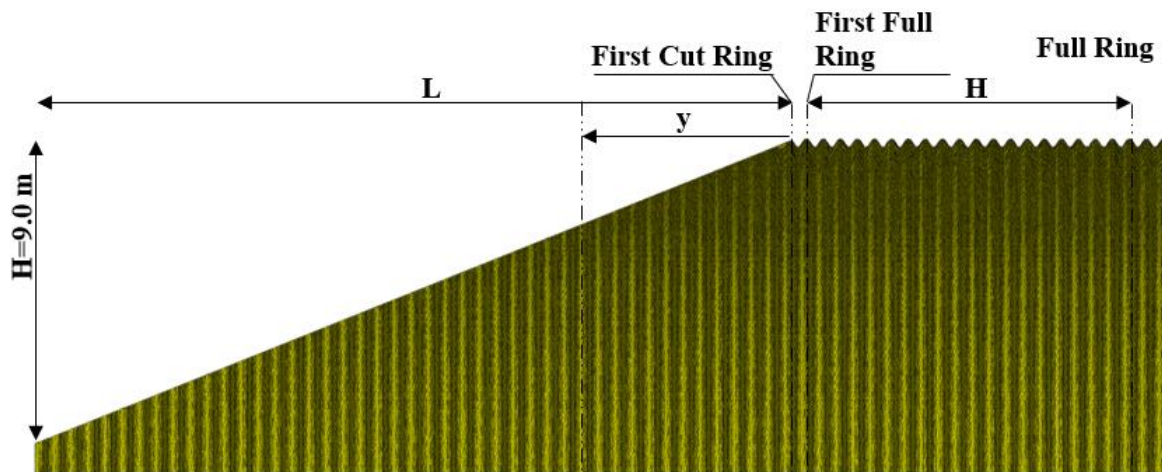


Fig. 4-9: Side view of steel structure including investigated cross-sections

4.5.1 Structure Deformations

Figs. 4-10 – 4-12 present the deformed shape of the steel structure at the peaking and final stages in cases of three different slopes under the effect of: no strengthening (RM); concrete

collar (CC); and steel mesh reinforcement (SMR). At the peaking stage, the figures show that the steel structure exhibited large lateral deformations at the shoulders in case of RM case in comparison to CC and SMR cases. These relatively large lateral deformations led to upward crown deformations exceeding 1.0% of the rise of the steel structure. The maximum allowable upward vertical deformation of the structure during construction shall not exceed 2% of the rise of the structure as per the requirements of CHBDC (CSA, 2019). The case of no strengthening techniques at the beveled end showed significantly large lateral deformations in the steel structure comparing to CC and SMR cases. The figures also reveal that the lateral deformations in the steel structure increases as the slope of the beveled end increases. The increase in lateral deformations as slope increases is attributed to the increase in the longitudinal distance between the first full ring and the tip of the slope (L) that represent the supports for the incomplete cut rings. The increase in the longitudinal distance between the first full ring and the tip of the slope increases the flexibility of the steel structure, and consequently, increases the lateral deformations in the steel structure.

At the final stage, the figures show that the deformations in the case of no strengthening techniques increased mainly at the highest 20% of the cut rings (i.e., from $y/L=0$ to $y/L=0.2$) after adding soil cover above the structure. The reason for that increase at this zone is that the highest 20% of cut rings were beveled at the upper zone of the structure that supports vertical stresses from soil above. The upward crown deformation of the first full ring and first cut ring was not influenced significantly by adding soil cover since relatively small soil cover was added at this area due to the beveled slope. The figures also show that the concrete collar and steel mesh reinforcement controlled the differential deformations of the cut rings at different beveled end slopes. However, the case of using

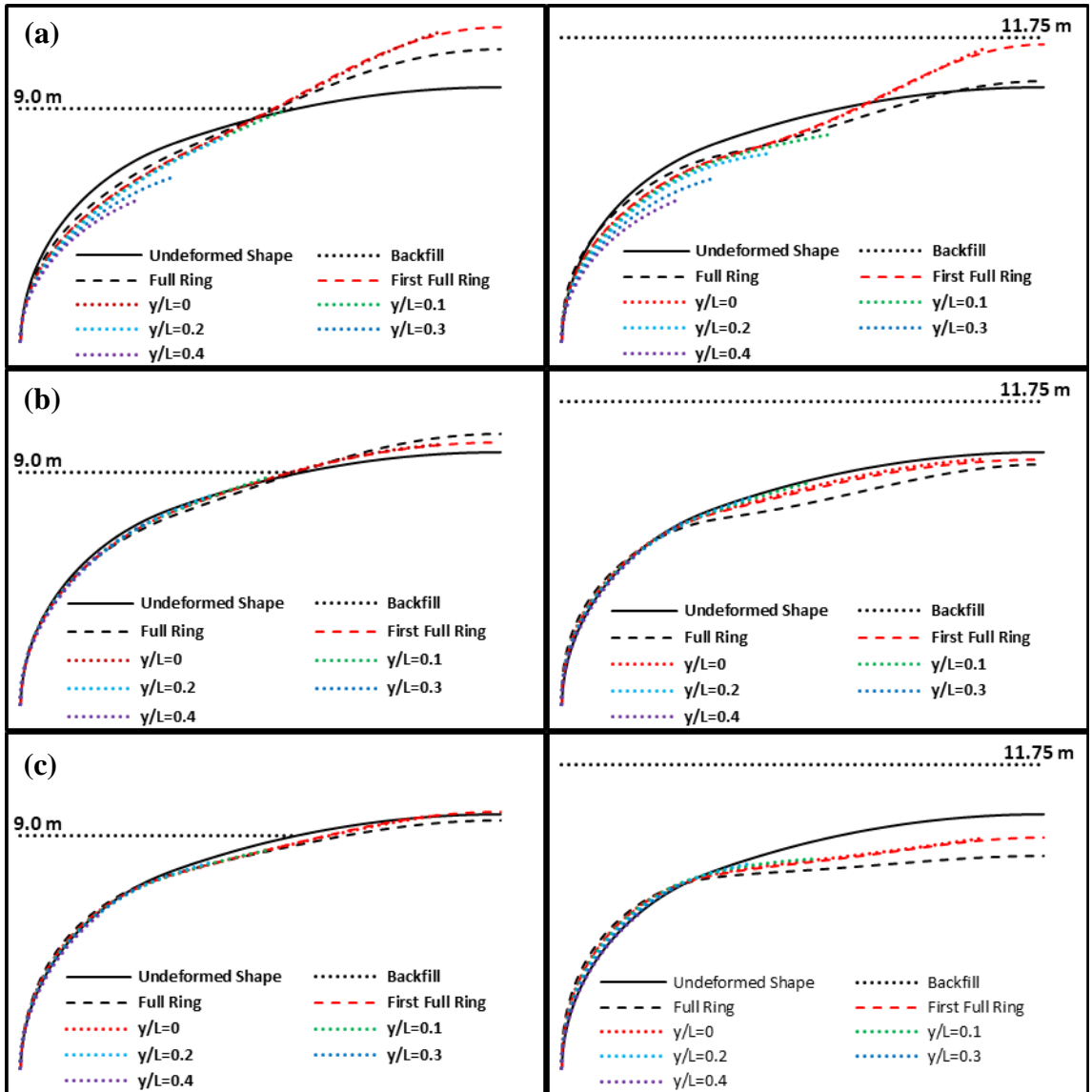


Fig. 4-10: Deformed shape of steel structure at peaking and final stages with 1.5:1 beveled end (scaled up 30 times) (a) RM; (b) CC; (c) SMR

steel mesh reinforcement exhibited large downward deformations at the full rings and first cut ring. This is attributed to the relatively very small deformations in the upper zone of the steel structure occurred in the case of steel mesh reinforcement during peaking stage. By adding soil cover above the steel structure, the contribution of steel mesh reinforcement was not significant, and the upper zone of the structure deformed downwards.

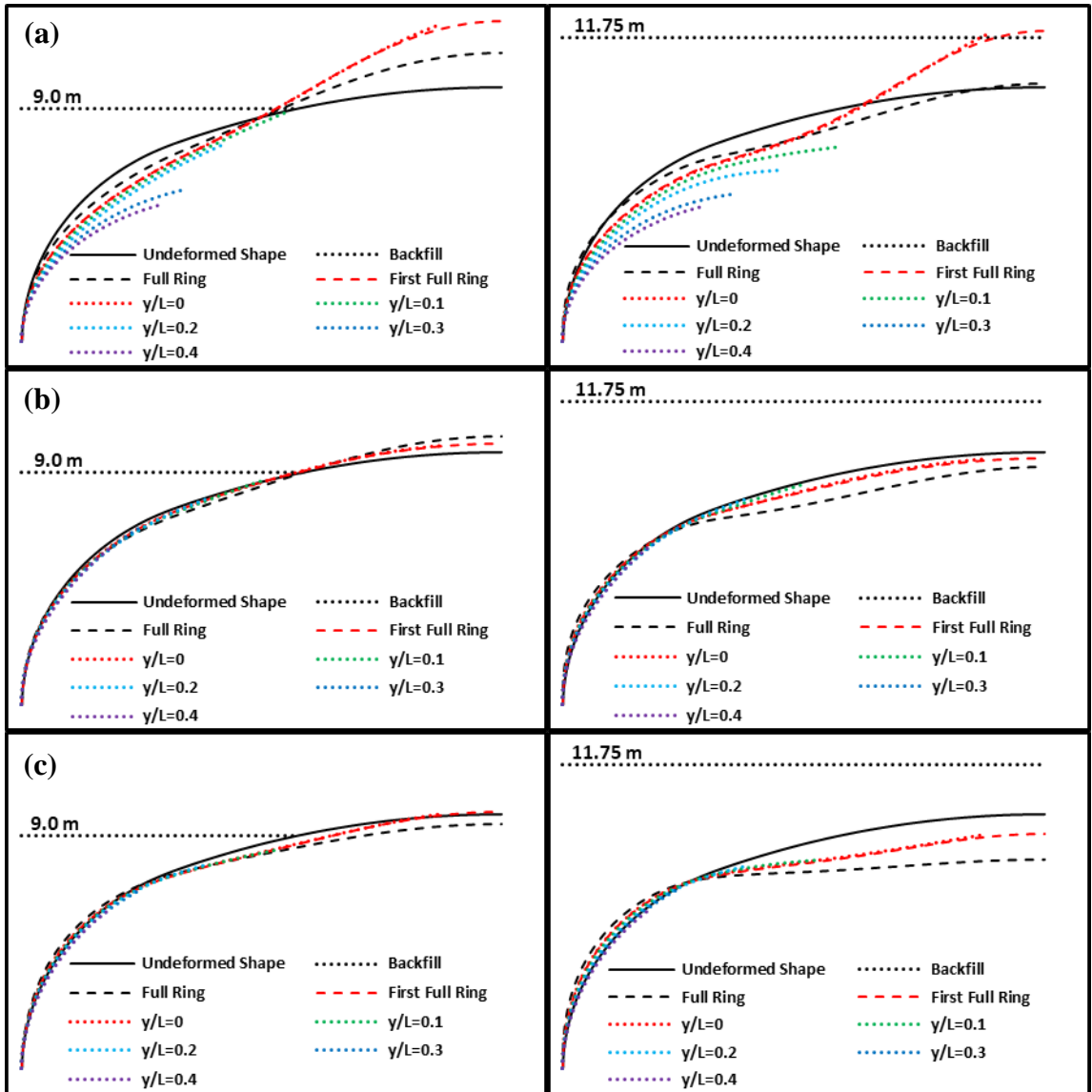


Fig. 4-11: Deformed shape of steel structure at peaking and final stages with 2.0:1 beveled end (scaled up 30 times) (a) RM; (b) CC; (c) SMR

Figs. 4-13 and 4-14 demonstrate the influence of different strengthening techniques and beveled end slopes on the maximum exhibited vertical and horizontal deformations of the steel structure at peaking stage and final stage, respectively. The figures show that the steel mesh reinforcement and concrete collar controlled the lateral deformations of the structure at peaking and final stages at all sections. The vertical deformations in case of steel mesh

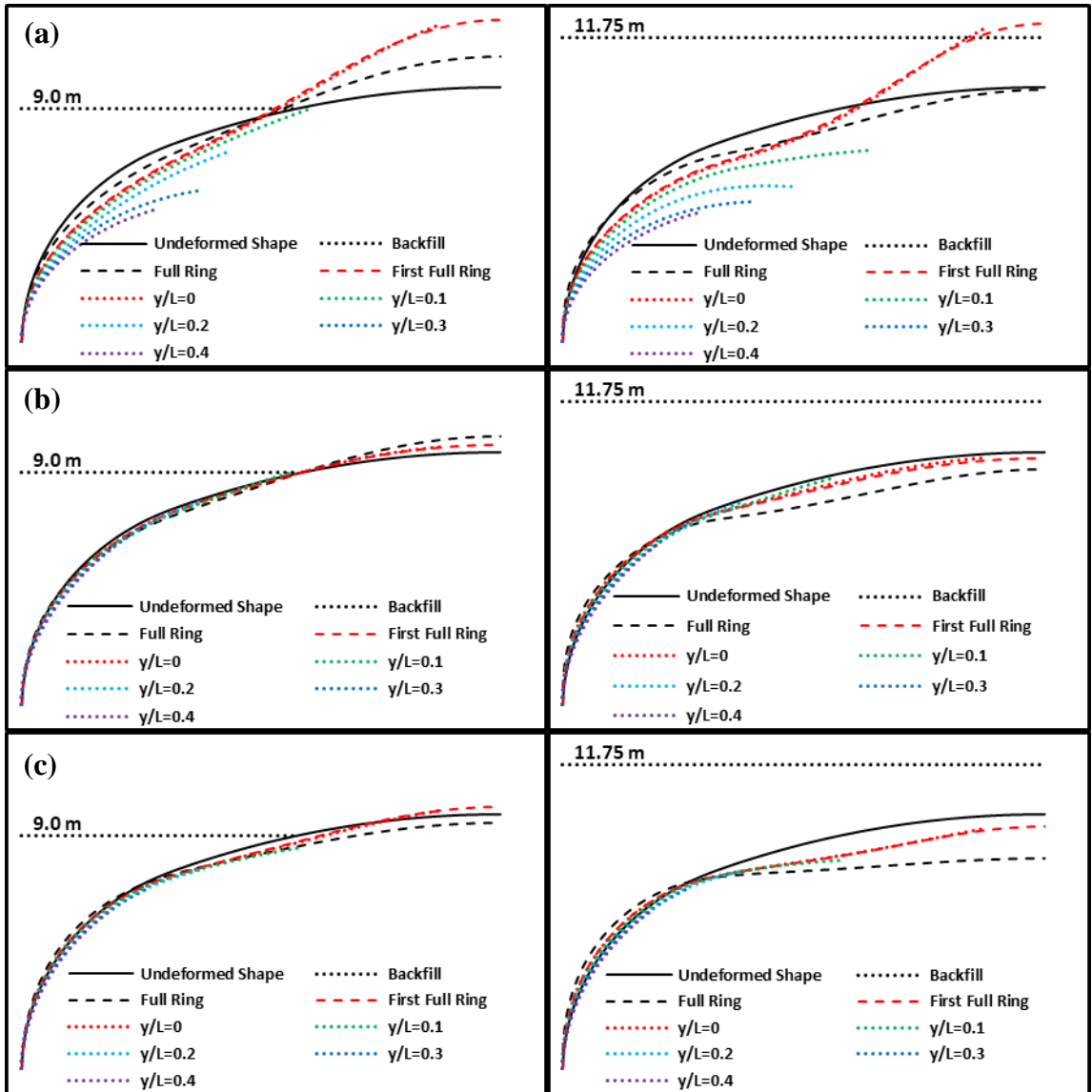


Fig. 4-12: Deformed shape of steel structure at peaking and final stages with 2.5:1 beveled end (scaled up 30 times) (a) RM; (b) CC; (c) SMR

reinforcement are relatively higher than the case of concrete collar at the highest 20% cut rings. The figures show also that the deformations in case of no strengthening techniques are significantly higher than the cases of steel mesh reinforcement and concrete collar. The maximum lateral deformations occur between $y/L=0.3$ and $y/L=0.4$. The lateral deformations start to decrease towards the tip of the slope. This is attributed to the decrease

in the height of the steel rings where the lateral stiffness of the corrugated steel section can sustain the lateral deformation. The figures also demonstrate the influence of beveled end slope on the vertical and horizontal deformations of the steel structure. The longitudinal distance between the first full ring and the tip of the slope (L) increases with the increase of slope leading increase in structure flexibility and deformations.

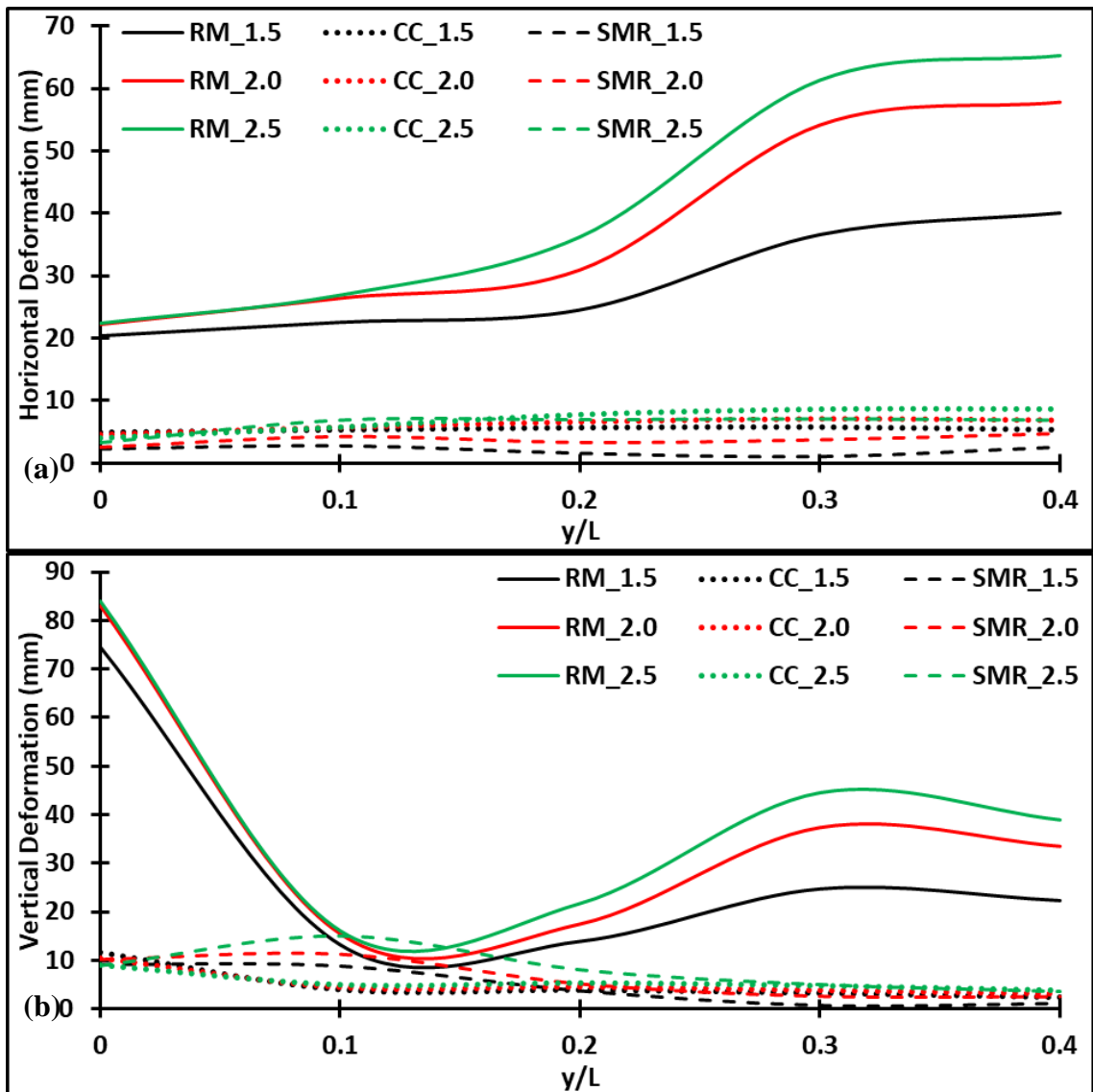


Fig. 4-13: Distribution of maximum deformations at peaking stage in (a) horizontal direction; (b) vertical direction

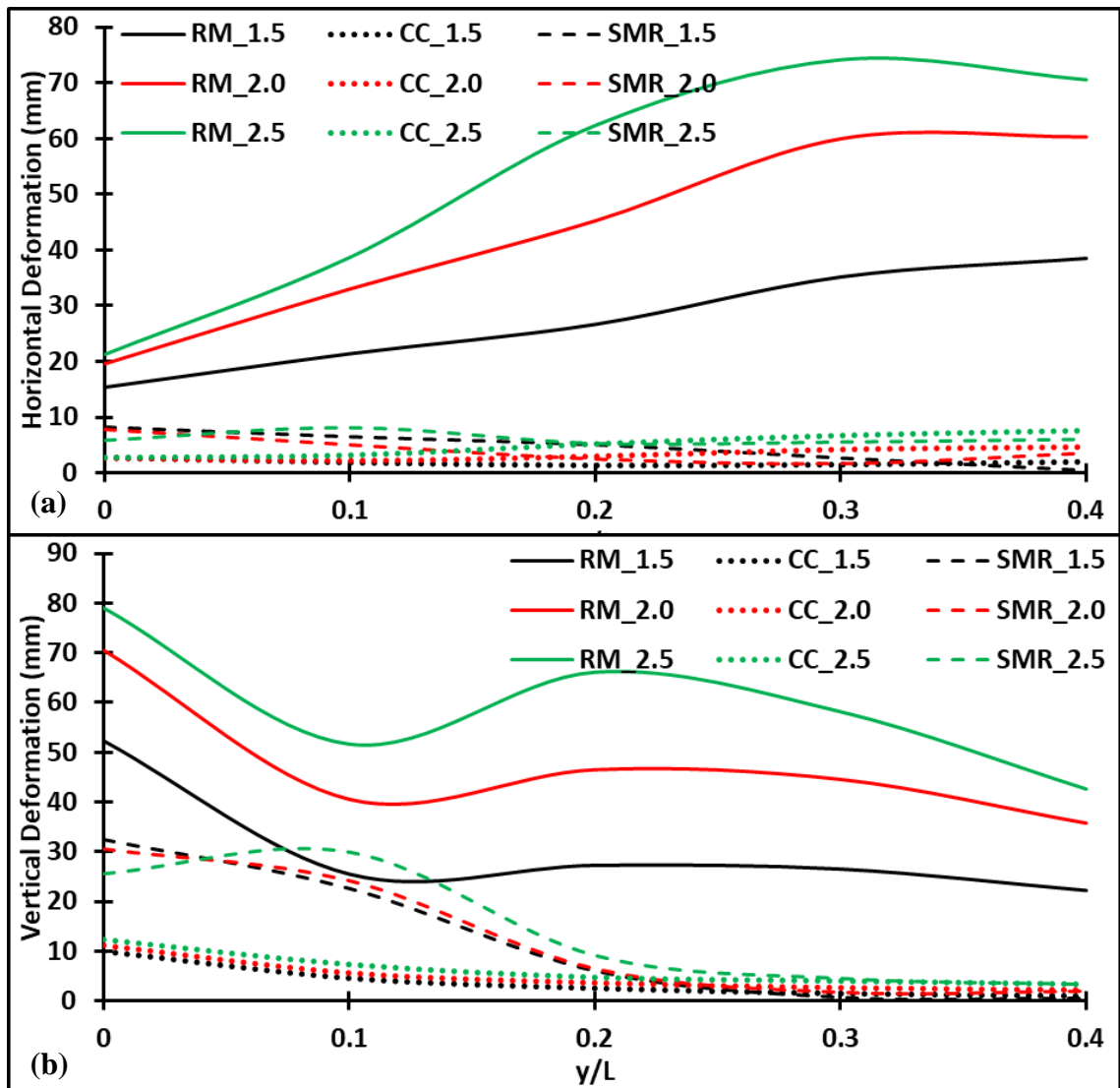


Fig. 4-14: Distribution of maximum deformations at final stage in (a) horizontal direction; (b) vertical direction

4.5.2 Circumferential Stresses

Fig. 4-15 presents the influence of different strengthening techniques to beveled end structures on the circumferential stresses at different cross-sections. The figure demonstrates that the influence of beveled end slope on the maximum induced circumferential stresses was not significant. The maximum induced circumferential stresses occurred at the first cut ring. The circumferential stresses decrease by more than

50% after the highest 10% of cut rings. On the other hand, steel mesh reinforcement and concrete collar reduced the induced axial stresses by nearly 30-50% comparing to the case with no strengthening elements. The maximum circumferential stresses in case of steel mesh reinforcement occurred also at the first cut ring and the stresses decreased by more than 50% towards the tip of the slope. The reduction in the axial stresses towards the tip of the slope decreased to nearly 30% in the cases of concrete collar.

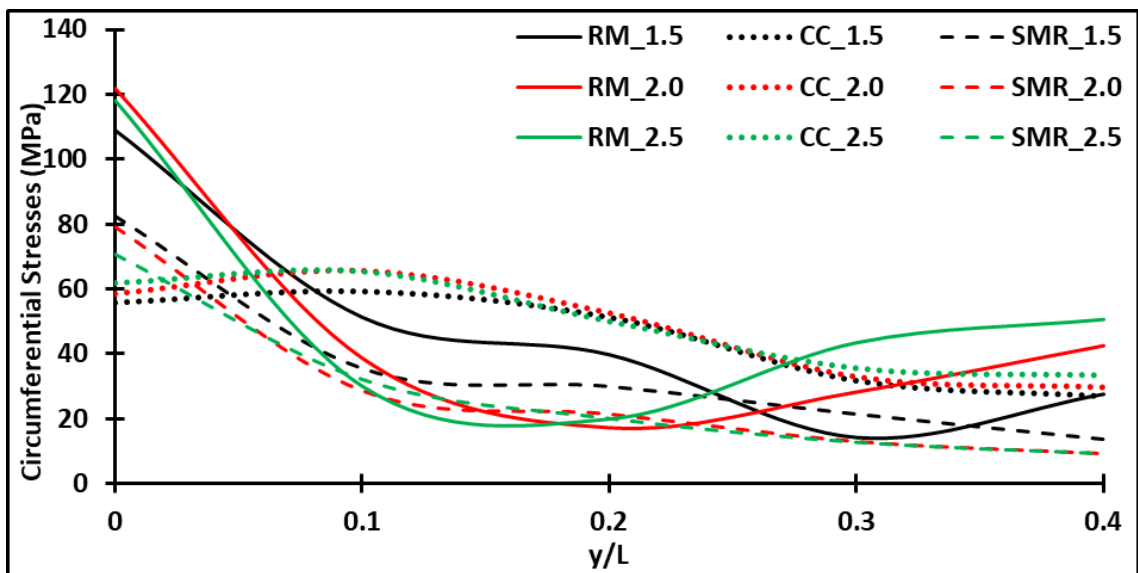


Fig. 4-15: Distribution of maximum circumferential stresses at final stage

4.5.3 Longitudinal Bending Moment

Fig. 4-16 shows the maximum longitudinal bending moment induced in the corrugated steel plates at different strengthening techniques and slopes. The results demonstrate that the corrugated steel plates are subjected to significant longitudinal bending moment which is influenced by the slope of the beveled end. This is attributed to the stability of the cut rings that is maintained by inducing longitudinal bending moment that is transferred to the full rings through transverse bolted connections. Transverse bolted connections are used to

connect full rings with each other to transfer longitudinal loads without separation or failure. Full rings' stability is subjected mainly to circumferential stresses and circumferential bending moment that are generated in the full cross-section of the corrugated profile. In the case of beveled end structures, longitudinal bending moment is induced in the steel plates in addition to the full cross-section circumferential stress resultants. The transverse bolt connections and steel plates require to be designed under the longitudinal forces and bending longitudinal bending moment that are generated from the longitudinal rotation of the structure. Fig. 4-16 also reveal that the longitudinal bending moment increases significantly in the case of no strengthening techniques by the increase of the slope. The reason is increasing the longitudinal distance between the full rings and the tip of the slope, and consequently, increase the number of cut rings that require additional longitudinal bending moment to maintain stability. The figure shows also that the case of using steel mesh reinforcement generate longitudinal bending moment at the highest 10% of the cut rings. The longitudinal bending moment was not prevented by the addition of SMR, however, decreased by 30-50% comparing to the case of no strengthening techniques. The reason is that SMR has no flexural capacity to resist the longitudinal rotation that the steel structure would suffer, nevertheless, SMR contributes to decreasing the lateral deformations of the steel structure. The case of using CC showed significantly small bending moment values induced in the steel plates along the cut rings. This is attributed to the large relative flexural stiffness of the CC comparing to the corrugated steel plates. The CC resists the longitudinal rotation of the structure at different beveled end slopes.

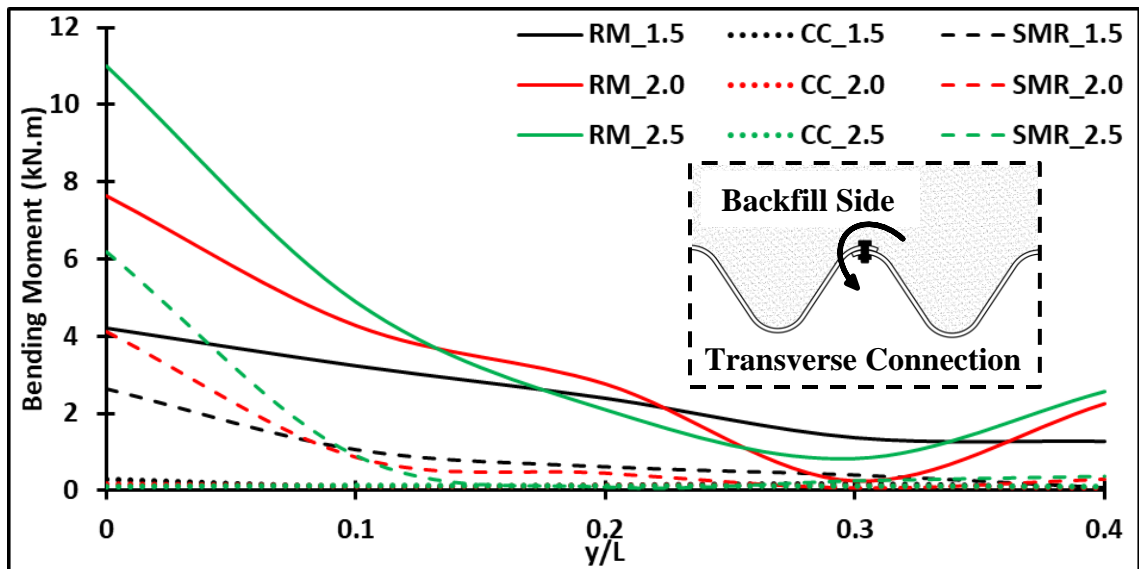


Fig. 4-16: Distribution of maximum longitudinal bending moment at final stage

4.6 Conclusion

Three-dimensional numerical analysis was conducted on large-span SSS comprising the deepest corrugated steel plates of 500 X 237 mm to investigate the influence of different beveled end slopes on the stability of the structure. The numerical modeling approach was based on 3D nonlinear FE model validated by the field results of the world's largest-span SSS with a span of 32.4 m where the steel structure was supported by concrete collars and steel mesh reinforcements. The following conclusions can be drawn from the current study:

- The numerical simulation correctly captured the performance of the steel structure under the condition of attaching concrete collars and steel mesh reinforcements to the sides of the structure.
- The vertical earth pressure distribution around the buried steel structure was non-uniform. Soil arching can be observed between the steel structure and surrounding

soil; transverse sections in the buried steel structure with and without concrete collars; and local soil arching along crest and valley of the corrugated steel profile.

- The effects of different beveled end slopes on the deformations, axial stresses and bending moment values of the corrugated steel plates were evaluated using the validated modeling approach.
- The slope of the beveled ends significantly affected the induced stress resultants in the steel structure in the longitudinal direction. However, the circumferential stresses at different transverse cross-sections were not affected by changing the slope of beveled ends.
- The induced longitudinal bending moment increased significantly by increasing the slope of the beveled ends leading to excessive longitudinal stresses in the steel plates and transverse bolted connections.
- A reduction in the circumferential stresses by about 30% is predicted in case of using steel mesh reinforcement around SSS.
- Reinforced concrete collars reduce the induced circumferential stresses in the steel structures by up to 50%. In addition, concrete collars distribute the induced circumferential stresses along different transverse cross-sections.
- Finally, the results obtained from comparing the longitudinal bending moment under different strengthening techniques demonstrated the significance of using concrete collar in reducing the longitudinal bending moment and consequently, controls the design and cost of the SSS.

4.7 References

- Atlantic Industries Limited (AIL). 2019. Personal Communication.
- AASHTO (American Association of State Highway and Transportation Officials). 2019. AASHTO LRFD Bridge Design Specification, customary U.S. units, 7th Ed. Washington, D.C.: AASHTO
- AASHTO (American Association of State Highway and Transportation Officials). 2014. AASHTO LRFD Bridge Design Specification, customary U.S. units. Washington, D.C.: AASHTO
- Beben, D. and A. Stryczek. 2016. "Numerical analysis of corrugated steel plate bridge with reinforced concrete relieving slab." *Journal of Civil Engineering and Management*, 22 (5), 585-596. DOI: <https://doi.org/10.3846/13923730.2014.914092>
- Beben, D. and Z. Manko. 2008. Static load tests of a corrugated steel plate arch with relieving slab. *Journal of Bridge Engineering*. 13(4), 362-376. [https://doi.org/10.1061/\(ASCE\)1084-0702\(2008\)13:4\(362\)](https://doi.org/10.1061/(ASCE)1084-0702(2008)13:4(362))
- CHBDC (Canadian Highway Bridge Design Code). 2014. Canadian Standards Association. CAN/CSA-S6-14., Mississauga, ON.: CHBDC

- CHBDC (Canadian Highway Bridge Design Code). 2019. Canadian Standards Association. CAN/CSA-S6-14., Mississauga, ON.: CHBDC
- El-Sawy, K. 2003. "Three-dimensional modeling of soil-steel culverts under the effect of truckloads." *Thin-walled Structures*, 41, 747-768. DOI: [https://doi.org/10.1016/S0263-8231\(03\)00022-3](https://doi.org/10.1016/S0263-8231(03)00022-3)
- Elshimi, T. M., R. W. I. Brachman, and I. D. Moore. 2013. "Effect of truck position and multiple truck loading on response of long-span metal culverts." *Can. Geotech. J.* [dx.doi.org/10.1139/cgj-2013-0176](https://doi.org/10.1139/cgj-2013-0176)
- Embaby, K., H. El Naggar, and M. El Sharnouby. 2021. "Response evaluation of large-span ultra-deep soil-steel bridges to truck loading." *Int. J. Geomech.*, 21(10). [https://doi.org/10.1061/\(ASCE\)GM.1943-5622.0002159](https://doi.org/10.1061/(ASCE)GM.1943-5622.0002159)
- Embaby, K., H. El Naggar, and M. El Sharnouby. 2022. "Performance of large-span arched soil-steel structures under soil loading" *Thin-Walled Structures*. 172. <https://doi.org/10.1016/j.tws.2022.108884>
- Ezzeldin, I. and H. El Naggar. 2021. Three-dimensional finite element modeling of corrugated metal pipes. *Transportation Geotechnics*. 27. <https://doi.org/10.1016/j.trgeo.2020.100467>

- Flener, E. 2010. Soil-steel interaction of long-span box-culverts – performance during backfilling.” *Journal of Geotechnical and Geoenvironmental Engineering*, 136(6), 823-832. [https://doi.org/10.1061/\(ASCE\)GT.1943-5606.0000287](https://doi.org/10.1061/(ASCE)GT.1943-5606.0000287)
- Girges, Y. and G. Abdel-sayed. 1995. "Three-dimensional analysis of soil-steel bridges." *Canadian Journal of Civil Engineering*, 22, 1155-1163. DOI: 10.1139/195-133
- Katona, M. 1978. "Analysis of long-span culverts by the finite element method." *Transportation Research Board 678*, Transportation Research Board, Washington D.C. 59-66.
- Katona, M., D. Meinhert, R. Orillac, and C. Lee. 1979. "Structural evaluation of new concepts for long-span culverts and culvert installations." Washington, D.C.: FHWA
- Lefebvre, G., M. Laliberte, L. Lefebvre, Lafleur J. and C. Fisher. 1976. Measurement of soil arching above a large diameter flexible culvert. *Canadian Geotechnical Journal*. 13(1), 58-71. <https://doi.org/10.1139/t76-006>

- Machelski, C., G. Antoniszyn, B. Michalski. 2006. "Live load effects on a soil-steel bridge founded on elastic supports." *Studia Geotechnica et Mechanica*, 28, 2-4, 65-82
- Mak, A. C., R. W. I. Brachman, I. D. Moore. 2009. "Measured response of a deeply corrugated box culvert to three dimensional surface loads." In *Proc., Transportation Research Board Annual Conference*, Washington, D.C.: TRB, 09-3016
- Maleska T. and D. Beben. 2019. "Numerical analysis of a soil-steel bridge during backfilling using various shell models." *Engineering Structures*. 196. <https://doi.org/10.1016/j.engstruct.2019.109358>
- Midas GTS-NX. 2020. <https://www.midasoftware.com/geo/gtsnx/products/midasgtsnx>
- Moore, I. and B. Taleb. 1999. "Metal culvert response to live loading performance of three-dimensional analysis." *Transportation Research Board* 1656, Transportation Research Board, Washington D.C. 37-44
- Moore, I. and R. Brachman. 1994. "Three-dimensional analysis of flexible circular culverts." *Journal of Geotechnical Engineering*, 120 (10), 1829-1844. DOI: [https://doi.org/10.1061/\(ASCE\)0733-9410\(1994\)120:10\(1829\)](https://doi.org/10.1061/(ASCE)0733-9410(1994)120:10(1829))

- Sargand, S. M., G. A. Hazen, T. Masada. 1994. Long-term field study of a deep-corrugated metal box type culvert. *Canadian Geotechnical Journal*. 31(2), 175-180. <https://doi.org/10.1139/t94-023>
- Tarmac. 2018. "Construction and execution of emirates road at RAK." Project No. R/7078-311906/77/2016. Dubai, UAE
- Tomala, P. and R. Vegerby-Hansen. 2017. "Structure in big skew – Gladsaxe case Denmark." *Archives of Institute of Civil Engineering*. 10.21008/j.1897-4007.2017.23.25
- Webb, M. C., E. T. Selig, J. A. Sussmann and T. J. McGrath. 1999. Field tests of a large-span metal culvert. Washington, DC: Transportation Research Record: *Journal of the Transportation Research Board*. 1656(1), 14-24. <https://doi.org/10.3141/1656-03>
- Williams, K., S. Mackinnon and J. Newhook. 2012. New and innovative developments for design and installation of deep corrugated buried flexible steel structures. The 2nd European conference on buried flexible structures. Poznan, Poland

5 Response Evaluation of Large-Span Ultra-Deep Soil-Steel Bridges to Truck Loading

5.1 Introduction

Soil-steel structures have been used for a few decades as an economical alternative solution for mining, water crossing, roadways and railways overcrossing. Various corrugation profiles have been investigated under the impact of surrounding soil and static truck loading. Recently, a new corrugation profile, Ultra-Cor, has been developed with total depth of 237 mm and 500 mm pitch. The corrugation profile was increased to support larger span bridges. However, the performance of such large-span soil-steel bridges using Ultra-Cor profiles has not been investigated under the influence of several factors such as soil cover height, compaction of backfill soil and truck loading.

Several numerical studies have investigated the performance of soil-steel bridges under soil self-weight and traffic loads. Many of these studies were conducted using two-dimensional numerical modeling and simulated the backfill soil behaviour employing Mohr-Coulomb failure criterion (Katona 1978, Machelski et al., 2006; Flener, 2010). Three-dimensional FE modeling studies were also performed to investigate the influence of truck loading on the performance of steel structures (Moore and Brachman, 1994; Girges and Abdel-Sayed, 1985; Moore and Taleb, 1999; El-Sawy, 2003; Beben and Stryczek, 2013; Elshimi et al., 2013). Nevertheless, in most of the reported studies, orthotropic shell elements were utilized to simulate the corrugated profile of the steel section. In addition, these studies investigated culverts with spans less than 16.0 m and considering corrugated profiles of depth up to 150 mm.

Existing design codes and standards require precise numerical simulation for special features soil-steel structures such as very large-span culverts and dual radii arched culverts (e.g. Canadian Highway Bridge Design Code (CHBDC, 2019); American Association of State Highway and Transportation Officials (AASHTO, 2019) LRFD Bridge Design specifications; Corrugated Steel Pipe Institute (CSPI, 2017) Handbook of Steel Drainage and Highway Construction Products). Several aspects of the numerical model could have a significant effect on the predicted stress resultants that are used in design. These aspects include: consideration of geometric nonlinearity; simulation of interface condition at steel-soil interface; proper constitutive modeling of the backfill soil; and consideration of construction stages for soil backfilling. Nevertheless, the present literature lacks qualitative investigation on the impact of these aspects on numerical simulation of soil-steel structures and there is no specific criteria provided in the current design codes and standards. In addition, all current design procedures and recommendations are based on Super-Cor steel sections with a total depth less 150 mm and structures' spans less than 20.0 m.

Katona et al. (1979) investigated the effect of modeling techniques of geometric nonlinearity and soil-steel interface on the predicted performance of buried structures. Their results demonstrated that the predicted stress resultants of the structure decreased by 2 to 6% when considering geometric nonlinearity and applying a reduction factor for the shear strength at the soil-structure interface. Meanwhile, Ramadan and El Naggar (2020) analyzed the response of large span reinforced concrete three-sided culverts with flexible top slab at service and ultimate load levels employing two- and three-dimensional linear and nonlinear finite element models. They concluded that the structure can be modeled as linear elastic material for the serviceability limit state, while the structure nonlinearity must

be considered for the ultimate limit state conditions. There is no similar evaluation for very large span soil-steel bridges.

The main objective of the current study is to investigate the performance of large-span Ultra-Cor soil-steel bridges subjected to single axle truck loading considering different soil cover heights. In addition, the influence of different modeling techniques on the predicted soil-structure performance is evaluated. In order to achieve these objectives, three-dimensional nonlinear FE model was established to simulate a load test on a full-scale 10.0 m span steel culvert under laboratory conditions. The FE model was validated by comparing the calculated deformations and circumferential bending moment with the measured responses. The same modeling approach and criteria were then used to simulate a 32.4 m span arched-steel culvert constructed using Ultra-Cor sections and subjected to single axle loading at different soil cover heights. Additional analysis is provided to highlight the impact of several modeling techniques on the predicted stress resultants and deformations of steel arched structures.

5.2 Numerical model validation

5.2.1 Experimental Details

Lougheed (2008) instrumented a 10.0 m span steel culvert and load tested it under controlled laboratory conditions. The culvert width and rise were 6.0 m and 2.4 m, respectively, and was placed in a test pit of 16.0 m wide, 8.0 m long and 4.0 m high. The corrugated profile of the 6.0 mm thick steel plates had a depth of 150 mm and pitch of 400 mm. Fig. 5-1 shows the geometry of the culvert, test pit and the corrugated profile of the steel plates. The culvert was backfilled using well-graded sand and gravel (SW) as per

ASTM D2487-06 (2006), with traces of fines, compacted just over 100% of its standard proctor maximum dry density. Uni-axial and bi-axial electrical foil resistance strain gauges were attached to the surface of the steel culvert at 56 positions, including at the crest, valley and the mid height of the straight portion of the web. The deformed shape of the steel culvert was reported by attaching 23 prisms to the steel culvert and monitored using electronic theodolite. The performance of the steel culvert was monitored under the influence of point loads on the steel structure, backfilling around the structure and plate loading above the crown of the structure under different cover heights. The steel structure was subjected to twenty-two experimental test by changing the cover heights and the position of the load above the soil surface. The data for all tests are reported by Loughheed (2008) and Mak et al. (2009).

The FE model was validated by comparing its results with the experimental results for service load tests of the culvert at three different cover heights. Tests C, D and E were conducted by applying a single axle beam at cover heights of 1.5 m, 1.0 m and 0.45 m, respectively. The loading configuration for the tests are shown in Fig. 5-1. The load is transferred to the soil surface through two steel plates with dimensions of 0.25 m X 0.6 m and spaced apart by 1.80 m. The structure was then subjected to vertical pressure on the steel pads with a maximum vertical force as specified in Table 5-1.

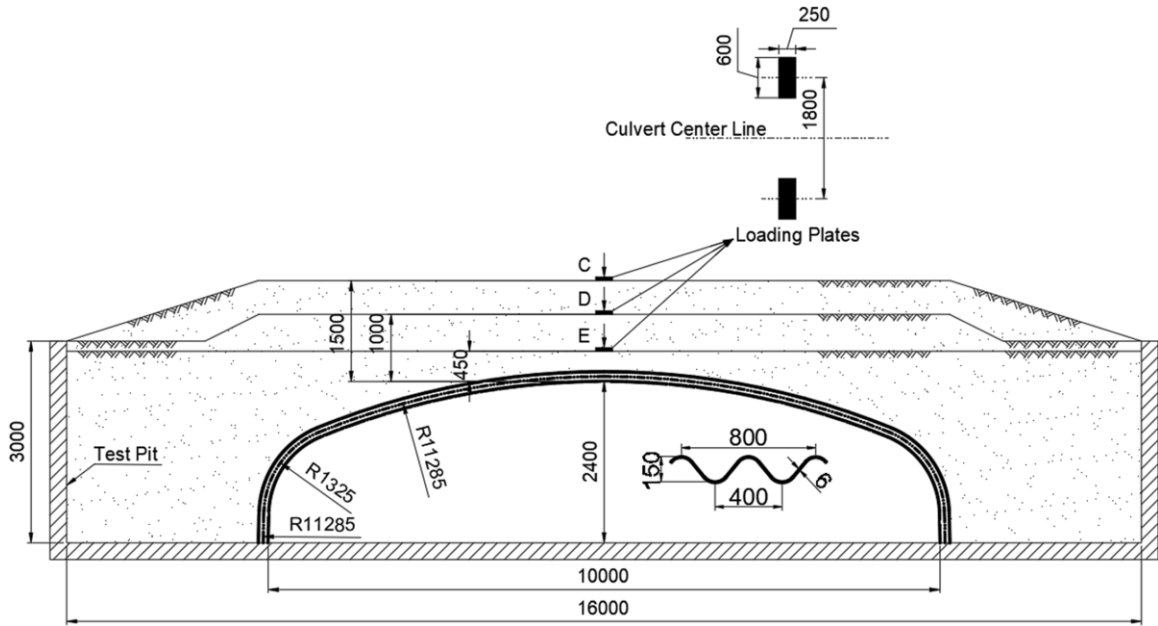


Fig. 5-1: Cross section for the test pit

Table 5-1: Summary for the Experimental Tests

Test Label	Cover Height (m)	Maximum Vertical Load (kN)
C1	1.50	197.80
D1	1.00	215.30
E1	0.45	234.50

5.2.2 Numerical Modeling

A three-dimensional finite element model was established using the finite element program Midas GTS NX (Midas GTS NX, 2019). Fig. 5-2 presents the numerical model geometry. The corrugated profile for the steel culvert was simulated using three-node and four-node shell elements. Four-node tetrahedron, six-node pentahedron and eight-node hexahedron solid elements were used to simulate the surrounding soil around the steel culvert. In total, the model comprised 221,442 elements. The vertical boundaries were restrained against horizontal displacements and the bottom boundary was fixed in all directions.

Von-Mises failure criterion was used to simulate the performance of the steel culvert and the Modified Mohr-Coulomb failure criterion was used to simulate the behaviour of the surrounding soil. The modified Mohr-Coulomb failure criterion considers the non-linear elastic behaviour, in addition to shear hardening of friction angle as a function of the plastic shear-strain. However, the modified Mohr-Coulomb model does not account for strain softening that may occur in the post peak region. Fig. 5-3 presents undrained triaxial compression test and direct shear test results conducted on similar type of backfill soil (Tarmac, 2018). The soil sample comprised 54% sand and 46% gravel, with less than 1% fines. The initial moisture content was 7.2% and initial unit weight of 22.4 kN/m³. The experimental data shows that the soil behavior did not exhibit significant strain softening in the post peak region. Furthermore, the maximum deviatoric stresses occurred at axial strain of more than 2.1%; however, the axial strain level measured in the current numerical analysis did not exceed 1.25%. According to the available experimental data, modified Mohr-Coulomb constitutive model is suitable for the current study. Relative movement was permitted between steel structure and surrounding backfill soil using interface elements, whose behaviour was simulated employing Coulomb-friction model. The stiffness and strength properties for the interface elements were taken as a ratio (0.6) of the surrounding soil properties (Allen et al., 1988; Midas GTS NX 2019). It should be noted that complete experimental setup involved 22 tests. In order to achieve accurate results for the three validated tests considered in the current study, staged construction analysis was applied including 49 construction phases for all the 22 experimental tests. Geometric nonlinearity was considered in the current study based on the updated Lagrangian formulation. Table 5-2 shows the material properties used in the numerical modeling for

both the steel culvert and the surrounding soil. The properties for the backfill soil was considered based on the data reported by Scott et al. (1977) and from laboratory test results performed on a similar type of granular soil (Tarmac, 2018).

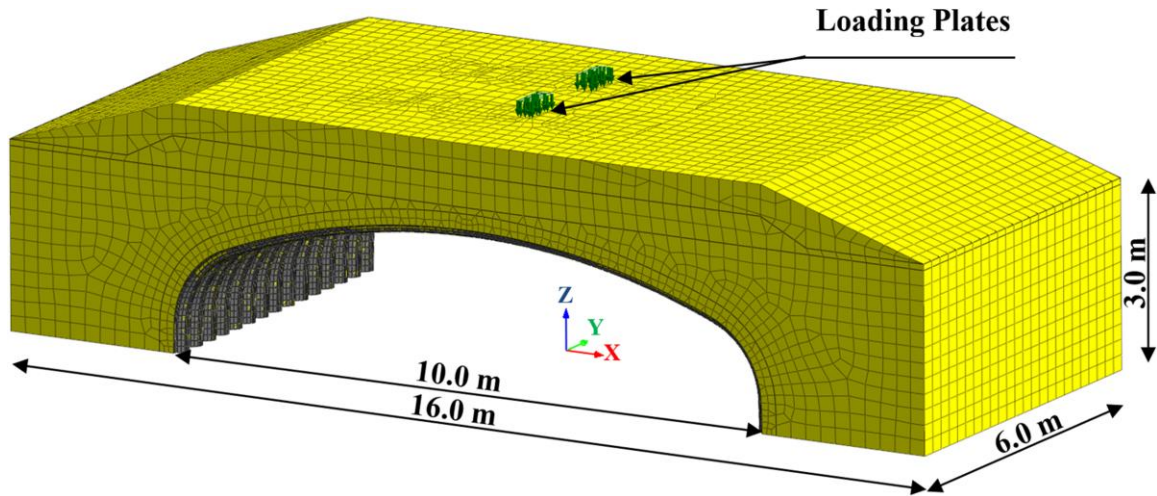


Fig. 5-2: Three-dimensional view for the numerical model

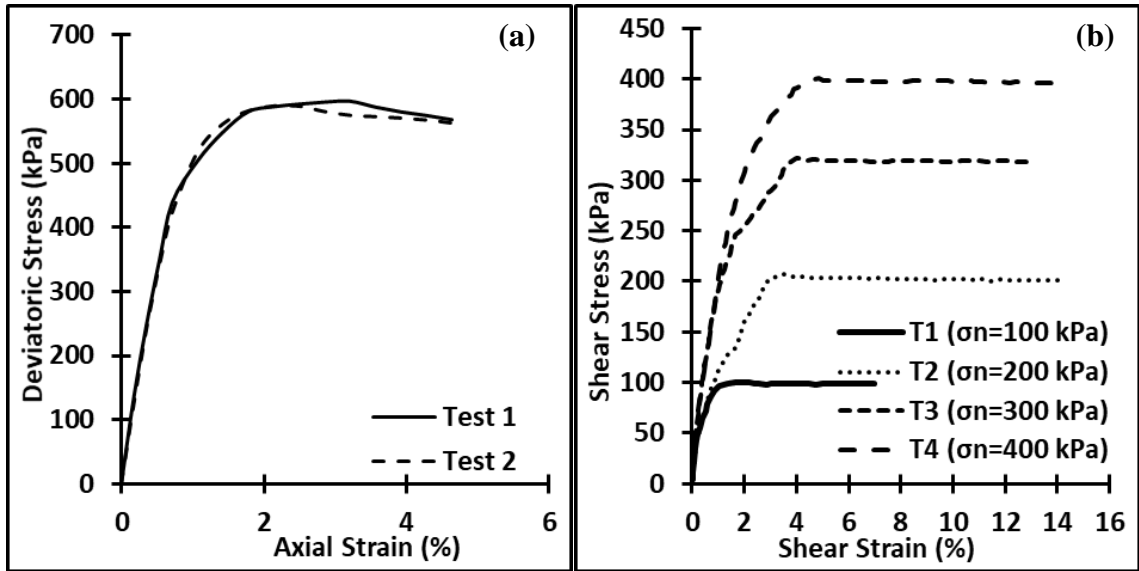


Fig. 5-3: Experimental data on backfill soil (a) undrained triaxial test; (b) direct shear test

Table 5-2: Summary for Soil and Structure material Properties

Name	Steel	Backfill Soil
Material Model Type	Von-Mises	Modified Mohr-Coulomb
Poisson's Ratio	0.3	0.3
Unit Weight (kN/m ³)	78.4	21.5
Secant Elastic Modulus in Loading (E) (MPa)	-	60
Elastic Modulus in unloading/reloading (E _{ur}) (MPa)	200000	120
Yield Stress (MPa)	275	-
Friction Angle (Degrees)	-	44
Dilatancy Angle (Degrees)	-	10
Cohesion (kPa)	-	3

5.2.3 Results from Validation of Numerical Model

The results of the numerical model for both stress resultants and deformations for the soil-steel bridges are compared with the experimental results in Fig. 5-4 and Fig. 5-5. Fig. 5-4 presents the vertical displacement at the crown just below the loading plate (i.e. at X=0 and Y=0.9 m) for the three load cases. As can be observed from Fig. 5-4, the numerical model successfully captured the same deformation pattern of the structure observed during the tests reported by Lougheed (2008). The maximum difference between the measured and calculated displacements was less than 15%. The results show that as the cover height varied from 1.50 m in test C1 to 1.0 m in test D1, there was no significant change in the vertical displacement at the crown. This is due to performing 8 truck loading tests on the cover height of 1.0 m before placing the additional 0.5 m and applying the C1 test, then removing again 0.5 m and conducting the D1 test. The preloading on the surface of cover height 1.0 m increased the stiffness of the soil-steel structure and deformed vertically close to the case of cover height 1.50 m. This preloading scheme was followed in the numerical model so as to evaluate the same structure performance. However, the vertical displacement increased significantly as the cover height decreased to 0.5 m in test E1. This

demonstrates that the general stiffness of the soil-steel structure under live loading increases as the cover height increases.

The circumferential bending moment was interpreted from the calculated axial stress values and measured axial strain values on the bottom side of both crest and valley of the corrugated steel plate. The circumferential bending moment values can be obtained assuming linear stress distribution between the crest and the valley, i.e.,:

$$M = \frac{\sigma_{crest} - \sigma_{valley}}{d} * I = \frac{\epsilon_{crest} - \epsilon_{valley}}{d} * EI \quad (1)$$

where: M is the circumferential bending moment in the steel section per unit length in the transverse direction; σ is the axial stress in the transverse direction; ϵ is the axial strain in the transverse direction; E is the elastic modulus of steel; d is the total depth of the corrugated profile; I is the moment of inertia per unit length in the transverse direction.

The calculated bending moment distribution was obtained along the unfolded length ζ of the steel structure and compared to the measured bending moment below the loading plate (i.e. $y=0.9$ m) as shown in Fig. 5-5. The calculated circumferential bending moment distribution along the steel structure in addition to the locations of maximum bending moment values agree well with the experimental observations. The difference between the numerical and measured circumferential bending moment was less than 10%. The maximum negative bending moment occurred at the crown, and positive bending moment started to occur at 1.5 – 2.0 m from the crown towards the shoulders. Furthermore, bending moment increased significantly as the soil cover height decreased.

The results discussed above collectively demonstrate the ability of the adopted three-dimensional FE modeling approach to simulate the performance of deep corrugated arched soil-steel bridges under the effect of live loading on the ground surface.

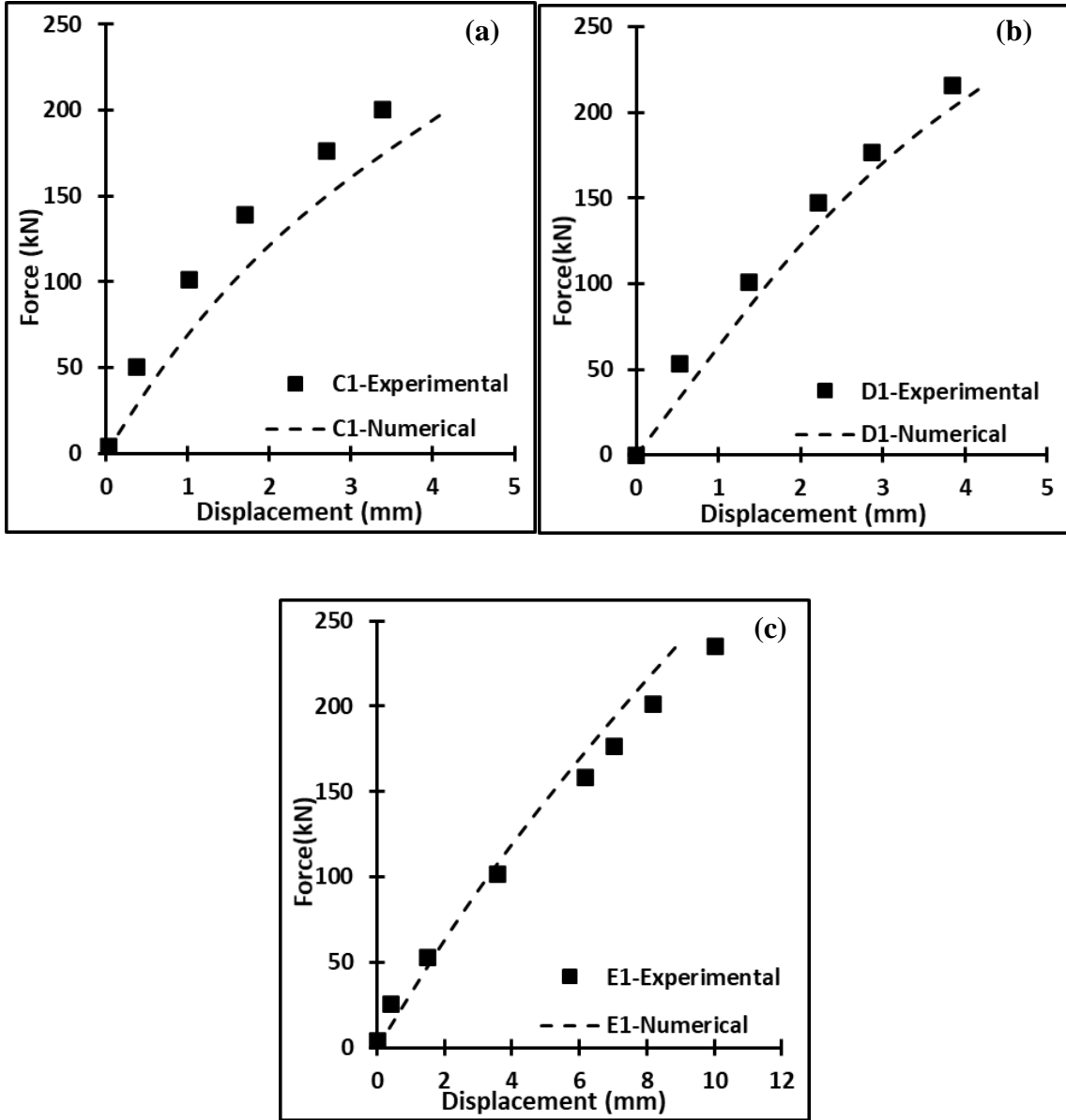


Fig. 5-4: Applied force vs. vertical displacement for test (a) C1; (b) D1; (c) E1

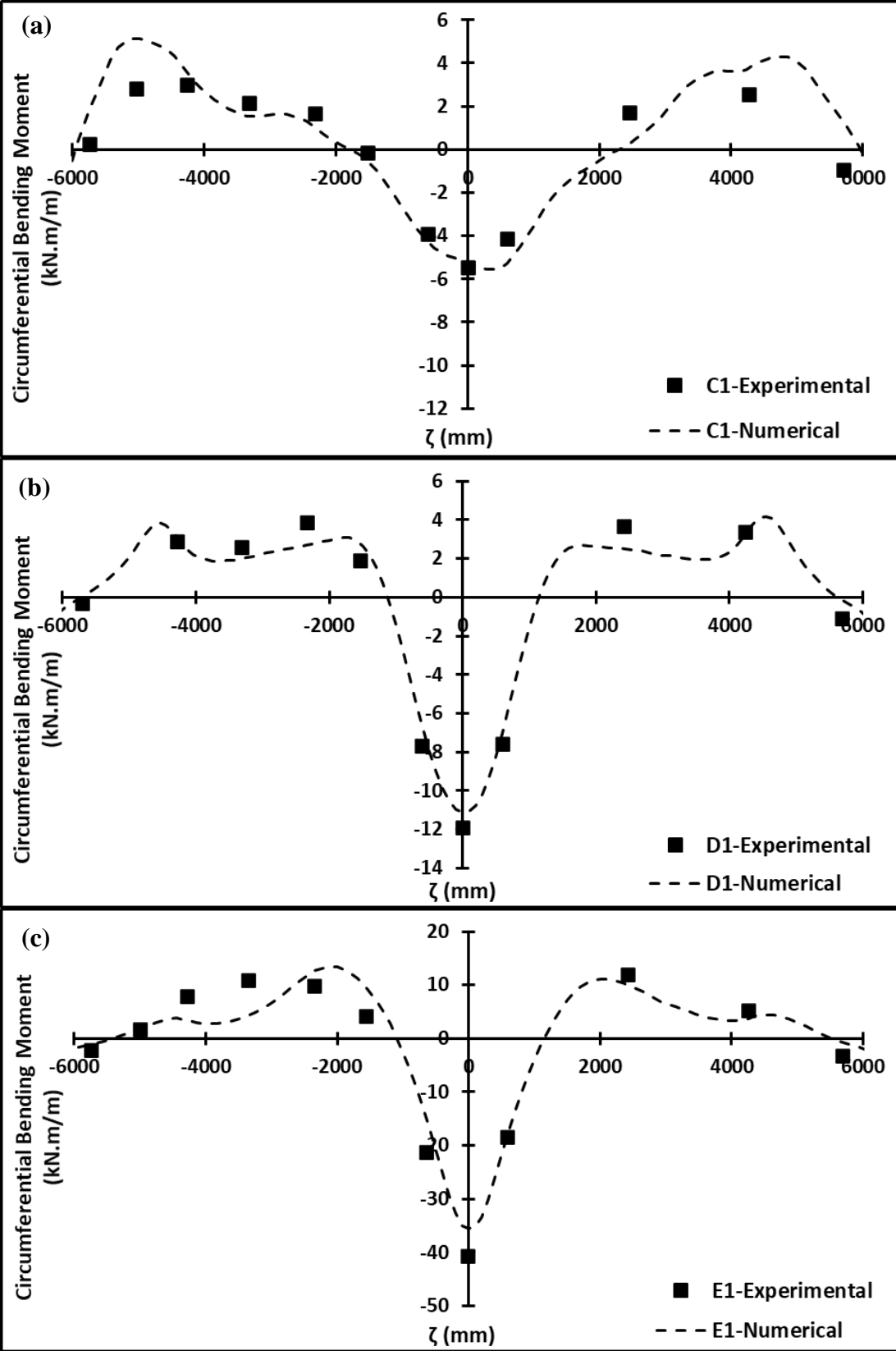


Fig. 5-5: Circumferential bending moment under test (a) C1; (b) D1; (c) E1

5.3 Ultra-Cor soil-steel bridge

5.3.1 Numerical Modeling

The validated numerical modeling approach (i.e. considerations of geometric nonlinearity, soil-steel interface condition, soil constitutive model and construction stages) is employed herein to investigate the performance of large span arched steel culvert considering the deepest corrugation profile currently available, known as Ultra-Cor. The structure configuration considered in the current study was implemented in the construction of the world's largest span arched steel culvert, which was erected in Dubai, UAE, in 2019. The span of the steel structure is 32.39 m and its rise is 9.57 m, and width is 12.0 m. The corrugated steel plates are 12.0 mm thick and have a profile of 500 mm pitch X 237 mm depth.

Three-dimensional nonlinear finite element model was established to simulate the corrugated profile of the steel plates along with the soil cover as shown in Fig. 5-6. Von Mises failure criterion and modified Mohr-coulomb failure criterion were used to simulate the nonlinear behaviour of the steel and soil backfill, respectively. The material nonlinearity for the interface elements was defined using Coulomb-friction model. The stiffness and strength properties for the interface elements were taken as a ratio of the surrounding soil properties and this ratio was assumed to be 0.6 (Allen et al., 1988; Midas GTS NX 2019). The same material properties shown in Table 5-2 were used in the analysis. The structure was subjected to vertical applied force equivalent to the maximum single axle load of a standard five-axle truck load CL-625-ON specified in Canadian Highway Bridge Design Code (CHBDC, 2019). The single axle load of 175 kN was chosen and

magnified by the Dynamic Load Allowance (DLA) as a function of the cover height following the equation below with 0.1 as the lowest value:

$$P_{LL} = P(1 + DLA) \quad (2)$$

$$DLA = 0.4(1 - 0.5D_E) \quad (3)$$

Where, P_{LL} is the live load vertical pressure; P is the live load pressure below the wheels; DLA is the dynamic load allowance; D_E is the distance between the ground surface and the highest point of the structure. Table 5-3 presents the applied vertical force and the cover height for each test.

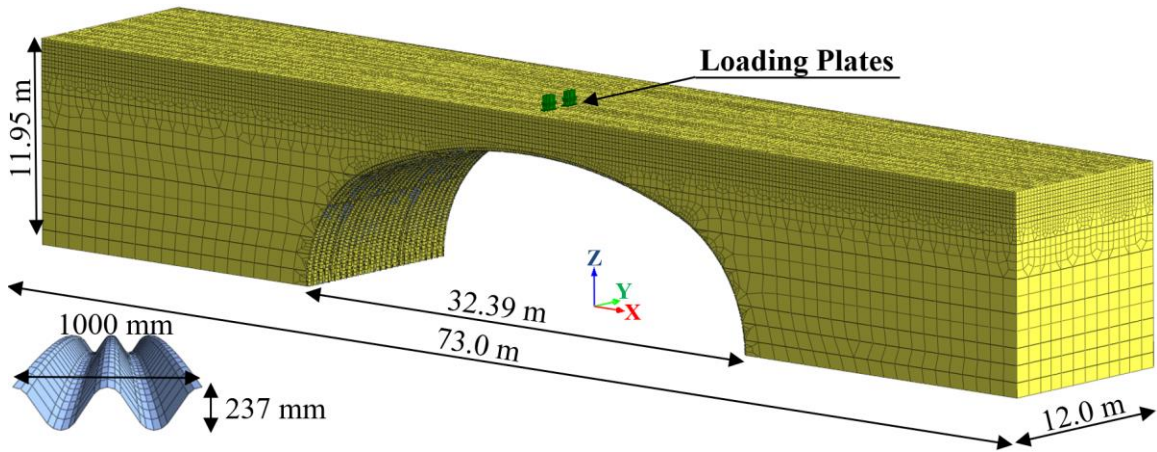


Fig. 5-6: Three-dimensional view for the numerical model using Ultra-Cor section

Table 5-3: Summary for the Numerical Tests

Test Label	Cover Height (m)	Dynamic Load Allowance (DLA)	Maximum Vertical Pressure (kPa)
U1	0.60	0.28	746.67
U2	1.00	0.2	700
U3	1.40	0.12	653.33
U4	1.80	0.1	641.67
U5	2.20	0.1	641.67

5.3.2 Results

Fig. 5-7 displays the calculated axial stress distribution at the bottom side of both crest and valley of the steel section along the applied load strip for different soil cover heights. The results demonstrate that the maximum compressive axial stress in the steel section occurs for the case of soil cover height of 0.6 m and decreases as the cover height increases in a nonlinear pattern. The results are used to estimate both circumferential bending moment and thrust distribution along the horizontal folded distance of the culvert. Fig. 5-8 shows the variation of the maximum circumferential bending moment and thrust on the steel structure due to live load with cover height. The maximum stress resultants are reduced by about 50-60% as the cover height increases from 0.60 m to 1.40 m. The minimum depth stated in the Canadian Highway Bridge Design Code (CHBDC, 2019) and in the American Association State Highway and Transportation Officials (AASHTO, 2019) is 0.6 m. The difference between the maximum stress resultants of 1.4 m and 1.0 m soil cover thickness ranges between 30 and 35%.

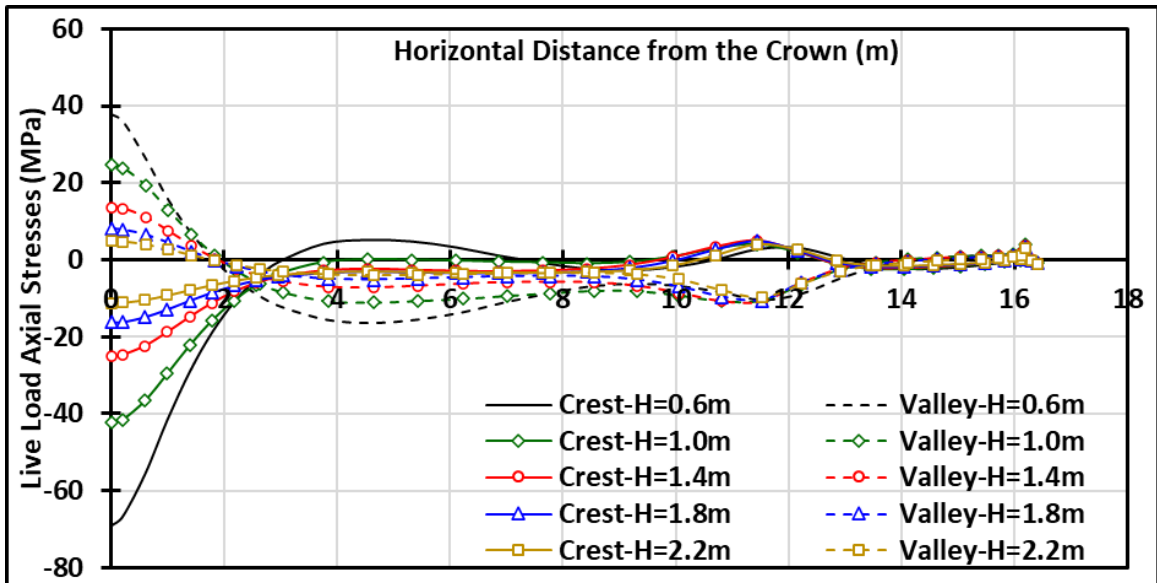


Fig. 5-7: Vertical stress distribution due to live load

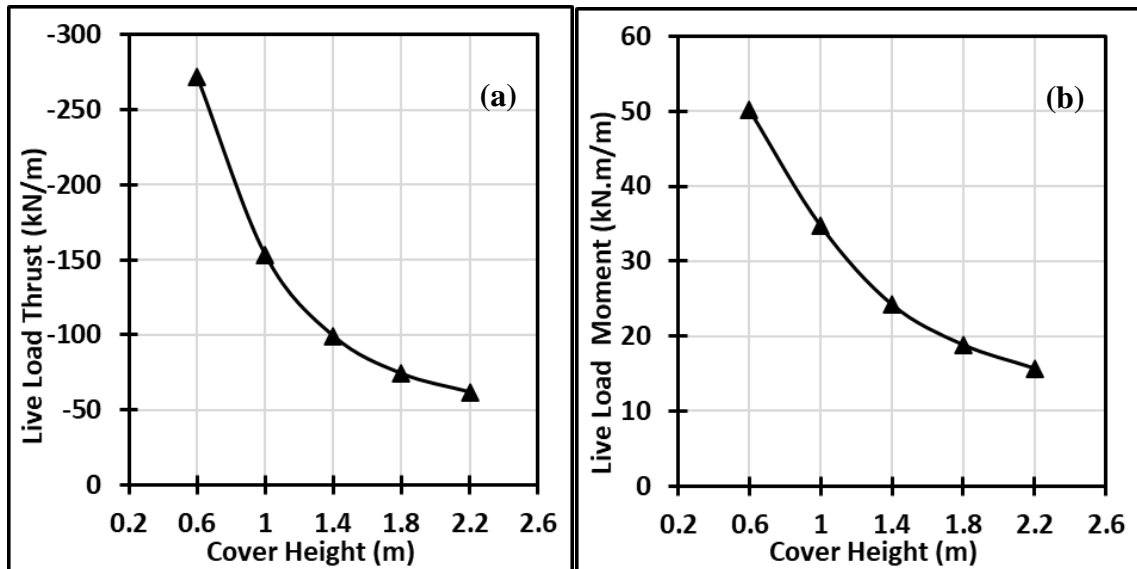


Fig. 5-8: Stress resultants variation due to live load (a) axial thrust; (b) bending moment

The vertical stress contours under the effect of axle loading are shown in Fig. 5-9. There is no overlapping in the vertical stresses at the ground surface from the two vertical loads, but overlapping appears at a depth of 0.4 m from the ground surface. The vertical stress distribution in the soil is plotted in Fig. 5-10. One of the methods used to estimate the axial thrust and bending moment design values stated in the CHBDC (CHBDC, 2019) depends on distributing wheel loads on a rectangular area using the empirical method, i.e., 1V:1H (1 vertical to 1 horizontal) in the transverse direction and 2V:1H in the longitudinal direction. The calculated vertical stress distribution was compared to the empirical method, and it was found that the calculated stress values are higher than that calculated by the empirical method by about 40%. The calculated vertical stress distribution is also compared with the method of 2V:1H for both longitudinal and transverse directions as shown in Fig. 5-10. For the first 0.6 m, the calculated stress values are higher than those calculated by the empirical method. However, the 2V:1H vertical stress distribution better describes the

numerical results and represents the upper bound for all stress values below the top 0.6 m cover fill.

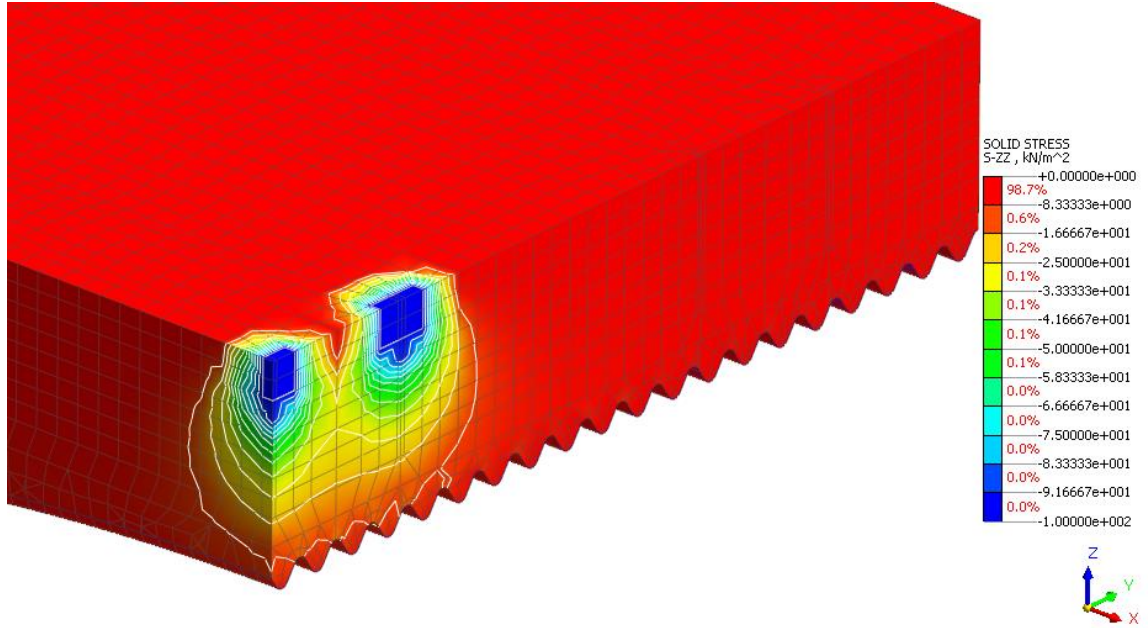


Fig. 5-9: Vertical stress distribution due to live load

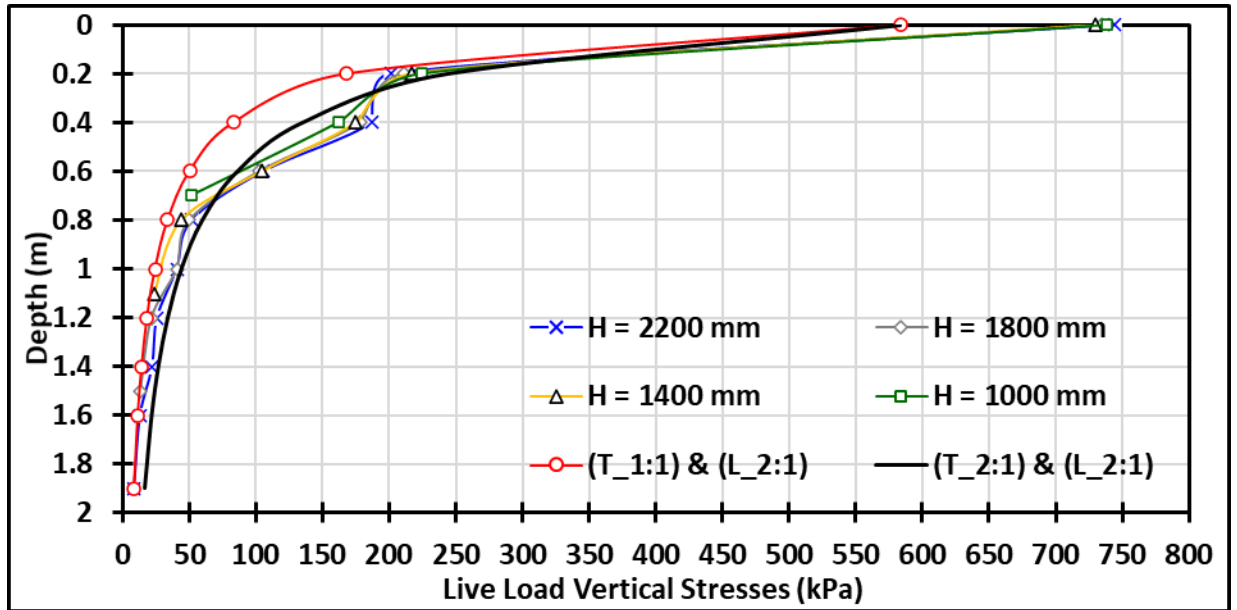


Fig. 5-10: Vertical stress distribution with Depth

5.4 Effect of different modeling techniques on predicted response

It is important to implement appropriate modeling methods and material constitutive models to accurately evaluate the performance and stress resultants for any soil-structure system. Therefore, the 3D FE model described above is employed to evaluate the impact of geometric nonlinearity, soil-structure interface model, construction stages and soil constitutive model on the predicted stress resultants and deformations of Ultra-Cor arched soil-steel bridges.

The effect of relative movement between steel structure and adjacent soil is simulated using interface plane elements with a strength reduction factor of 0.6 (Allen et al., 1988; Midas GTS NX 2019) and the obtained results are compared with the case of rigidly bonded interface. Both models involved construction stages analysis to account for backfilling; and simulated backfill soil behaviour employing modified Mohr-Coulomb failure criterion. Geometric nonlinearity is adopted in both models. Fig. 5-11 shows the percentage difference of axial compressive stresses at the crest, axial tensile stresses at the valley and the crown vertical deformation due to axle loading under several cover heights. Considering bonded soil-structure interface overestimates the vertical deformation by less than 2.5% while the axial stresses were underestimated by up to 4% at cover height 2.20 m.

The effect of geometric nonlinearity on the predicted response is evaluated by comparing the results obtained from numerical models with and without its consideration. The geometric nonlinearity is caused by the large deformations and large strains in the steel structure and is simulated employing updated Lagrangian FE formulation. Modified Mohr-

Coulomb failure criteria is used to simulate the backfill soil behaviour, and construction stages analysis is conducted to account for the backfilling process in both models. In addition, interface plane elements with a strength reduction factor of 0.6 is considered between steel structure and surrounding soil in both models. The impact of the geometric nonlinearity is not significant on the axial stresses of the structure with a maximum difference of 4.5% as shown in Fig. 5-11. However, neglecting geometric nonlinearity underestimates the crown vertical deformation values by up to 8% with linearly increasing pattern as the cover height increases. Katona et al. (1979) reported similar difference and underscored the importance of including geometric nonlinearity with large span culverts.

The effects of the adopted soil constitutive model on the predicted performance and stress resultants are evaluated by conducting two analyses: one considering the nonlinear behaviour of the backfill soil using Modified Mohr-Coulomb failure criteria; and one using the regular Mohr-Coulomb failure criteria. The Modified Mohr-Coulomb model considers the hyperbolic stress-strain curve in contrast to the regular Mohr-Coulomb that considers elastic-perfectly plastic curve. Moreover, the yield surface of the Modified Mohr-Coulomb depends on the shear and compression hardening that are used to model the irreversible strains and plastic strains, respectively. On the other hand, shear and compression hardening are not considered in the regular Mohr-Coulomb. Both models consider the construction stages for soil backfilling and soil-structure plane interface elements. In addition, both models account for geometric nonlinearity. Both axial stresses and deformations are affected greatly by the selection of soil constitutive model. Employing the Mohr-Coulomb material model overestimates both axial compressive and tensile stresses. The difference in the compressive stresses increases as the cover height increases

by up to 15% at the cover height 2.20 m, while the axial tensile stresses increase significantly reaching more than 60%. On the other hand, the crown vertical deformation values were underestimated by nearly 12%.

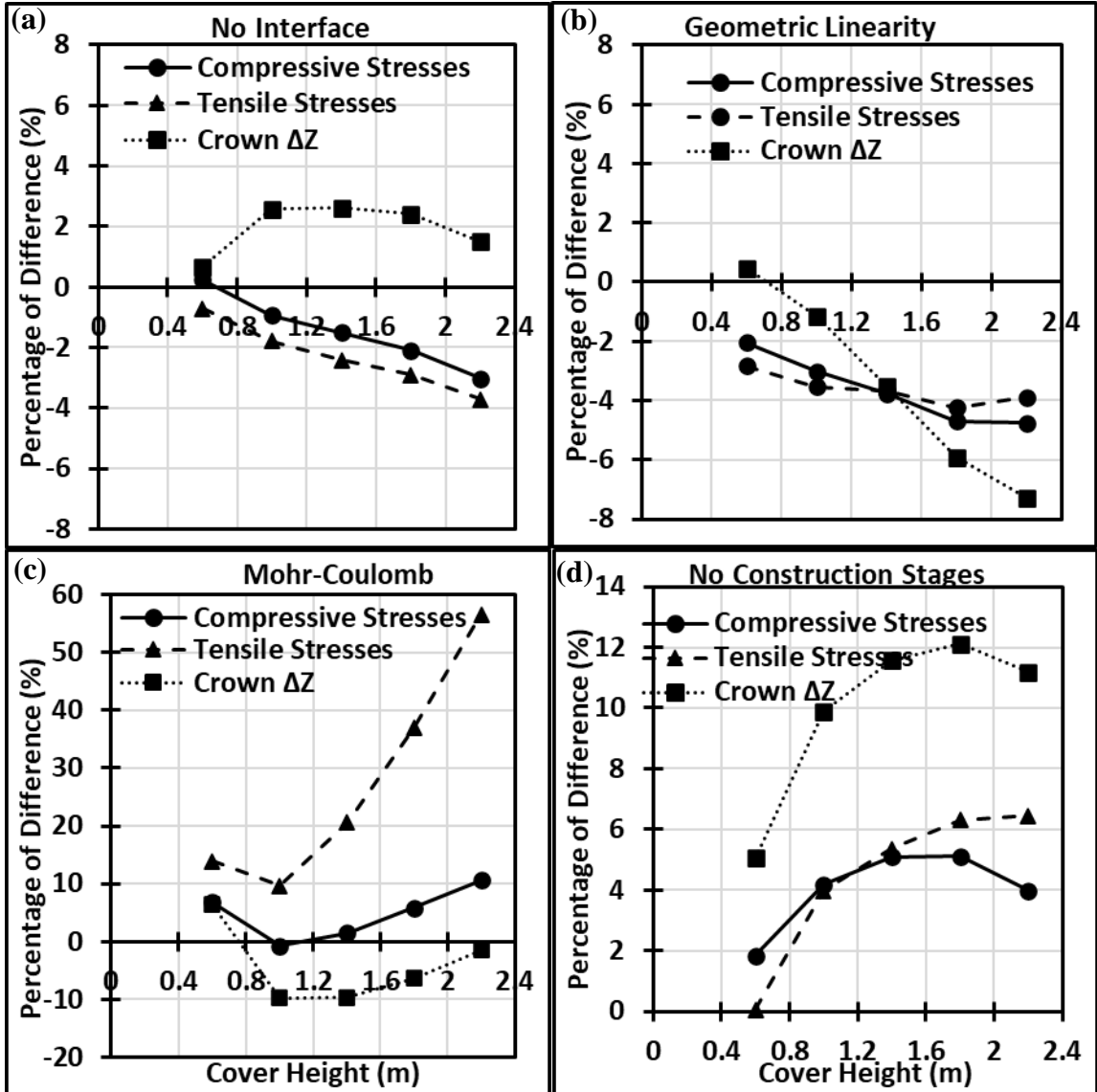


Fig. 5-11: Percentage difference in axial stresses and deformations for different soil cover heights for (a) modeling interface conditions; (b) consideration of geometric nonlinearity; (c) soil constitutive model; (d) consideration of construction stages

Finally, the influence of considering construction stages for backfilling before loading the structure in the analysis is evaluated. One analysis is conducted considering construction

stages of the soil backfill while the other starts the first stage with the structure already backfilled, and the truck load is applied in the next stage. Modified Mohr-Coulomb constitutive model is employed for simulating the behaviour of backfilling soil and the soil-structure interaction is counted in both models. In addition, geometric nonlinearity is considered in both models. The calculated axial stresses and deformations without consideration of construction stages are overestimated by up to 11% in comparison with the case including construction stages during the analysis. This difference tends to increase as the cover height increases.

Fig. 5-12 presents the crown vertical deformation below the loading plates at different construction stages subjected to axle loading and backfilling above the structure. During backfilling, the steel structure deformed upward, and the maximum upward deformation occurred at 9.57 m backfill height just before adding soil cover above the structure. The maximum upward deformation limit during construction should be less than 2% of the steel structure rise (CHBDC, 2019). Fig. 5-12 shows that the upward vertical deformation when using Mohr-Coulomb model reached 1.56% of the structure rise; however, the ratio did not exceed 0.3% in case of using modified Mohr-Coulomb constitutive model which is referred to as Reference Model. Although Mohr-Coulomb model underestimates the live load vertical deformation by nearly 12% only, the difference in upward vertical deformation exceeded 650% under the effect of soil backfilling.

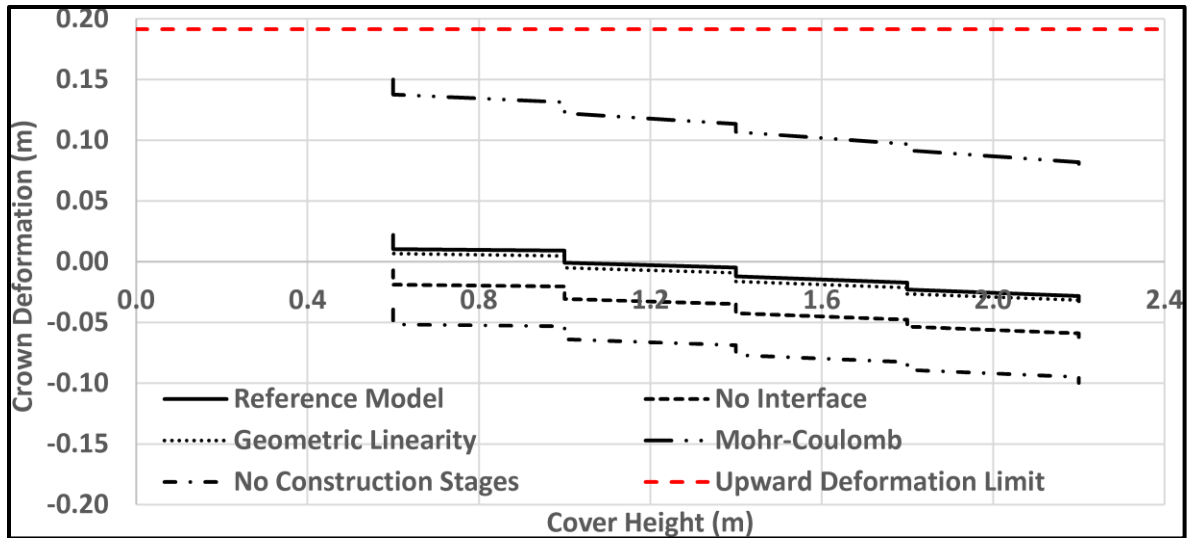


Fig. 5-12: Crown vertical deformation under different modeling techniques at different soil cover heights

Fig. 5-13 presents the calculated axial stresses in the steel structure. The large deformation of the steel structure calculated using the Mohr-Coulomb model led to higher axial compressive and tensile stresses in the steel as shown in Fig. 5-13. The calculated axial stresses in the steel section reached up to 75% of the yielding stresses (275 MPa) when using the Mohr-Coulomb model under the effect of one axle loading. However, the maximum stresses did not exceed 40% when using the modified Mohr-Coulomb constitutive model. From previous results, Mohr-Coulomb model shows that with the increase of number of truck axles, the calculated axial stresses may incorrectly increase significantly, which could have a serious impact on the design of soil-steel structures. Geometric nonlinearity had the least impact on the performance of the soil-steel response; however, not considering the geometric nonlinearity when large deformations occurred may lead to more than 30% difference in the axial stress values under earth load.

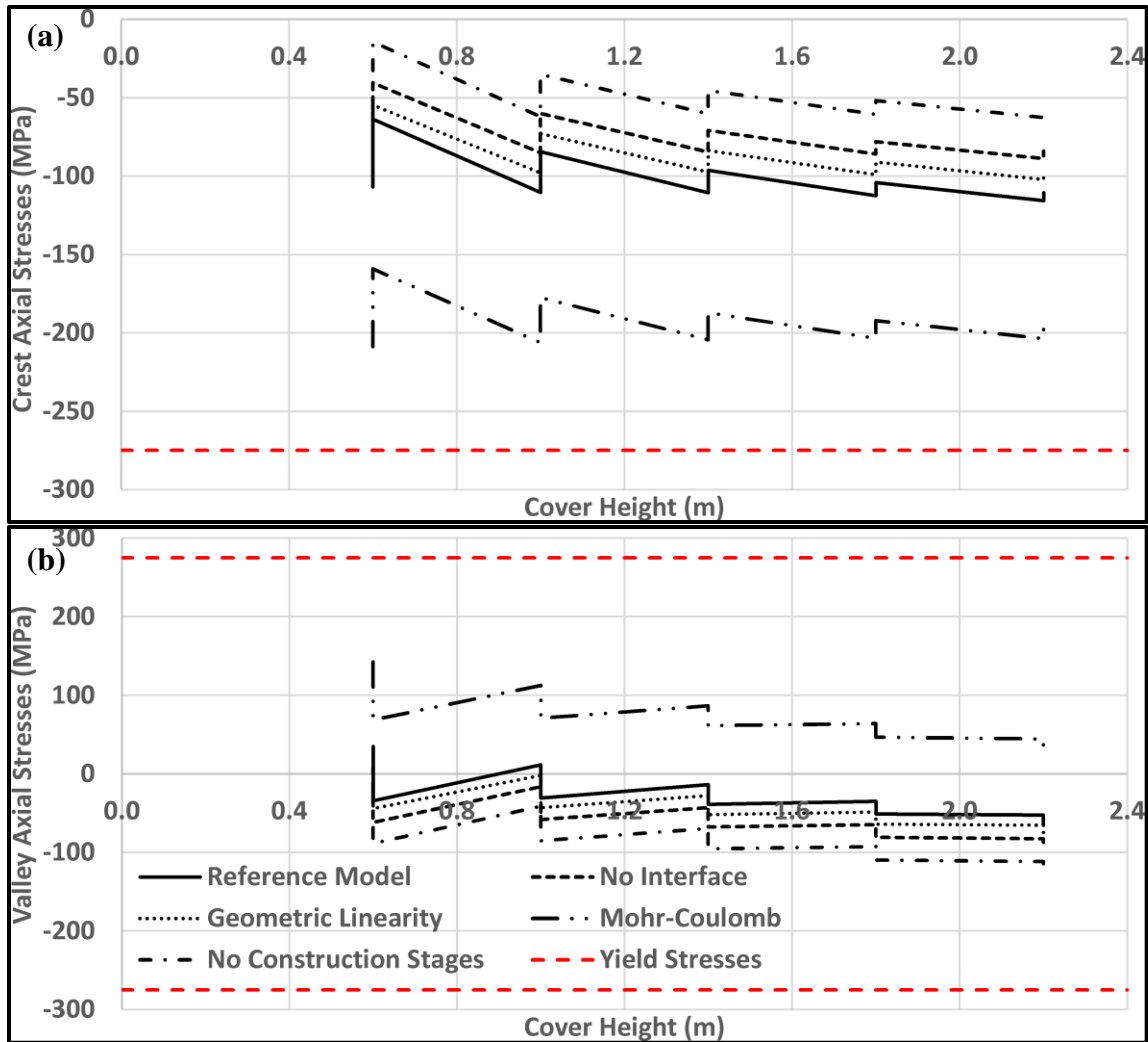


Fig. 5-13: Crown axial stresses under different modeling techniques at different soil cover heights at (a) crest; (b) valley

5.5 Conclusion

The performance of large-span arched steel culvert constructed with Ultra-Cor corrugated profile was investigated under the impact of truck single axle loading. A three-dimensional finite element model was validated with the results of full-scale tests of a 10.0 m span box culvert (Mak et al., 2009). The calculated response and stress resultants were in good agreement with the observed experimental results of the full-scale culvert with a maximum difference of 10% and 15% for the measured circumferential bending moments and

deformations, respectively. The validated modeling approach was then employed to evaluate the influence of truck axle loading on a very large span culvert that was constructed in Dubai, UAE. The results demonstrated the significant effect of the cover height on the stress resultants of the steel structure. The vertical stress distribution for axle loading was evaluated and a ratio of 2V:1H was recommended as an upper bound for analyzing large-span soil-steel bridges subjected to live loading.

The effect of different modeling techniques on the numerical results due to live loading was then investigated. It was found that the geometric nonlinearity could cause an increase of 4% and 8% in axial stresses and deformations, respectively. Furthermore, slippage at soil-structure interface could increase axial stresses by up to 4%. It was also found that using the simplified linear elastic-perfectly plastic soil model with Mohr-Coulomb could overestimate the axial stress by up to 60%, which could significantly affect the total stress resultants of the steel structure. Finally, lack of consideration of construction stages before applying the live load overestimates the predicted axial stresses and deformations by about 11%.

5.6 References

- AASHTO (American Association of State Highway and Transportation Officials). 2019. AASHTO LRFD Bridge Design Specification, customary U.S. units, 7th Ed. Washington, D.C.: AASHTO
- Allen, R. L., J. M. Duncan, and R. T. Snacio. 1988. "An engineering manual for sheet pile walls." Blacksburg, VA: Department of Civil Engineering, Virginia Tech.

- ASTM D2487-06. 2006. "Standard Practice for Classification of Soils for Engineering Purposes (Unified Soil Classification System)." ASTM International, West Conshohocken, PA. DOI: [10.1520/D2487-06](https://doi.org/10.1520/D2487-06)
- Beben, D. and A. Stryczek. 2016. "Numerical analysis of corrugated steel plate bridge with reinforced concrete relieving slab." *Journal of Civil Engineering and Management*, 22 (5), 585-596. DOI: <https://doi.org/10.3846/13923730.2014.914092>
- CHBDC (Canadian Highway Bridge Design Code). 2019. Canadian Standards Association. CAN/CSA-S6-14., Mississauga, ON.: CHBDC
- CSPI (Corrugated Steel Pipe Institute). 2017. Handbook of Steel Drainage and Highway Construction Products, Canadian Edition, Cambridge, ON.: CSPI.
- Elshimi, T. M., R. W. I. Brachman, and I. D. Moore. 2013. "Effect of truck position and multiple truck loading on response of long-span metal culverts." *Can. Geotech. J.* [dx.doi.org/10.1139/cgj-2013-0176](https://doi.org/10.1139/cgj-2013-0176)
- El-Sawy, K. 2003. "Three-dimensional modeling of soil-steel culverts under the effect of truckloads." *Thin-walled Structures*, 41, 747-768. DOI: [https://doi.org/10.1016/S0263-8231\(03\)00022-3](https://doi.org/10.1016/S0263-8231(03)00022-3)
- Flener, E. B. 2010. "Testing the response of box-type soil-steel structures under static service loads." *Journal of Bridge Engineering*, 15, 90-97. DOI: [https://doi.org/10.1061/\(ASCE\)BE.1943-5592.0000041](https://doi.org/10.1061/(ASCE)BE.1943-5592.0000041)

- Girges, Y. and G. Abdel-sayed. 1995. "Three-dimensional analysis of soil-steel bridges." Canadian Journal of Civil Engineering, 22, 1155-1163. DOI: [10.1139/195-133](https://doi.org/10.1139/195-133)
- Lougheed, A. 2008. "Limit states testing of a buried deep-corrugated large-span box culvert." M.S. thesis. Kingston, ON, Canada : Department of Civil Engineering, Queen's University. <http://hdl.handle.net/1974/1663>
- Katona, M. 1978. "Analysis of long-span culverts by the finite element method." Transportation Research Board 678, Transportation Research Board, Washington D.C. 59-66.
- Katona, M., D. Meinhert, R. Orillac, and C. Lee. 1979. "Structural evaluation of new concepts for long-span culverts and culvert installations." Washington, D.C.: FHWA
- Machelski, C., G. Antoniszyn, B. Michalski. 2006. "Live load effects on a soil-steel bridge founded on elastic supports." Studia Geotechnica et Mechanica, 28, 2-4, 65-82
- Mak, A. C., R. W. I. Brachman, I. D. Moore. 2009. "Measured response of a deeply corrugated box culvert to three dimensional surface loads." In Proc., Transportation Research Board Annual Conference, Washington, D.C.: TRB, 09-3016
- Midas GTS-NX. 2020. <https://www.midasoftware.com/geo/gtsnx/products/midasgtsnx>

- Moore, I. and B. Taleb. 1999. "Metal culvert response to live loading performance of three-dimensional analysis." Transportation Research Board 1656, Transportation Research Board, Washington D.C. 37-44
- Moore, I. and R. Brachman. 1994. "Three-dimensional analysis of flexible circular culverts." Journal of Geotechnical Engineering, 120 (10), 1829-1844. DOI: [https://doi.org/10.1061/\(ASCE\)0733-9410\(1994\)120:10\(1829\)](https://doi.org/10.1061/(ASCE)0733-9410(1994)120:10(1829))
- Ramadan, S. and M. H. El Naggar. (In press). "Field monitoring and numerical analysis of a large span three-sided reinforced concrete culverts." Journal of Geotechnical and Geoenvironmental Engineering, ASCE.
- Scott, J., G. Bauer and D. Shields. 1977. "Triaxial testing on a granular A aggregate." Ontario Joint Transportation and Communications Research Program, ON. Project O-1
- Tarmac. 2018. "Construction and Execution of Emirates Road at RAK." Project No. R/7078-311906/77/2016. Dubai, UAE

6 Ultimate Capacity of Large-Span Soil-Steel Structures

6.1 Introduction

Soil-steel structures (SSS) have been used widely in the mining industry to withstand significant vertical loading in haul roads and railways. The weight of the mining equipment, rail loads, off-road trucks are much higher than standardized highway trucks stated in the design codes and standards. The weight of mining trucks has the tendency to reach up to 628 tonnes (Komatsu, 2019), while mining shovels exceeds one thousand tonnes weight (Petersoncat, 2013). Moreover, the soil cover above the buried structures and below the heavy equipment may exceed 20 m depending on the structure shape and loading conditions. Recently, a deep corrugation profile of 500 mm pitch and 237 mm depth has been developed to support higher loading conditions with larger spans (Williams et al. 2012). However, the ultimate capacity of SSS comprising such deep corrugated profile has not been investigated under both earth and truck loading.

Several full-scale load tests have been performed on SSS with spans up to 18.15 m to evaluate their performance under applied vertical loading (Lefebvre et al. 1976; Sargand et al. 1994; Webb et al. 1999; Beben and Manko 2008; Mak et al. 2009; Sanaeiha et al. 2017). Additional studies escalated the applied load to reach the ultimate capacity of the steel structure (Pettersson 2007; Loughheed 2008; Flener 2009; Wysokowski 2021). However, the spans of SSS that was subjected to ultimate loading conditions were less than 14.0 m and had corrugated profiles no deeper than 150 mm depth and 400 mm wavelength. On the other hand, limited studies investigated the ultimate capacity of SSS numerically. Elshimi (2011) simulated numerically 10.0 m span SSS under ultimate loading conditions.

The study demonstrated the importance of considering the geometry of corrugated profile in the numerical simulation in addition to large deformation geometrical nonlinearity. Wadi et al. (2020) conducted three-dimensional numerical simulation for SSS with 18.1 m span and 5.6 m rise. The thickness of the corrugated steel plates was 7.0 mm and soil cover of 700 mm was chosen. The study focused on applying tandem axles over the SSS at different locations and increasing the load up to failure to indicate the maximum capacity of the structural system. Meanwhile, Ramadan and El Nagggar (2021) investigated the ultimate capacity of reinforced concrete three-sided culverts under the effect of maximum backfill height. They varied the backfill height on three-sided culverts with large spans and evaluated the maximum backfill height at failure and explored the failure mechanism. Up to the authors' knowledge, there is no similar studies conducted on large-span SSS comprising the deep corrugation profile.

The current design codes and standards require limit states design of the steel structure under serviceability, fatigue, and ultimate limit states (CSA, 2019; AASHTO (2019) LRFD Bridge Design specifications; CSPI (2017) Handbook of Steel Drainage and Highway Construction Products). Evaluating the ultimate limit state for the safety of the steel cross-section and the configuration of the structure involves an interaction equation that combines the effects of bending moment and axial thrust, as well as maximum structure wall strength including global buckling factors. The interaction equation of the steel cross-section does not consider the structure instability that may be encountered by in-plane or snap-through buckling modes. The Swedish Design Method (Pettersson and Sundquist 2014) considers the second order effects of the axial forces acting on deformed members in amplifying the factored bending moment in addition to reducing the axial capacity of

the cross-section to account for the flexural buckling. With the use of mining shovels of gross weight exceeding one thousand tonnes and structure spans larger than 30 meters, it is essential to investigate the ultimate capacity of the steel structure considering the buckling factors in the interaction equation.

The current study presents three-dimensional finite element analyses for large-span SSS utilizing the deepest corrugation profile and subjected to ultimate loading conditions. The numerical modeling technique was validated through comparisons with full-scale test data for a 10.0 m span SSS subjected to tandem axles under ultimate loading. The same modeling technique was used to investigate the performance of 32.4 m span SSS under the maximum backfill height and ultimate truck loading. The critical stress resultants of the steel structures at the ultimate case were compared to CHBDC (CSA, 2019) and AASHTO (AASHTO LRFD, 2019) ultimate limit states. The results and observation obtained from the conducted analyses were used to propose a conservative and applicable interaction equation for large-span SSS accounting for buckling effects.

6.2 Numerical Model Validation

6.2.1 Experimental Details

Lougheed (2008) investigated the performance of large-span box culvert under serviceability and ultimate limit states. The structure had a span of 10.0 m, longitudinal width and rise of 6.0 m and 2.4 m, respectively. The steel structure was assembled from corrugated profile using 6.0 mm thick steel plates, and 150 mm x 400 mm (depth x pitch). The structure was placed in a rectangular test pit of 16.0 m X 8.0 m, and 3.0 m depth as shown in Fig. 6-1. The backfill soil surrounding the steel culvert was well-graded sand with gravel (SW) per ASTM D2487-06 (2006), with traces of fines. The backfilling was

completed in lifts no more than 300 mm and compacted to over 100% of its standard proctor maximum dry density. The deformations of the steel structure were monitored using an electronic theodolite with accuracy of ± 0.2 mm. In addition, the axial strains were recorded by attaching 56 uni-axial and bi-axial electrical foil resistance strain gauges at the bottom surface of the structure. The SSS was subjected to truck loading, single axle and tandem axle, at different cover heights as listed in Table 6-1. A total of twenty load tests were conducted within the serviceability limit range. The load in each axle was transferred to the soil surface above the steel structure through two steel plates with dimensions of 0.25 m X 0.6 m and spaced apart by 1.80 m. The deformations and axial strains of the steel structure were presented by Loughheed (2008). The ultimate capacity of the steel structure was investigated later by escalating the applied vertical load above the structure until failure. However, a bearing capacity failure in the soil cover occurred below the loading plates at a vertical load of 800 kN (Test E5a). Test E5b was then conducted using larger bearing plates of 0.37 m X 0.95 m and the structure behavior was recorded until failure occurred in the steel structure at a total vertical load of 1100 kN.

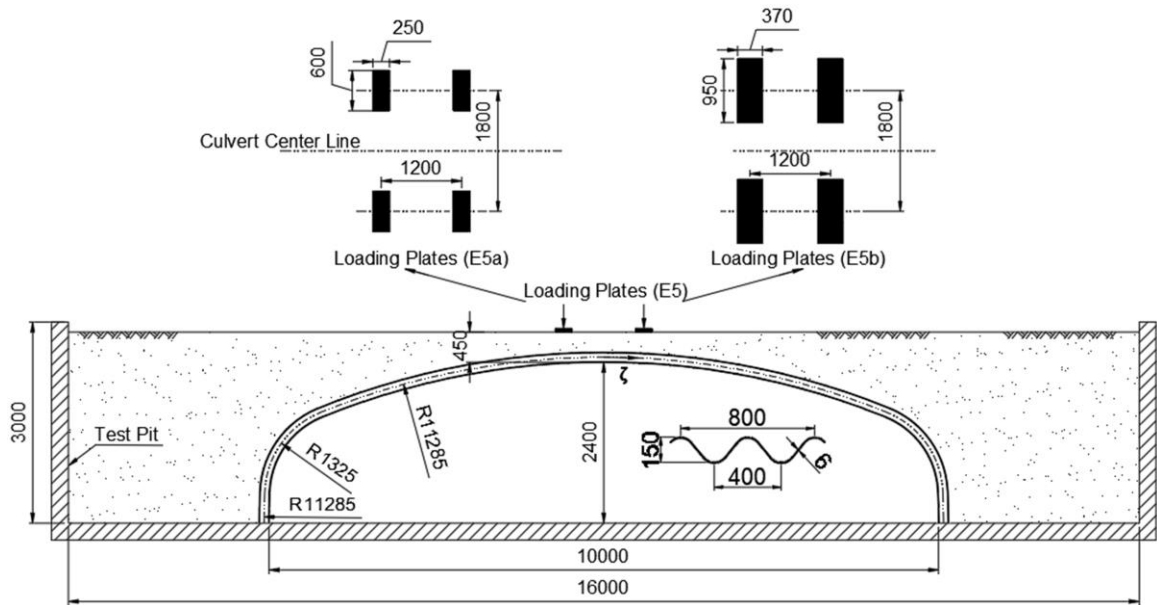


Fig. 6-1: Cross-section for the test pit

Table 6-1. Summary for Test Scheme

Test	Cover Height (m)	Axle Type	Offset from Structure Center (m)	Applied Load (kN)
A1/A2	No backfill	Single	0	30/40
B1-8	1.046	Tandem-axle truck	-6.0 – 1.0	240
C1/C2	1.507	Single/Tandem	0	197.8/275
D1/D2	1.0	Single/Tandem	0	215.3/328.4
D3/D4	1.0	Single/Tandem	-2.0	215.3/328.4
E1/E2	0.45	Single/Tandem	0	234.5/351.4
E3/E4	0.45	Single/Tandem	-2.0	234.5/351.4
E5a	0.45	Tandem	0	800
E5b	0.45	Tandem	0	1100

6.2.2 Numerical Modeling

Three-dimensional finite element model was established using the finite element program Midas GTS NX (Midas GTS NX, 2019). The actual corrugated profile for the steel culvert was simulated using three-node and four-node shell elements. Four-node tetrahedron, six-node pentahedron and eight-node hexahedron solid elements were used to simulate the surrounding soil around the steel culvert. In total, the model comprised 221,442 elements.

The size and number of the elements used in the current study were determined based on sensitivity analysis. Geometric nonlinearity large deformation was considered during all construction stages. The vertical boundaries were restrained against horizontal displacements and the bottom boundary was fixed in all directions.

Von-Mises failure criterion and Modified Mohr-Coulomb failure criterion were used to simulate the behaviour of the steel structure and surrounding soil, respectively. The properties of the backfill soil were determined from experimental tests performed on similar soil sample and reported by Tarmac (2018). Table 6-2 presents the material properties used for the current study. The interface between the steel structure and surrounding soil was modeled using Coulomb-friction yielding criterion. The properties of the interface elements were obtained from the following recommended equations (Midas GTS NX, 2019)

$$K_n = \frac{E_{oed,i}}{t_v} \quad \& \quad K_t = \frac{G_i}{t_v}$$

$$C_i = R * C_{soil} \quad \& \quad \tan(\phi_i) = R * \tan(\phi_{soil}) \quad (1)$$

where, K_n & K_t are the normal and shear stiffness moduli, respectively; $E_{oed,i}$ is the oedometer elasticity modulus of interface; t_v is the virtual thickness (0.1); C_i and ϕ_i are the strength parameters of interface elements and estimated from multiplying R , which is the reduction factor and is assumed to be 0.6, by surrounding soil strength parameters, C_{soil} & ϕ_{soil} , (Allen et al., 1988; Midas GTS NX 2019).

As previously mentioned, the structure was subjected to twenty loading tests at different cover heights before subjecting it to the ultimate loading. The performance of the structure in the numerical model was recorded from two modeling strategies to highlight the influence of preloading the soil-structure. The first strategy considered all previously

applied service loading tests on the structure with a total of forty-nine construction stages and referred to as FFEM. The second strategy involved subjecting the SSS to the ultimate loading directly (i.e., without considering the prior service loading tests) referred to as UFEM. The performance of the soil-steel structure under the effect of service loading tests is reported in **Embaby et al. (2021)** (Chapter 5).

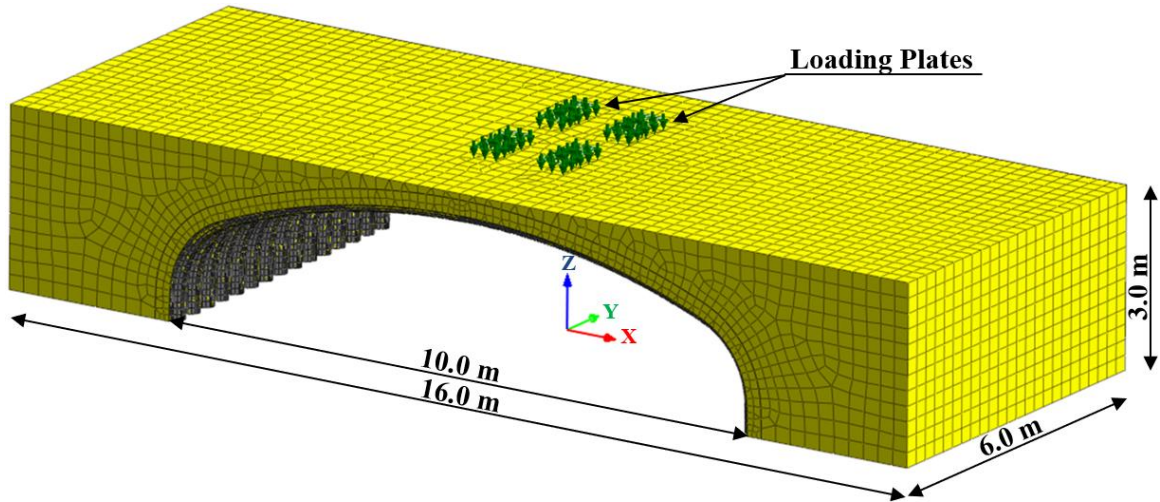


Fig. 6-2: Three-dimensional view for the numerical model

Table 6-2. Summary for Soil and Structure Material Properties

Name	Steel	Backfill Soil
Material Model Type	Von-Mises	Modified Mohr-Coulomb
Poisson's Ratio	0.3	0.3
Unit Weight (kN/m ³)	78.4	21.5
Secant Elastic Modulus in Loading (E) (MPa)	-	60
Elastic Modulus in unloading/reloading (E _{ur}) (MPa)	200000	120
Yield Stress (MPa)	300	-
Friction Angle (Degrees)	-	44
Dilatancy Angle	-	10
Cohesion (kPa)	-	3

6.2.3 Validation Results and Discussion

The validation process was conducted by comparing the measured and calculated curves of the applied load-vertical displacement at the structure crown (between the two loading

plates) for both loading tests (E5a & E5b). Figs. 6-3 compare the calculated and measured load-displacement curves. Figs. 6-3 demonstrate that the FE model successfully captured the performance of the structure and the maximum plate-loading capacity. The behaviour calculated by simulating all prior loading tests before applying the ultimate loads (FFEM) was in a better agreement with the measured results, compared with the case of simulating the ultimate loads only (UFEM). Fig. 6-3a shows that the stiffness (i.e., slope of the load-displacement curve) of the soil-steel structure in case of UFEM is approximately 40-45% of the case of FFEM during the initial loading increments. This difference is because the model in case of FFEM was subjected to several service loads including test E2 which had the same load pattern (tandem axle) and applied load of approximately 44% of the applied load in test E5a. The preloading of the system using same load patterns led to densification in the backfill soil below the loading plates, and thus, stiffer behavior during the initial loading increments of test E5a. Nevertheless, the difference between FFEM and UFEM decreased to 25% as the applied load increased to 800 kN. The backfill soil in both models was experiencing the additional applied load from test E5a for the first time, and therefore, closer soil behavior at the final loading increments.

With the change of loading plates in case of E5b, the calculated stiffness of the soil-steel structure from FFEM was overestimated because the calculated vertical displacement was 22% less than the measured values as shown in Fig. 6-3b. The difference in case of E5b may be attributed to (a) the bearing capacity failure in the full-scale test occurred in the soil cover which could have increased the plastic strain in the soil-steel structure; (b) the re-leveling and re-compacting of soil cover after the bearing failure and before applying E5b test led to disturbance in the preloaded soil below the loading plates, and consequently,

lower stiffness in the field results was observed; (c) the loading criteria in test E5b started with first load step of 800 kN at which test E5a ended that may have led to additional deformation in the steel structure and more flexible behavior than that in the numerical model; (d) each load increment was kept constant for 30 minutes to identify creep strains and deflections in the structure. The numerical model could not simulate the previously mentioned conditions due to software convergence limitations and the absence of creep yield surface in the used constitutive models. However, despite the limitations in the numerical simulation, the FE models captured the ultimate load capacity of the soil-steel structure reasonably well. This is because the ultimate capacity of the SSS depends mainly on the stability of the steel structure and the capacity of the steel cross-section in resisting the induced stress resultants, which were not affected by the preloading condition differences in both models. Fig. 6-3b also shows that the difference in the structure stiffness between FFEM and UFEM decreased to 30%. The lower difference is because part of the soil below the larger loading plates was not subject to the prior service loading tests. In this case, the difference between FFEM and UFEM would be less than the expected difference between two modeling criteria.

The numerical model was further validated by comparing the calculated and measured circumferential bending moments along the periphery of the structure. The bending moment distribution was compared at the section below the loading plates (i.e., $Y=0.9$ m). The calculated bending moment profiles from both FFEM and UFEM were close to each other at the final step of tests E5a and E5b with differences less than 5%. The results obtained from the FFEM model were considered in the comparison with the measured bending moment distribution. The bending moment values were estimated for both

experimental and FFEM in addition to axial thrust values for the FFEM by assuming linear stress distribution along the cross-section of the corrugation profile, i.e.:

$$M = \frac{\sigma_{crest} - \sigma_{valley}}{d} * I = \frac{\epsilon_{crest} - \epsilon_{valley}}{d} * EI \quad (2)$$

$$N = \frac{\sigma_{crest} + \sigma_{valley}}{2} * A = \frac{\epsilon_{crest} + \epsilon_{valley}}{2} * EA \quad (3)$$

where: M is the circumferential bending moment in steel section per unit length in the transverse direction; N is the axial thrust per unit length in the transverse direction; σ is the axial stress in the transverse direction; ϵ is the axial strain in the transverse direction; E is the elastic modulus of steel; d is the total depth of the corrugated profile; I is the moment of inertia per unit length in the transverse direction; A is the cross-sectional area per unit length in the transverse direction.

The assumption of linear stress distribution is based on considering the axial stress values at the crest and the valley only and neglects the nonlinearity along the corrugation profile. Fig. 6-4 shows the circumferential stress distribution across the corrugated steel plates at the crown and shoulder in case of test E5b. Fig. 6-4 examines the validity of assumption of Linear Stress Distribution (LSD) in comparison with the actual Nonlinear Stress Distribution (NSD). It can be observed that the nonlinearity in the axial stress distribution increases towards the crown (i.e., $\zeta=0$). This is attributed to the yielding of the zone below the loading plates first before propagating towards the shoulders of the structure. Accordingly, the Nonlinear Stress Distribution (NSD) along the steel cross-section and the updated corrugated profile at the ultimate case were considered in determining the actual bending moment (M_{actual}) and axial thrust (N_{actual}) values, i.e.:

$$M_{actual} = \int \sigma_i * t_i * b_i * dy \quad (4)$$

$$N_{actual} = \sum \sigma_i * t_i * b_i \quad (5)$$

where: σ_i is the circumferential stresses at each element in the corrugation profile; t_i & b_i are the thickness and breadth of each element; y is the distance from the element to the centroid of the section.

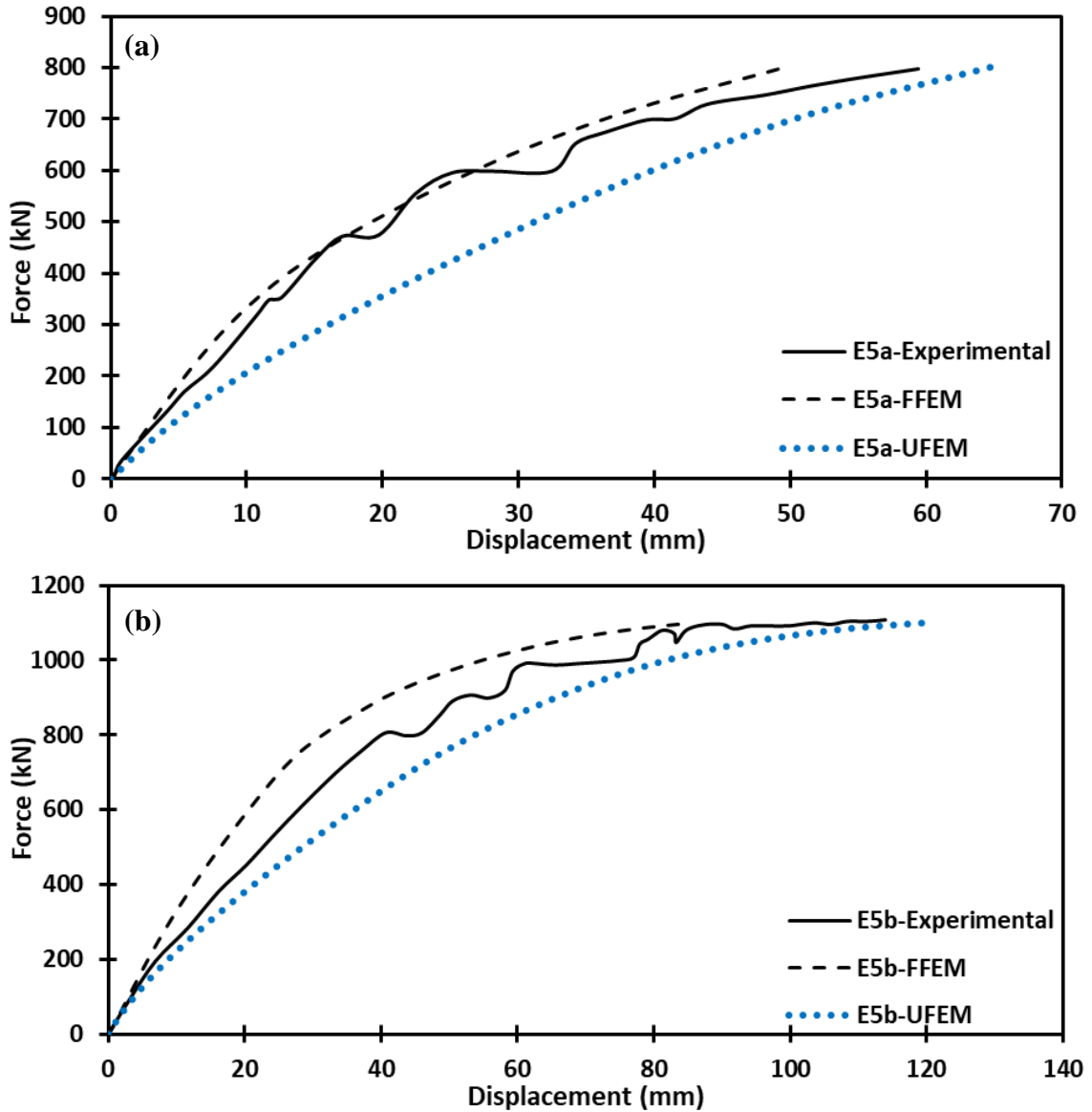


Fig. 6-3: Load-displacement relationship for test (a) E5a; (b) E5b

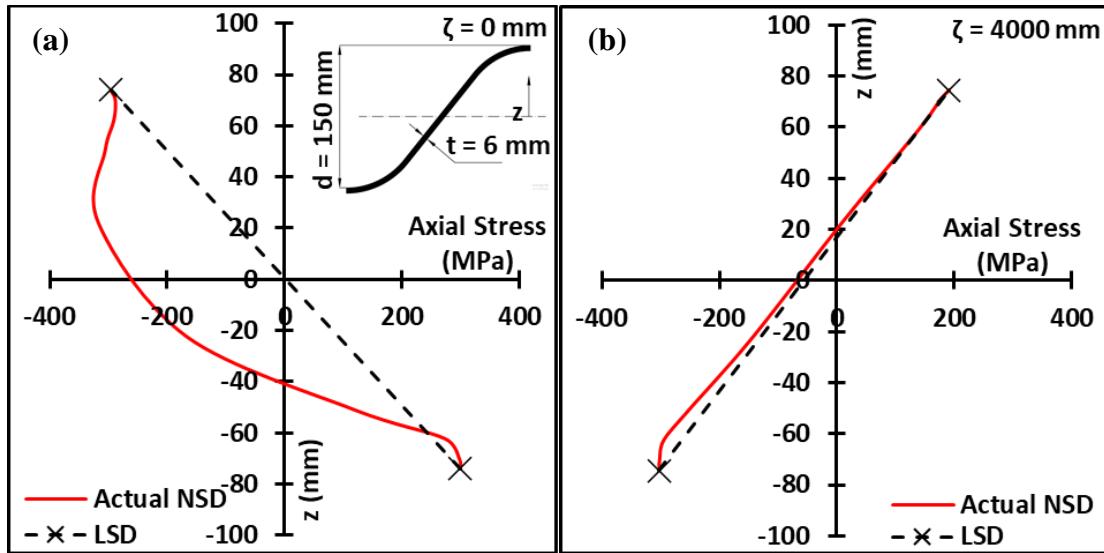


Fig. 6-4: Circumferential stress distribution in case of test E5b at (a) crown ($\zeta=0$); (b) shoulder ($\zeta=4.0$ m)

Fig. 6-5 presents the circumferential bending moment distribution along the folded length of the steel structure. The calculated bending moment distribution using LSD assumption agreed with the experimental results since the same assumption was used in calculating the bending moment values. Nevertheless, both calculated and measured LSD overestimated the bending moment values by up to 30% in comparison with calculated bending moment considering the NSD. The reason for this difference can be explained by inspecting the axial thrust distribution along folded length of the steel structure as shown in Fig. 6-6. At the crown, the LSD method significantly underestimated the axial thrust due to reaching yield stress on both tension and compression sides of the cross-section, leading to average value of nearly zero. The high compressive stresses in the actual distribution leads to lower bending moment values around the centroid of the section. The actual axial thrust decreases as the distance from the crown increases, which reduces the difference in estimated bending moment values employing the LSD and NSD methods. The maximum plastic strength of

the corrugated section in bending moment (M_p) and axial thrust (N_p) can be estimated from the following equations:

$$M_p = Z * \sigma_y \quad \& \quad N_p = \sum \sigma_y * t_i * b_i \quad (6)$$

where: σ_y is the yield strength of the steel material; Z is the plastic section modulus of the corrugated profile (390.4 mm³/mm). The maximum calculated bending moment at the crown is 84 kN.m/m, which is 72% of the plastic moment capacity of the steel section (M_p is taken as 117.12 kN.m/m). On the other hand, the maximum computed axial thrust is 1030 kN/m, which is 44% of the section ultimate capacity (N_p is taken as 2478 kN/m). The combined effect of both bending moment and axial thrust due to unfactored loads is evaluated using CHBDC (CSA, 2019) and AASHTO (AASHTO LRFD, 2019) method without reducing the section resistance capacity, i.e.

$$\left[\frac{N}{N_p} \right]^2 + \left[\frac{M}{M_p} \right] \leq 1.0 \quad (7)$$

The calculated value employing the interaction equation (Eq. 7) provided is 0.91. Thus, the structure failed before reaching the unity value of the interaction equation. To further investigate the cause of failure, the unfactored induced stresses along the structure cross-section is compared with the section compression strength accounting for the structure global buckling utilizing equation (8) provided by the CHBDC (CSA, 2019) and equation (9) provided by AASHTO (AASHTO LRFD, 2019). The equation provided by CHBDC (CSA, 2019) relates to inelastic behavior of the conduit wall when the wall radius of curvature R_{curv} less than equivalent radius R_e , i.e.,:

$$f_b = \Phi_t F_m \left[\sigma_y - \frac{(\sigma_y K R)^2}{12 E r^2 \rho} \right] \quad (8)$$

$$f_b = \frac{1.2 \phi_b C_n (EI)^{\frac{1}{3}} (\phi_s E_s K_b)^{\frac{2}{3}} R_h}{A} \quad (9)$$

where CHBDC (CSA, 2019) parameters, f_b is the maximum compressive stresses in the structure wall; ϕ_t is resistance factor for compressive strength (taken = 1.0); F_m is a reduction factor for modifying buckling stresses in case of multiple structures; K is a factor representing relative stiffness between structure and surrounding soil; R is the structure rise; r is the radius of gyration of the structure wall; ρ is a reduction factor for buckling stresses. While AASHTO (AASHTO LRFD, 2019) parameters ϕ_b is resistance factor for general buckling; C_n is scalar calibration factor for nonlinear effects (0.55); I is moment of inertia for structure wall; ϕ_s is resistance factor for soil; E_s is modulus of elasticity for backfill soil; K_b is factor based on Poisson's ratio (0.44); and R_h is a correction factor for backfill geometry.

The comparison demonstrates that the induced axial compressive stress ($\sigma = 121.1 \text{ MPa}$) does not exceed the maximum wall strength in equation (8) ($f_b = 157.9 \text{ MPa}$), neither that in equation (9) ($f_b = 411.56 \text{ MPa}$). The maximum induced axial compressive stress is 76% of capacity of the structure wall calculated by CHBDC equation (CSA, 2019) and 30% of that calculated by AASHTO equation (AASHTO LRFD, 2019). The results demonstrate that the current limit state equations require further evaluation for its applicability to large span SSS.

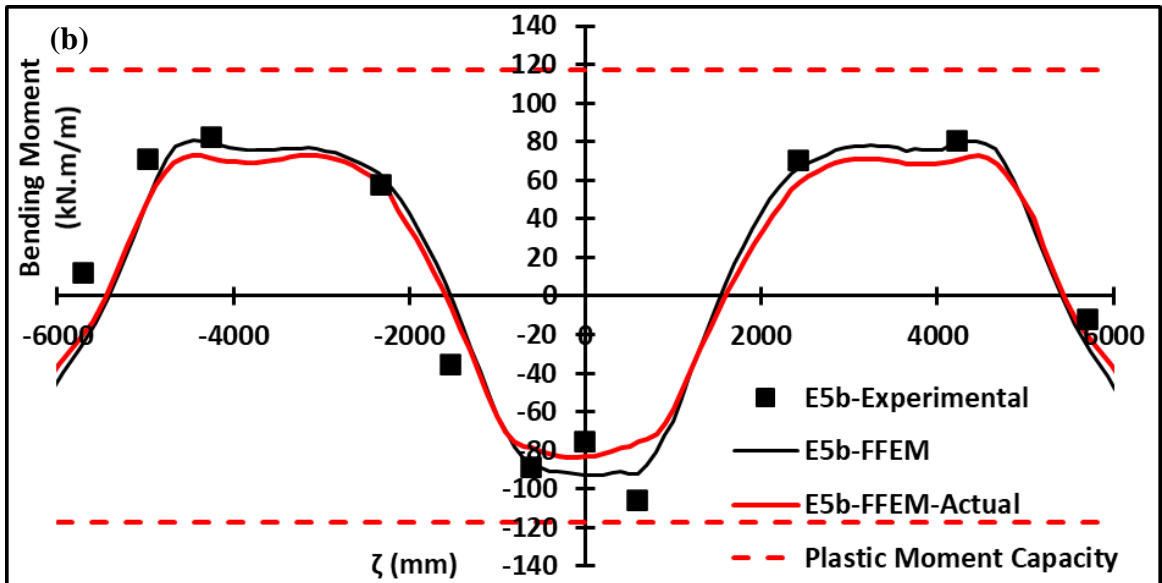
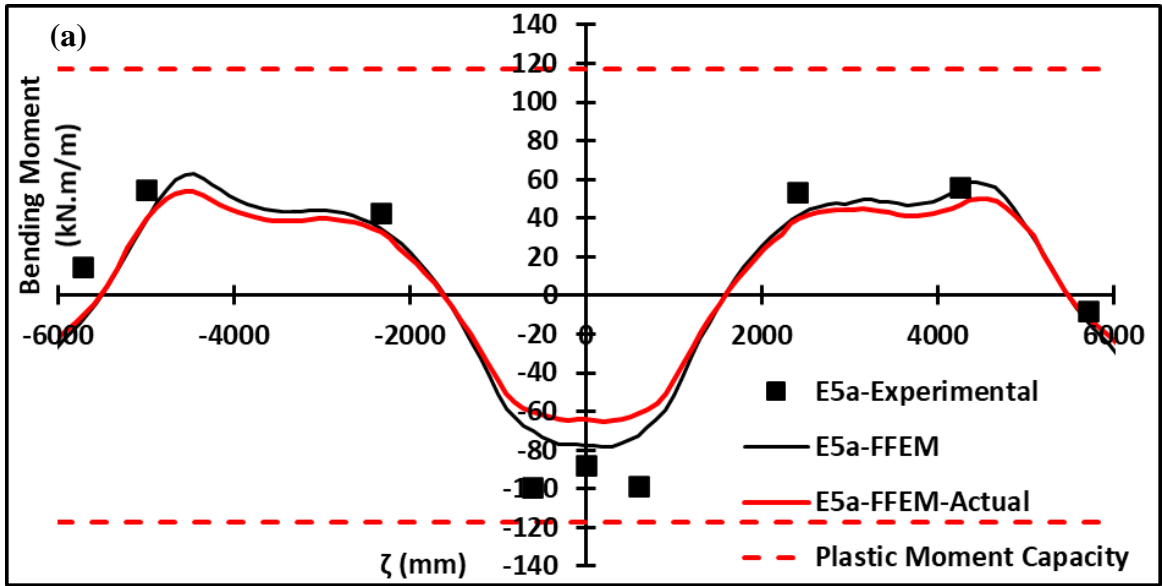


Fig. 6-5: Bending Moment Distribution for test (a) E5a; (b) E5b

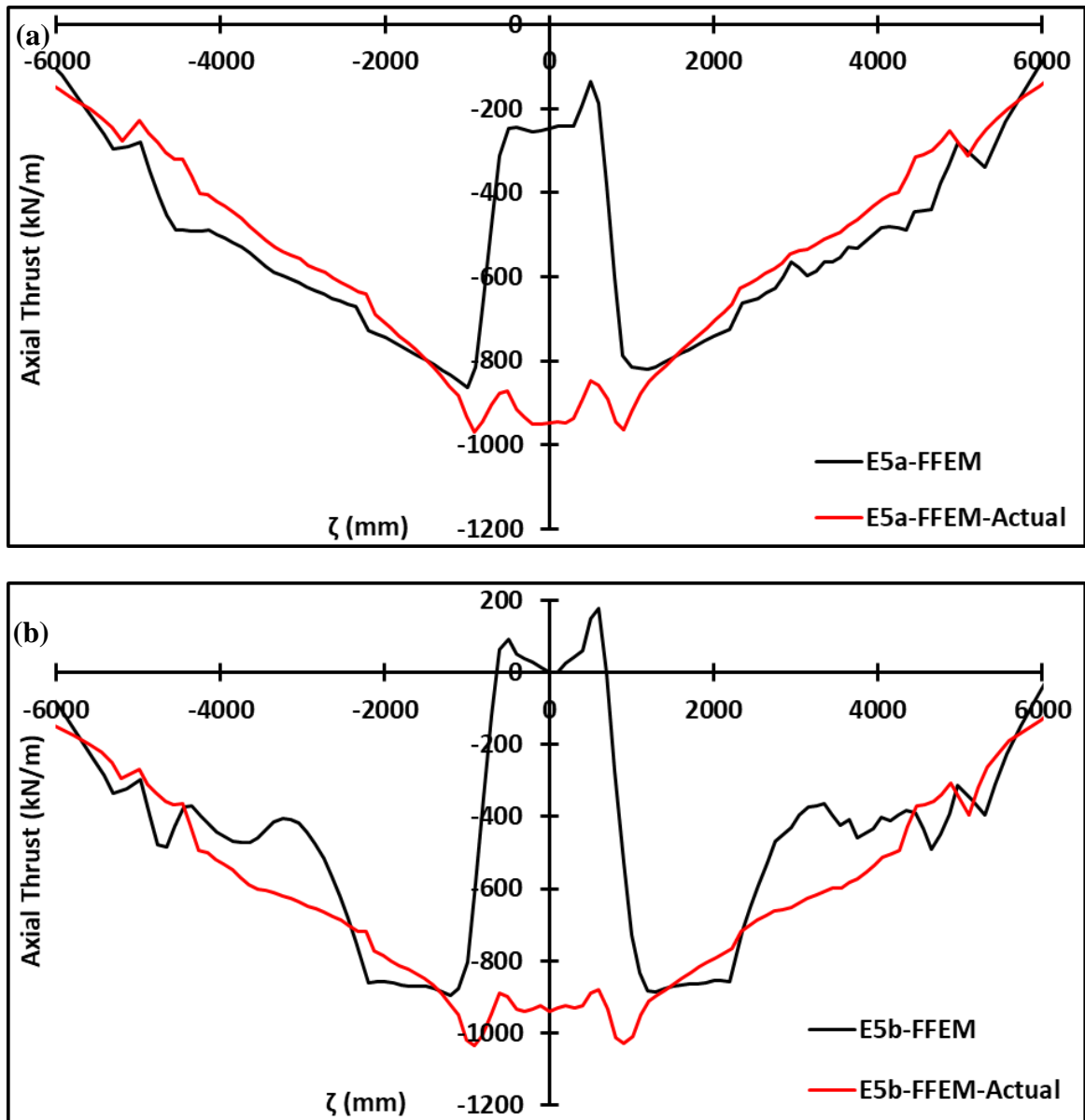


Fig. 6-6: Axial Thrust Distribution for test (a) E5a; (b) E5b

6.3 Large-Span Soil-Steel Structure

The ultimate capacity for SSS comprising the deepest corrugation profile, i.e., 237 mm X 500 mm, is investigated in this section employing the validated numerical technique and the NSD in calculating the induced stress resultants. The investigation involved two steps. First, the ultimate flexural capacity of the deepest corrugation profile was evaluated without the influence of backfill soil through laboratory full-scale test conducted at

Waterloo university, Canada. A specimen of 9.54 mm thick plate with the deepest corrugated profile was tested by applying four-point bending test. The ultimate flexural capacity was evaluated by comparing the measured stress resultants with the plastic moment capacity of the section. Second, the geometric configuration of the world's largest-span SSS, Shamal bridge (Embaby et al., 2022) (Chapter 3), was analyzed to evaluate the influence of the backfill soil. The span and height of the steel structure are 32.39 m and 9.57 m, respectively. The wall radius of curvature for the upper zone is 29.81 m, while that of the sides portion is 8.20 m. The thickness of the steel plates is 12 mm. The input parameters for backfill soil and steel elements considered in the analysis are those presented in Table 6-2. The yield strength for the steel material was taken as 430 MPa for the corrugated profile. The ultimate capacity of the SSS is evaluated by determining the maximum backfill height that can be sustained by the structural system representing the case of high induced axial thrust values in the steel structure. In addition, different truck loading conditions were applied at shallow cover heights representing the case of high induced bending moment values.

6.3.1 Maximum Flexural Capacity

Fig. 6-7 presents the setup of four point bending test performed on the deepest corrugated 9.54 mm steel plates and the corresponding three-dimensional finite element model developed to simulate the experimental test. Figs. 6-7a and 6-7b show the dimensions of the tested specimen and the configuration of the test. The vertical applied pressure was transferred from 2500 kN actuator to two loading beams through a spreader beam to ensure symmetric loading conditions on both loading beams. The tested specimen was rested on two pedestals with an inside-to-inside distance of 2.42 m that were clamped to the ground.

The inner dimension between the loading plates was 0.82 m. The performance of the corrugated steel plate was investigated by monitoring the vertical displacement at the middle of the test specimen under different applied load.

A three-dimensional finite element model of the test setup was developed as shown in Fig. 6-7c. The corrugated profile of the steel section was simulated using four-noded shell elements. Four-node tetrahedron, six-node pentahedron and eight-node hexahedron solid elements were used to simulate the loading beams and pedestals. The lateral boundaries of the model were restrained at the loading beams in addition to total fixation at the base of the pedestals. Von-mises failure criterion was used to simulate the behavior of the steel material. Rotation boundary conditions were permitted to enable the corrugated steel plates to rotate and deform freely under applied vertical loading.

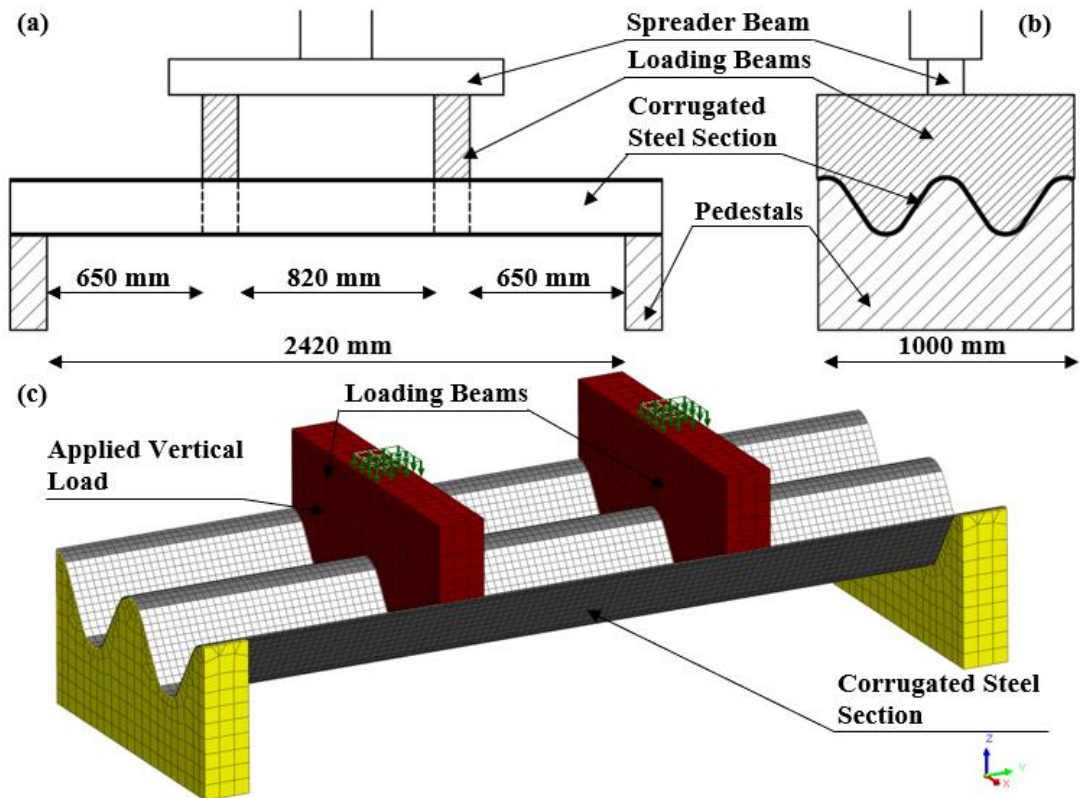


Fig. 6-7: Specimen configuration and test setup (a) front view; (b) side view; (c) three-dimensional numerical model

Fig. 6-8a compares the calculated and measured load-deflection curves at the crest of specimen midspan. The comparison demonstrates that the calculated load-deflection curve reasonably agrees with the observed response. Despite, the large deformations involved and strong nonlinearity the numerical simulation successfully captured the maximum applied vertical load the corrugated steel plates could sustain. The corrugated steel plate reached the maximum flexural capacity during the experiment at applied vertical load of 1430.5 kN. The calculated maximum applied load was 1414.7 kN, i.e., only 1.0% difference between the measured and calculated values.

The maximum bending moment induced in the corrugated steel section was extracted from the numerical model considering the nonlinear distribution of axial stresses as shown in Fig. 6-8b. The maximum calculated bending moment was 438 kN.m/m at the midspan of the specimen. The plastic section modulus of the corrugated steel section ($Z=967.44 \text{ mm}^3/\text{mm}$) was used to calculate the plastic moment capacity (M_p) using Equation (6). The calculated plastic moment capacity (M_p) is 416 kN.m/m. The experimental results indicated that the deepest corrugation profile could sustain bending moment that is 6% above its theoretical plastic moment capacity. Correspondingly, the deepest corrugated profile is considered either class 1 or class 2 where the section can attain plastic moment capacity as per CHBDC (CSA, 2019) and S16-19 (CSA, 2019). Fig. 6-8c shows that the maximum Von mises stresses were found at the midspan of the specimen indicating the formation of plastic hinge, i.e., at the zone of maximum bending moment. The ends of the specimen were deformed upwards as the applied load increased approaching the maximum value. This indicates that the pedestals acted as hinged supports that permitted rotation of the steel section and no rotation restraints existed at the ends.

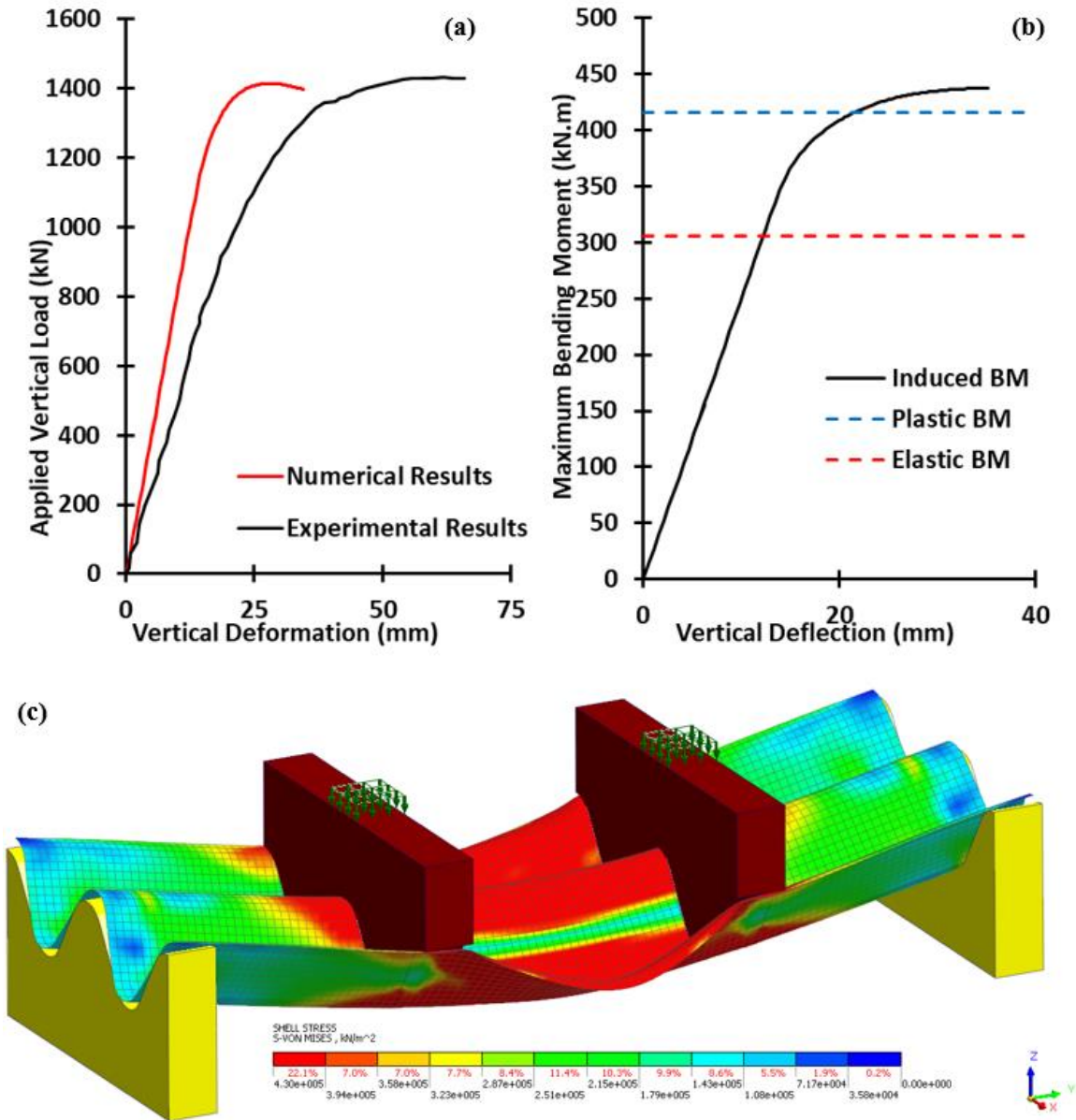


Fig. 6-8: Test results (a) load-deflection curve; (b) moment-deflection curve; (c) Von Mises stresses on deformed shape (scaled up 5 times)

6.3.2 Maximum Backfill Height

Fig. 6-9 presents a three-dimensional FE model for the arched soil-steel structure considering a variable backfill height measured from the base of the steel structure. The numerical model considered backfill construction stages to anticipate the updated configuration occurring at the peaking stage. The vertical deformation of the structure was

recorded between the crown ($X/S=0$) and the point of change in structure radii ($X/S=0.35$). The point of change in structure radii is considered the shoulder of the structure and acts as the connection between the main span (upper zone) and the vertical element of the structure (sides portion).

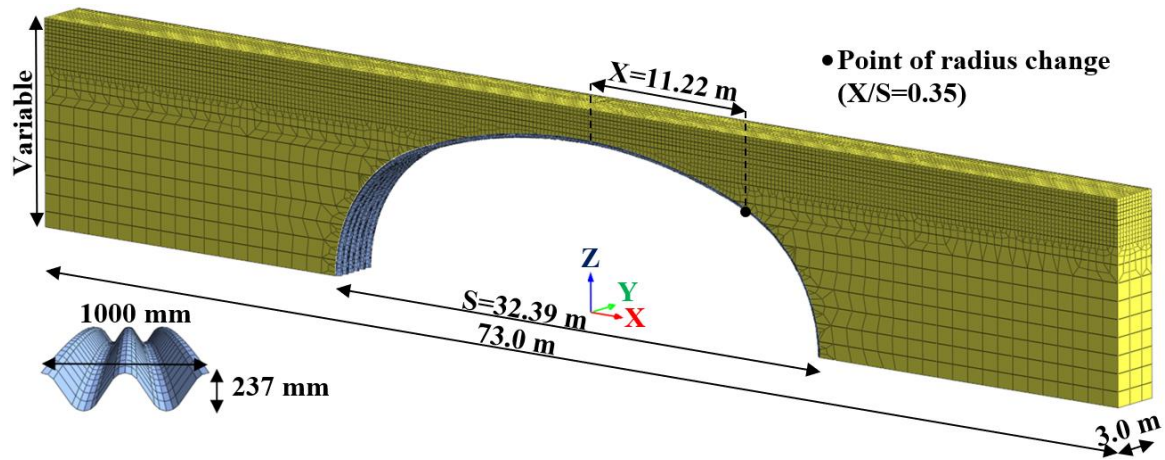


Fig. 6-9: Three-dimensional numerical model under variable backfill height

Fig. 6-10 shows the vertical deformation of the structure at different locations under different backfill heights. The figure shows that the crown ($X/S=0$) exhibited the maximum upward deformation at 9.57 m backfill height (referred to as the peaking stage). This is due to the large lateral stresses applied on the steel structure and without any vertical stresses from soil cover above the crown. After backfill height of 9.57 m is exceeded, the upper zone of the structure starts to deform downward due to increasing the vertical stresses above the structure. The maximum downward deformation in comparison to the undeformed shape occurs at $X/S=0.2$. This is attributed to the crown upward deformation at the peaking stage and the large vertical stiffness of the shoulder and sides of the structure, leading to large downward deformation at the midpoint between them. The maximum difference between the vertical deformations at the crown and midpoint between the crown

and shoulder occurs at the peaking stage. However, this difference decreases as the soil cover height increases indicating increase in the structure radius of curvature and consequently, snap-through buckling mode was encountered due to the spreading of the sides of the structure (Dowswell, 2018). The numerical model predicted a maximum backfill height of 26 meters, at which point the structure fails, and several plastic points develop in the steel structure.

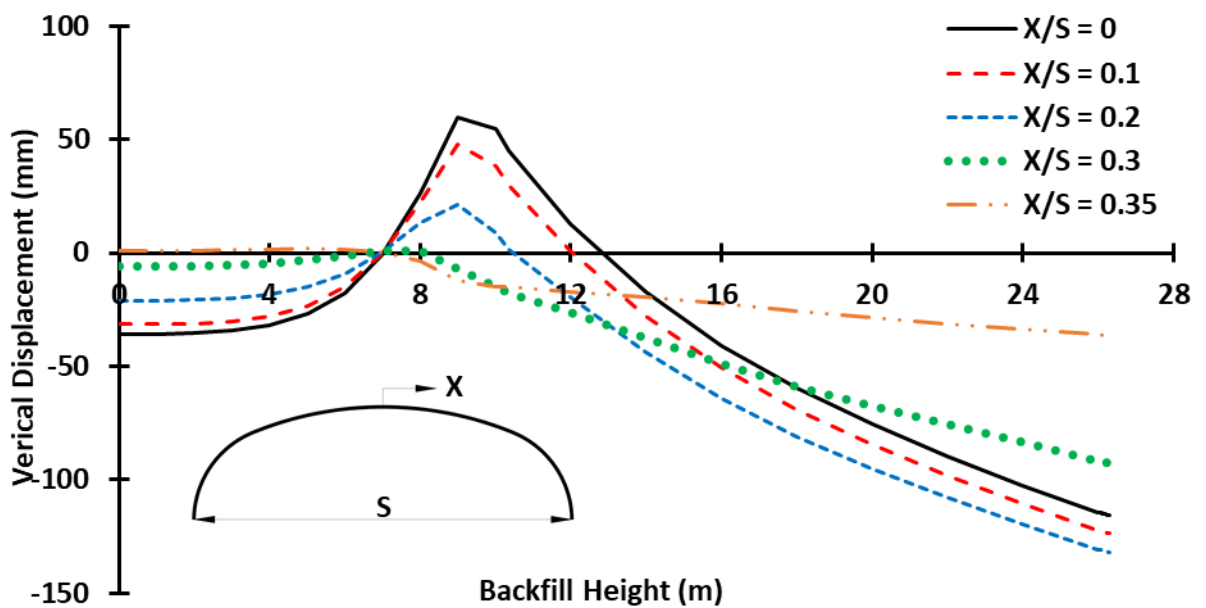


Fig. 6-10: Deflection of soil-steel structure at different backfill heights

Fig. 6-11 shows the distribution of vertical stresses within the soil as well as the distribution of the ratio between the actual vertical pressure on the steel structure to the weight of soil prism above the outside span of the structure, known as Arching Factor (A_f), along the periphery of the structure. The stress distribution close to the steel structure demonstrates the arching effect occurring in the soil. It can be observed that the A_f reaches 3.0 at the point of radius change (i.e., $X/S=0.35$) due to the relatively larger vertical stiffness of the sides of the structure. Based on observations for conventional short-span SSS, the CHBDC

(CSA, 2019) proposes $A_f = 1.0$ for span-to-rise ratio of more than 1.6 (i.e., the case in the current structure). The A_f decreases significantly with distance towards the crown, down to 0.5, due to the large relative vertical deformations between the crown and shoulders of the structure.

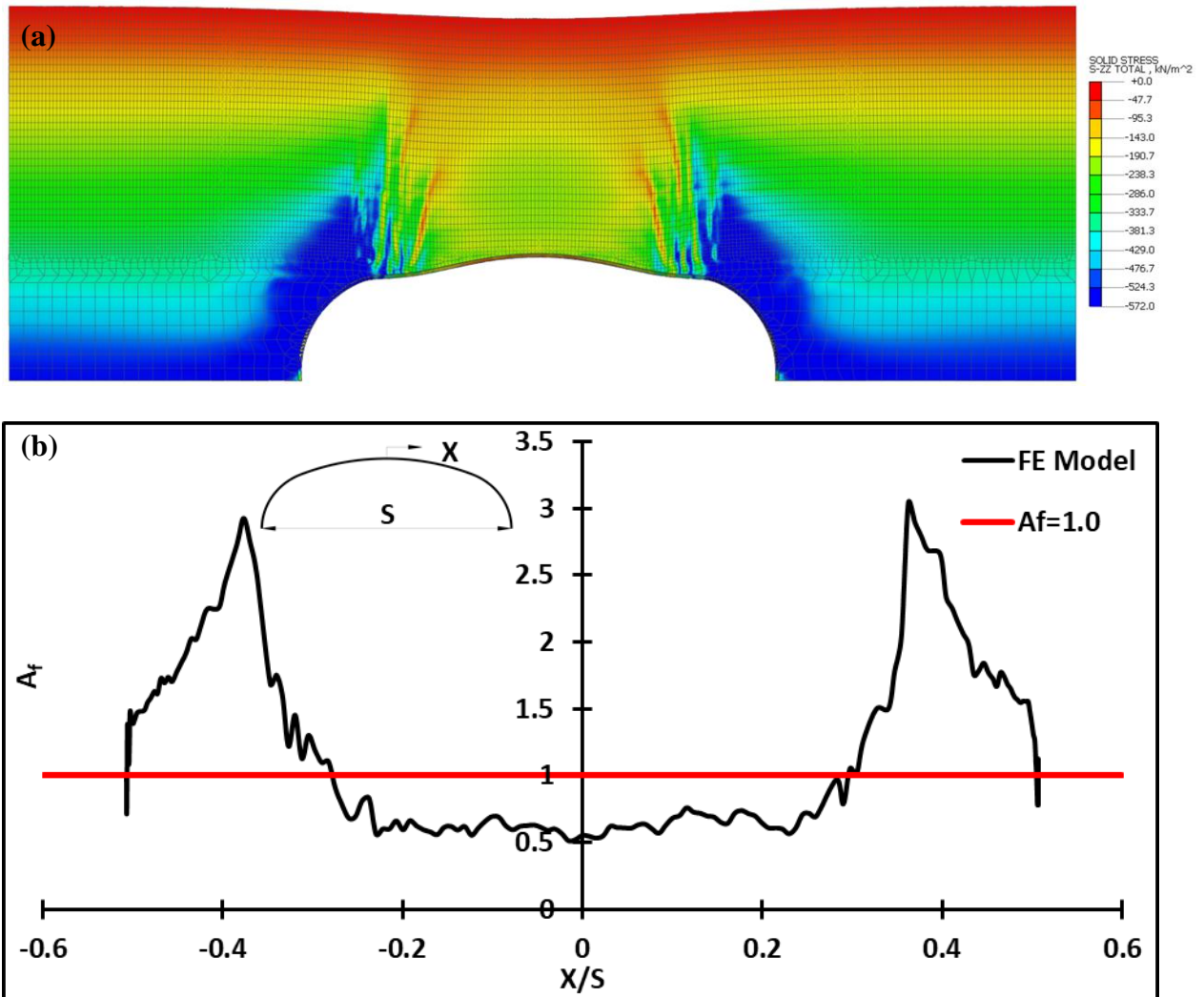


Fig. 6-11: Vertical arching effect on SSS (a) vertical stress distribution in soil; (b) A_f distribution

Fig. 6-12 displays the stress resultants and the deformed shape of the structure scaled up 5 times under the effect of 26.0 m backfill height. Fig. 6-12a shows the locations of yield points developed along the corrugation profile of the steel structure. The stress resultants

presented in Fig. 6-12b and Fig. 6-12c along the periphery of the structure explain the cause for the development of yield points in the steel structure. The sides of the structure reached the yielding stresses (430 MPa) at the valley due to the large induced thrust load, in addition to the outward bending moment. The outward bending moment resulted from the large downward vertical deformation of the crown, accompanied with spreading of the sides and outward rotation of the structure. Consequently, additional compressive stresses are induced at the valley of the sides. Fig. 6-12a also shows the yield points within the zone between the crown and shoulder (i.e. $X/S=0.2$). This zone exhibits the highest downward deformation in the structure in comparison to the undeformed shape leading to the development of inward bending moment, which caused additional compressive stresses at the crest of the corrugated profile that reached the yield strength. The developed yield points at the crest and valley limited the load carrying capacity of the steel structure, i.e., maximum backfill height is reached.

The induced stress resultants in the steel structure are compared to the values obtained from the limit state equation (8) provided by CHBDC (CSA, 2019) and equation (9) by AASHTO (AASHTO LRFD, 2019) for the case of maximum backfill height. The calculated wall compressive strength agreed with the numerical results, which demonstrates that the axial stresses in the steel structure ($\sigma = 402.0 \text{ MPa}$) exceeded wall the compressive strength ($f_b = 324.0 \text{ MPa}$) as per the CHBDC equation. However, the compressive strength according to AASHTO (AASHTO LRFD, 2019) failed to capture the general buckling capacity of the structure giving a ratio of less than 50% between the induced stress and the compressive strength. Moreover, applying the interaction equation

(7) reveals that considering both axial thrust and bending moment account for only 0.935 of the section capacity.

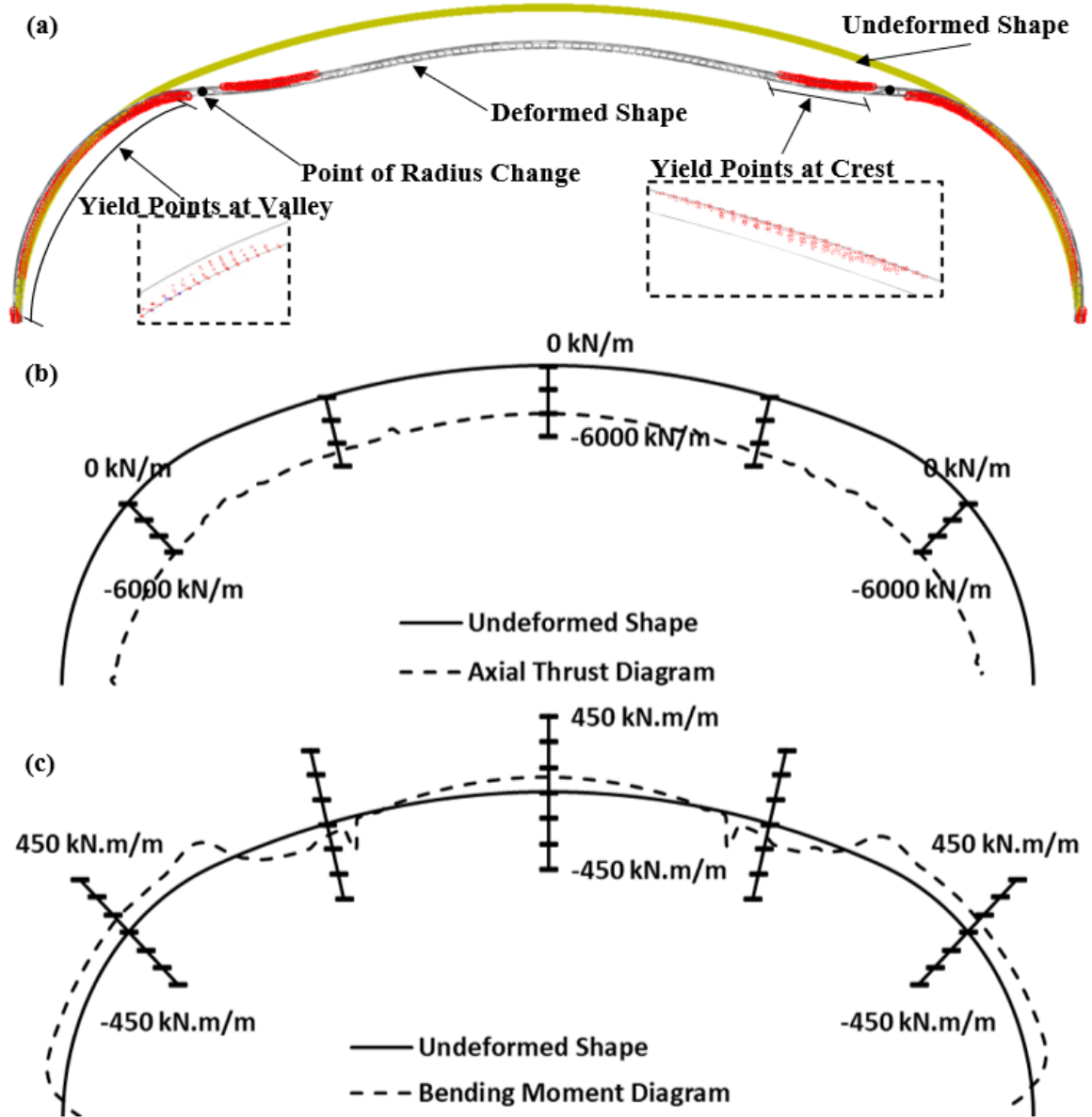


Fig. 6-12: Results from FE model at maximum backfill height; (a) yield points on steel structure; (b) axial thrust diagram; (c) bending moment diagram

6.3.3 Maximum Truck Load

Fig. 6-13 displays the three-dimensional FE model of the SSS subjected to loading configuration of standardized CL-625 truck and Komatsu 980E-5 (Komatsu, 2019). The loading configuration of CL-625 truck was applied at different transverse locations at a distance “X” between the center of axles 2 & 3, and the structure centerline; in addition to applying that of Komatsu 980E-5 rear axle at the structure centerline. Four cases of shallow cover heights are considered in the current analysis to represent the cases of lower induced axial thrust and higher bending moment values: 600 mm; 1000 mm; 1400 mm; and 2000 mm. The footprint of each wheel was considered 0.37 m X 0.95 m as provided in the full-scale test performed on the 10.0 m span SSS. The reason for using the larger footprint was to avoid bearing capacity failure below the loading plates at the ultimate loads and to focus the failure on the steel structure. The truck loads were increased in the numerical model until the structure reaches the ultimate capacity.

The maximum stress resultants induced in the steel structure at the ultimate load were used in the limit state equations provided by CHBDC (CSA, 2019) and equation (9) provided by AASHTO (AASHTO LRFD, 2019). The maximum thrust load along the periphery of the structure is compared to the maximum compressive wall strength using unity resistance and load factors. The equation used in calculating the maximum wall strength based on the CHBDC (CSA, 2019) is for the case of wall radius of curvature greater than equivalent radius relating to elastic behavior of the structure wall, i.e.,

$$f_b = \frac{3\phi_t \sigma F_m E}{\left[\frac{KR}{r}\right]^2} \quad (10)$$

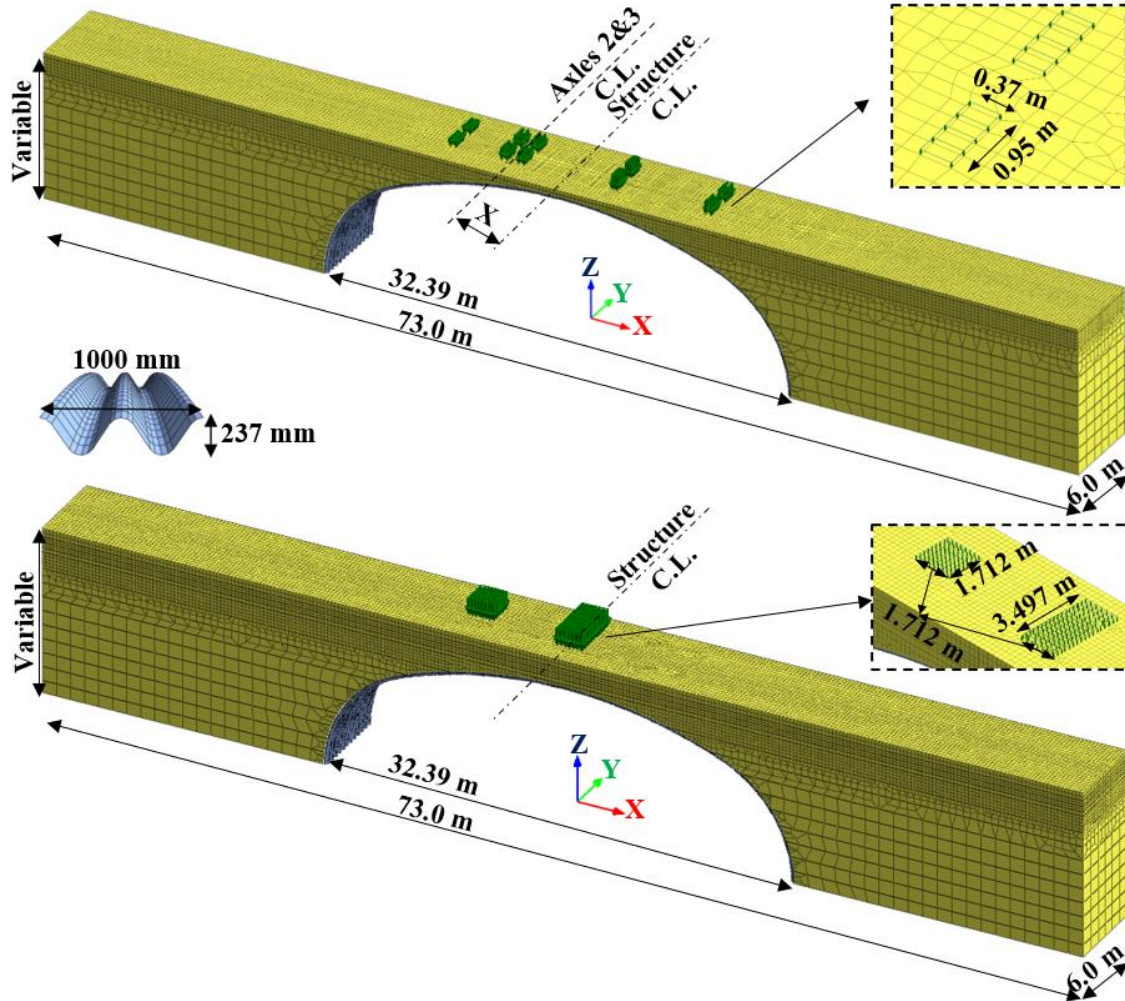


Fig. 6-13: Three-dimensional numerical model subjected to (a) CL-625 truck; (b) Komatsu 980E-5

Fig. 6-14 presents the ratios of axial stress of the steel section and its maximum wall strength obtained from CHBDC and AASHTO equations at different cover heights. Fig. 6-14a demonstrates that applying the ultimate load of CL-625 truck's configuration at transverse distances of -4.0 m; -2.0 m and at the middle of the structure results in axial stresses greater than the maximum compressive wall strength, indicating good agreement between numerical model and CHBDC equation in predicting the structure failure. The loading at these locations produces low bending moment since the structure deforms upwards at these locations during backfilling, which promotes sustaining axial stress higher

than the wall strength. However, applying the load at transverse distance of 2.0 m from the center of the structure causes failure at loads slightly lower than the maximum capacity indicated by the CHBDC (CSA, 2019) equation. Fig. 6-14b indicates that the AASHTO equation is not suitable for predicting the failure in the steel structure for all cases with soil cover height greater than 1.0 m. On the other hand, the AASHTO equation can predict the failure for the cases of truck load applied at transverse distance of -2.0 m and at the center of the structure, and with cover height of 0.6 m. These two loading cases produce axial thrust that exceeds the structure capacity obtained from the AASHTO equation. It can be observed from most of the cases that the combined effects of the axial stresses and induced bending moment that exceeds the flexural capacity of the corrugated profile are the reason of the structure failure.

Fig. 6-15a displays the deformed shape (scaled up by 10 times) of the steel structure under the effect of the maximum CL-625 truck loading configuration that caused failure to the steel structure, at different transverse distances. The deformed shape indicates in-plane instability of the structure due to asymmetric buckling mode. Fig. 6-15a also shows the locations of the second and third axles of the CL-625 truck at each loading condition. It can be observed that the location of second and third axles exhibited the maximum deformations and consequently, maximum bending moment in the structure. It can be observed also that the cases of $X=-4.0$ m and $X=-2.0$ m exhibit inward deformations only in the steel body causing snap-through buckling mode. The reason for that is the presence of axles 4 and 5 above the eastern zone of the structure that prevent the steel body to deform outwards. However, the cases of loading from the middle of the structure to the eastern

side ($X > 0$ m), the structure deforms outwards in the western side where no truck axles exist leading to asymmetric buckling model.

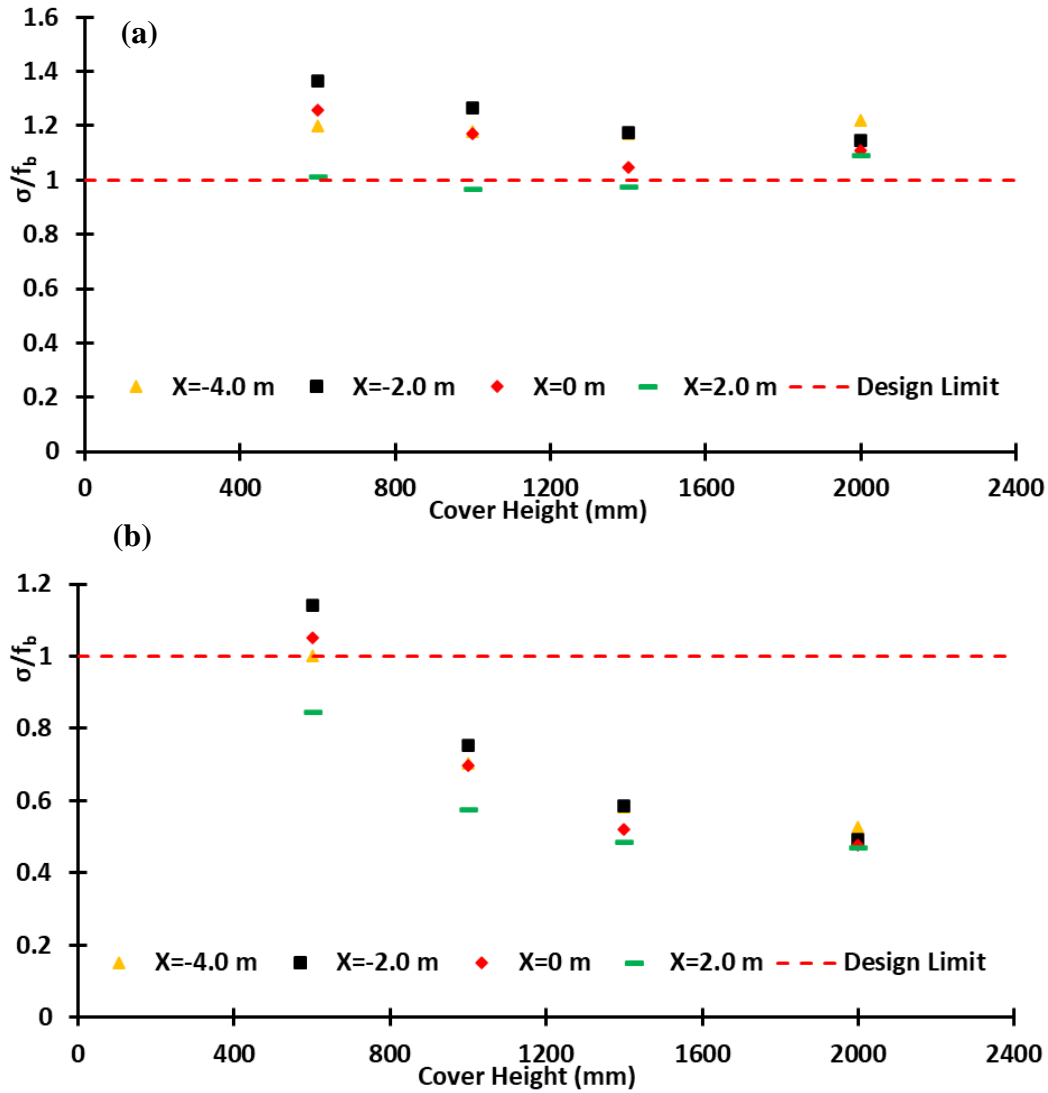


Fig. 6-14: Axial stresses-wall strength ratios at different cover heights (a) CHBDC; (b) AASHTO

Fig. 6-15b displays the interaction equation values of the steel structure under the maximum bending moment values and the corresponding axial stresses at the same cross-section following equation (7). Fig. 6-15b shows that the induced stress resultants at the critical sections of the steel structure at the ultimate case reached nearly 50% only of the maximum capacity of the steel section. Additional numerical models were established

considering steel plates of 8 mm and 10 mm to evaluate the ultimate capacity of structures constructed with thicker plates. However, the steel structure failed to sustain additional applied loads and reached the ultimate capacity. It is noted that the existing interaction equations in the CHBDC and AASHTO do not predict failure in the steel structure based on the induced stress resultants. The interaction diagram demonstrates that the steel structure encounters in-plane buckling behavior under large live loading since the induced-resisting bending moment ratio is close to 1.0.

6.4 Proposed Interaction Equation

This section proposes an interaction equation that incorporates reduction factors of the section capacity due to its buckling. The proposed equation is based on the equations in CHBDC (CSA, 2019) and S16-19 (CSA, 2019). The resisting axial load is reduced by considering the slenderness parameter for the steel member subjected to compression loading. Moreover, the second-order effects of the structure deformations are applied by adding amplification factor to the induced bending moment values. Accordingly, the interaction equation is modified to the following form:

$$\left[\frac{N}{N_r} \right]^2 + \left[\frac{U_{1x}M}{M_r} \right] \leq 1.0 \quad (11)$$

where, N_r & M_r are the factored thrust and moment capacity of the steel section and shall be calculated as:

$$N_r = \phi_s * \sigma_y * A * (1 + \lambda^{2n})^{\frac{-1}{n}} \quad (12)$$

$$\lambda = \frac{KL}{r} \sqrt{\frac{F_y}{\pi^2 E}} \quad (13)$$

$$M_r = \phi_s * Z * \sigma_y \quad (14)$$

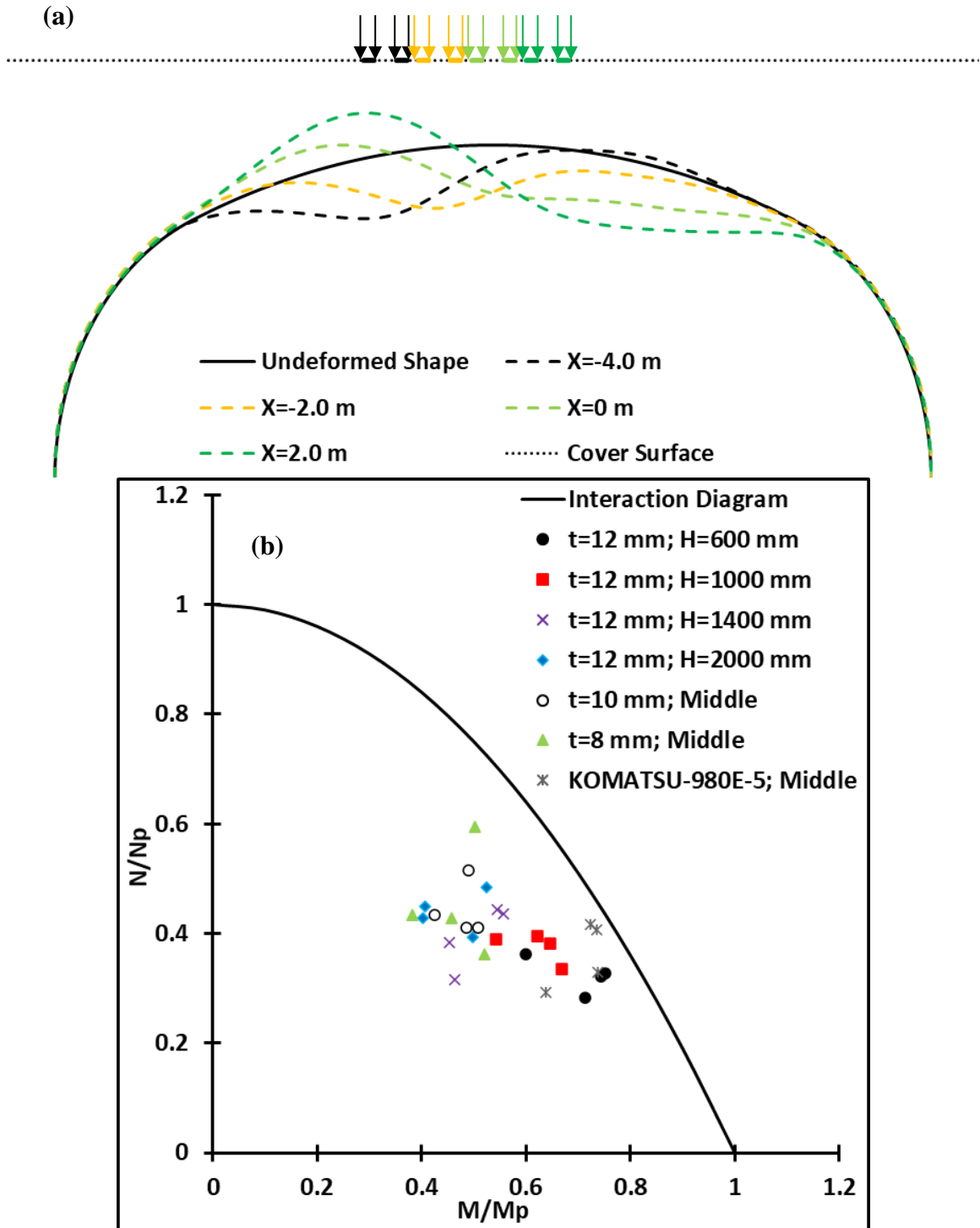


Fig. 6-15: Performance of SSS (a) deformed shape; (b) interaction equation based on CHBDC and AASHTO

ϕ_s is the steel resistance factor; λ is nondimensional slenderness parameter for steel member under compression; n is coefficient for axial buckling resistance (taken as 1.34); K is the effective wall length factor for in-plane buckling (taken as 0.3); L is the arched length of the steel body between points of radius change representing the main span of the structure; r is the radius of gyration of the steel section; and S is the plastic section modulus of the steel section. On the other hand, U_1 is an amplification factor for the second-order effects due to member deformations and can be estimated based on Euler buckling load “ N_e ” as the following:

$$U_1 = \frac{1}{1 - \frac{N}{N_e}} \quad (15)$$

$$N_e = \frac{\pi^2 EA}{\left(\frac{KL}{r}\right)^2} \quad (16)$$

However, it should be noted that the amplification factor U_1 should be used only in the case when geometric nonlinearity due to large deformations is not considered in the numerical simulation.

Fig. 6-16 displays the interaction equation values at the critical sections of the steel structure using the proposed interaction equation. The bending moment amplification factor U_1 was taken as 1.0 since the large deformations were considered in the numerical simulation and the additional bending moment in the steel section due to the nonlinear deformations was already considered in the induced bending moment and thrust values. Fig. 6-16 shows that the maximum bending moment and thrust values in the critical sections along the periphery of the steel structure are beyond the proposed limit state function. This indicates that the proposed interaction equation succeeded to provide limit state covering all the cases of loadings above the soil-steel structure.

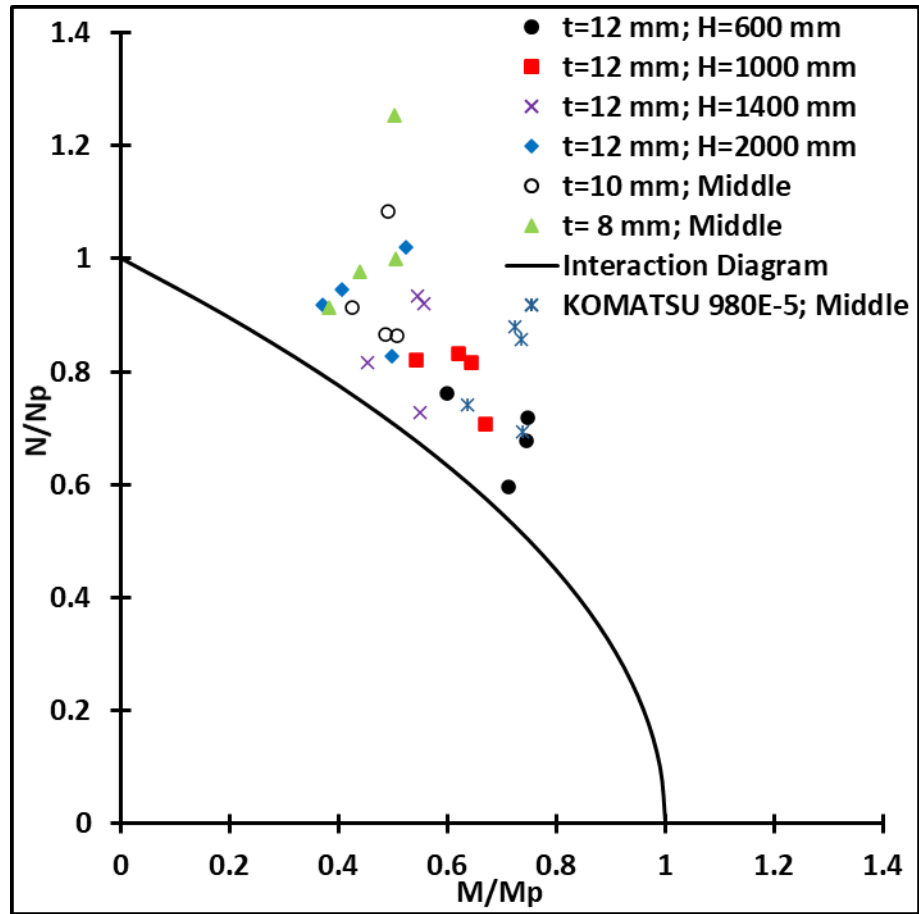


Fig. 6-16: Proposed interaction equation values

6.5 Conclusion

Three-dimensional numerical analysis was conducted on large-span SSS comprising the deepest corrugated steel plates of 500 X 237 mm to investigate their ultimate capacity under earth and truck loading. The numerical analysis was based on 3D nonlinear FE model validated with full-scale test of 10.0 m span SSS using 400 X 150 mm corrugation profile and subjected to service and ultimate loading. The geometric and material nonlinear behavior was included in the numerical simulation in addition to the accumulation of internal forces during construction phases. The following conclusions can be drawn from the current study:

- The axial stress distribution along the corrugated profile under ultimate loading is nonlinear. The nonlinearity increases with the increase of the bending moment.
- The assumption of linear distribution of axial stresses may lead to significant underestimation in the thrust load values affecting the design of steel body.
- The current limit state functions specified in the design codes may sometimes fail to capture the ultimate capacity of the deepest profile large span steel structure when subjected to ultimate earth and truck loading.
- In-plane and snap-through buckling modes may be encountered in large-span SSS due to significant second order effects associated with the axial forces in addition to large deformation in the steel structure leading to induced bending moment exceeding the flexural capacity of the corrugated steel section.
- Modified interaction equation is proposed to account for in-plane structure instability for large-span SSS. The proposed interaction equation can determine the ultimate limit state covering all the SSS and load cases considered in the current study.
- It should be noted that the proposed interaction equation is evaluated for 10.0 m and 32.4 m span SSS only. Further analysis is still required for different soil-steel structure configurations and backfilling conditions.

6.6 References

- AASHTO (American Association of State Highway and Transportation Officials). 2019. AASHTO LRFD Bridge Design Specification, customary U.S. units, 7th Ed. Washington, D.C.: AASHTO
- Allen R. L., J. M. Duncan, and R. T. Snacio. 1988. "An Engineering Manual for Sheet Pile Walls". Blacksburg, VA: Department of Civil Engineering, Virginia Tech.
- ASTM D2487-06. 2006. "Standard Practice for Classification of Soils for Engineering Purposes (Unified Soil Classification System)." ASTM International, West Conshohocken, PA. DOI: 10.1520/D2487-06
- Beben, D. and Z. Manko. 2008. Static load tests of a corrugated steel plate arch with relieving slab. *Journal of Bridge Engineering*. 13(4), 362-376. [https://doi.org/10.1061/\(ASCE\)1084-0702\(2008\)13:4\(362\)](https://doi.org/10.1061/(ASCE)1084-0702(2008)13:4(362))
- CHBDC (Canadian Highway Bridge Design Code). 2019. Canadian Standards Association. CAN/CSA-S6-14., Mississauga, ON.: CHBDC
- CSPI (Corrugated Steel Pipe Institute). 2017. Handbook of Steel Drainage and Highway Construction Products, Canadian Edition, Cambridge, ON.: CSPI.

- Dowswell, B. 2018. “Design Guide 33: Curved member design” American Institute of Steel Construction. USA.
- Embaby, K., H. El Naggar, and M. El Sharnouby. 2021. “Response evaluation of large-span ultra-deep soil-steel bridges to truck loading.” *Int. J. Geomech.*, 21(10). [https://doi.org/10.1061/\(ASCE\)GM.1943-5622.0002159](https://doi.org/10.1061/(ASCE)GM.1943-5622.0002159)
- Embaby, K., H. El Naggar, and M. El Sharnouby. In press. “Performance of large-span arched soil-steel structures under soil loading” *Thin-Walled Structures*
- Flener E. B. 2009. “ Response of long-span box type soil-steel composite structures during ultimate loading tests”. *Journal of Bridge Engineering*. 14(6). 10.1061/(ASCE)BE.1943-5592.0000031
- Komatsu. 2019. Electric drive truck (980E-5). Komatsu America Corp. USA <https://www.smsequipment.com/getmedia/263888a2-175a-472e-a625-2f50909ab898/980E-5.pdf>
- Lefebvre, G., M. Laliberte, L. Lefebvre, Lafleur J. and C. Fisher. 1976. Measurement of soil arching above a large diameter flexible culvert. *Canadian Geotechnical Journal*. 13(1), 58-71. <https://doi.org/10.1139/t76-006>

- Loughheed, A. 2008. "Limit states testing of a buried deep-corrugated large-span box culvert." M.S. thesis. Kingston, ON, Canada : Department of Civil Engineering, Queen's University. <http://hdl.handle.net/1974/1663>
- Mak, A. C., R. W. I. Brachman, I. D. Moore. 2009. "Measured response of a deeply corrugated box culvert to three dimensional surface loads." In Proc., Transportation Research Board Annual Conference, Washington, D.C.: TRB, 09-3016
- Midas. 2020. Midas GTS NX user manual, Midas IT Co. Accessed September 17, 2019. <https://www.midasoft.com/geo/gtsnx/products>
- Pettersson L. 2007. "Full scale tests and structural evaluation of soil steel flexible culverts with low height of cover." Ph.D. thesis, Division of Structural Engineering and Bridges, KTH Royal Institute of Technology.
- Petersoncat. 2013. Hydraulic Shovel (6090 FS). Caterpillar Inc. USA <https://www.petersoncat.com/sites/cat/files/products/documents/18555798.pdf>
- Pettersson L., H. Sundquist. 2014. "Design of soil steel composite bridges." Report 112, 5th Edition. Division of Structural Engineering and Bridges, KTH Royal Institute of Technology.

- Ramadan, S. and M. H. El Naggar. 2021. "Design guidelines for reinforced concrete three-sided culverts." *Tunnelling and Underground Space Technology*. 119. 10.1016/j.tust.2021.104259
- Sanaeiha A., M. Rahimian, M. S. Marefat. 2017. "Field test of a large-span soil-steel bridge stiffened by concrete rings during backfilling" *Journal of Bridge Engineering*. 22(10). [https://doi.org/10.1061/\(ASCE\)BE.1943-5592.0001102](https://doi.org/10.1061/(ASCE)BE.1943-5592.0001102)
- Sargand, S. M., G. A. Hazen, T. Masada. 1994. Long-term field study of a deep-corrugated metal box type culvert. *Canadian Geotechnical Journal*. 31(2), 175-180. <https://doi.org/10.1139/t94-023>
- Tarmac. 2018. "Construction and execution of emirates road at RAK." Project No. R/7078-311906/77/2016. Dubai, UAE
- Wadi A., L. Pettersson, R. Karoumi. 2020. "On predicting the ultimate capacity of a large-span soil-steel composite bridge." *International Journal of Geosynthetics and Ground Engineering*. 6:48. <https://doi.org/10.1007/s40891-020-00232-z>
- Webb, M. C., E. T. Selig, J. A. Sussmann and T. J. McGrath. 1999. Field tests of a large-span metal culvert. Washington, DC: Transportation Research Record: Journal of the Transportation Research Board. 1656(1), 14-24. <https://doi.org/10.3141/1656-03>

- Williams, K., S. Mackinnon and J. Newhook. 2012. New and innovative developments for design and installation of deep corrugated buried flexible steel structures. The 2nd European conference on buried flexible structures. Poznan, Poland

7 Conclusions

7.1 Summary

Soil-steel structures are used nowadays as a solution for overpassing in highway and mining engineering projects. Soil-steel structures are considered in numerous engineering projects as they are cheaper and easy to construct in comparison to conventional concrete and steel bridges. Recently, the deepest corrugation profile has been developed to achieve large spans and have been used for applications encompassing up to 32 meters. Nevertheless, the performance of large-span soil-steel structures and the distribution of soil stresses on the structure surface and the cut plates are yet to be investigated under different loading conditions.

This thesis presents a comprehensive investigation of the world's largest-span soil-steel structure constructed in Dubai, UAE, in 2019 as an example for large span soil-steel structures. It has a span of 32.40 m and vertical rise of 9.57 m. Lateral reinforced steel mesh was attached to the steel structure and embedded in the surrounding backfill. Moreover, the performance of the steel structure was enhanced by cement-stabilized soil at a certain level and reinforced concrete collars at both cut ends of the structure. The structure was fully instrumented and monitored during all construction stages and the performance of the structure was recorded under the effect of soil loading.

Three-dimensional nonlinear finite element modeling technique was used to further investigate the performance of the soil-steel structure and to understand the influence of different construction procedures and stages on the structural integrity of the structure.

Finally, the ultimate capacity of large-span soil-steel structure was investigated under the effect of earth and truck loading. The numerical analysis was used to propose design guidelines for soil-steel structures taking into account several factors.

7.2 Conclusions

Based on the results of our investigation program, the following conclusions can be drawn:

7.2.1 Service loading

7.2.1.1 Earth Loading

- The field monitoring data demonstrated the capability of the deepest corrugation profile to safely support the largest-span arched soil-steel bridge in the world with clear span of 32.40 meters during and by the end of construction under the effect of soil loading. The study shows possible ways of shape controlling, and together with careful design process, it can be possible to provide soil-steel structures withstanding larger-spans.
- Three-dimensional nonlinear numerical model was conducted considering the exact configuration of the corrugated profile. The numerical model simulated all the structural elements used to support the bridge and both material and geometric nonlinearity were considered in the current study. The numerical model successfully captured the performance of the structure during and at the end of construction under the effect of surrounding backfill soil.
- The calculated deformations of the steel structure close to the ends where reinforced concrete collars were attached to the steel structure were in a good agreement with the measured deformations with a difference less than 0.5% of the

total rise of the structure. The validation program demonstrated the ability of the numerical simulation in predicting the performance of the steel structure under the condition of attaching concrete collars and steel mesh reinforcements to the sides of the structure.

- Two main critical zones of the steel structure, the crown and at the change of arc radii (40 degrees from the top arc on each side), were observed to experience high axial stresses that may cause buckling of the cross-section and should be carefully considered in the structural design.
- Based on the assumption of considering no relative deformation permitted between steel mesh reinforcement and surrounding soil, it was found that reinforced steel mesh significantly reduced the deformations and stress resultants in the steel structure during and after construction with nearly 50% reduction in the axial compressive stresses at the peaking phase. Nevertheless, the reduction percentage in the upward vertical deformation decreases by increasing the longitudinal spacing of steel bars and decreasing the embedment length in the backfill soil.
- Circumferential steel stiffeners lessen both upward and downward vertical deformation of steel structure with maximum crown deformation less than 0.5% of the structure rise. The reduced vertical deformation is due to the contribution of circumferential steel stiffeners to resisting downward deformations after adding the soil cover above the structure. An equation is proposed to estimate the percentage reduction in the induced axial stresses in steel structure based on the rigidity of the steel stiffeners.

- The results obtained from the conducted numerical analysis and field measurements showed the validity of using steel mesh reinforcement in rigidifying large-span soil-steel structures. It can be concluded also that steel mesh reinforcement can be utilized around buried structures as an alternative strengthening approach to reduce the induced stress resultants in the steel structure during and after construction.
- The validated modeling approach was employed to evaluate the effect of different beveled end slopes on the deformations, axial stresses and bending moment values of the corrugated steel plates. It was found that the slope of the beveled ends significantly affects the induced stress resultants in the steel structure. However, the circumferential stresses at different transverse cross-sections were not affected by changing the slope of beveled ends.
- The induced longitudinal bending moment increased significantly by increasing the slope of the beveled ends leading to excessive longitudinal stresses in the steel plates and transverse bolted connections. Furthermore, the steel mesh reinforcement and concrete collars reduced the induced circumferential stresses in the steel structure by nearly 30-50%.
- The results obtained from comparing the longitudinal bending moment under different strengthening techniques showed the significance of using concrete collar in reducing the longitudinal bending moment and consequently, controls the design and cost of the beveled ended soil-steel structures.

7.2.1.2 Truck Loading

- The numerical modeling technique for simulating soil-steel structures subjected to truck loading was validated by conducting a three-dimensional nonlinear finite element model for a 10.0 m span box soil-steel structure. The numerical model simulated several single axle and tandem axle loading tests and compared with the measured deformations and axial stresses. The calculated response and stress resultants were in good agreement with the observed experimental results of the full-scale culvert with a maximum difference of 10% and 15% for the measured circumferential bending moments and deformations, respectively.
- The validated modeling approach was employed to evaluate the influence of truck axle loading on the world's largest-span soil-steel structure that was constructed in Dubai, UAE. The results demonstrated the significant effect of the cover height on the stress resultants of the steel structure. The vertical stress distribution for axle loading was evaluated and a ratio of 2V:1H was recommended as an upper bound for analyzing large-span soil-steel bridges subjected to live loading.
- The effect of different modeling techniques on the numerical results due to live loading was investigated. It was found that the geometric nonlinearity could cause an increase of 4% and 8% in axial stresses and deformations, respectively. Furthermore, slippage at soil-structure interface could increase axial stresses by up to 4%.
- The study demonstrated that using the simplified linear elastic-perfectly plastic soil model with Mohr-Coulomb could overestimate the axial stress by up to 60%.

which could significantly affect the total stress resultants of the steel structure. Moreover, lack of consideration of construction stages before applying the live load overestimates the calculated axial stresses and deformations by about 11%.

7.2.2 Ultimate loading

- The numerical modeling technique for simulating soil-steel structures subjected to ultimate loading conditions was validated by conducting a three-dimensional nonlinear finite element model for a 10.0 m span box soil-steel structure. The geometric and material nonlinear behavior was included in the numerical simulation in addition to the accumulation of internal forces during construction phases. It was found that the axial stress distribution along the corrugated profile under ultimate loading is nonlinear. The nonlinearity increases with the increase of the bending moment.
- The numerical analysis indicated that the assumption of linear distribution of axial stresses may lead to significant underestimation in the axial thrust values induced in the steel wall of the structure affecting the design of steel structure.
- The current limit state functions specified in the design codes may sometimes fail to capture the ultimate capacity of the deepest profile large span steel structure when subjected to ultimate earth and truck loading.
- In-plane and snap-through buckling modes may be encountered in large-span soil-steel structures due to significant second order effects associated with the axial

forces in addition to large deformation in the steel structure leading to induced bending moment exceeding the flexural capacity of the corrugated steel section.

- Modified interaction equation is proposed to account for in-plane structure instability for large-span soil-steel structures. The proposed interaction equation can determine the ultimate limit state covering all the SSS and load cases considered in the current study.
- It should be noted that the proposed interaction equation is evaluated for 10.0 m and 32.4 m span soil-steel structures only. Further analysis is still required for different soil-steel structure configurations and backfilling conditions.

7.3 Recommendations for Future Research

The current study demonstrated the capability of the deepest corrugated profile (Ultra-Cor) to withstand large-span soil-steel structures (up to 40.0 m). Several strengthening techniques were demonstrated to enhance the performance of buried steel structures by reducing the deformations and induced stress resultants. The following are recommended for future research work:

- Evaluating the performance of different soil-steel structures configurations under ultimate loading conditions.
- Investigating the influence of circumferential and transverse bolted connections on the performance of soil-steel structures.

- Investigating the local buckling of the straight portion of the Ultra-Cor steel plates using validated 3D numerical model of the large-span soil-steel structure.
- Carry out a reliability analysis based on target reliability indices associated with predetermined probabilities of failure for the various ultimate and serviceability limit states.

Curriculum Vitae

Name: Kareem Embaby

Post-secondary Education and Degrees: Ain Shams University
Cairo, Egypt
2013-2018 M.A.Sc.

Ain Shams University
Cairo, Egypt
2008-2013 B.Sc.

Honors and Awards:

- Mitacs Accelerate internship, 2020-2022
- 407 ETR Scholarship, Transportation Association of Canada, 2021.
- John Booker Award, Geotechnical Research Center, University of Western Ontario, 2021.
- Teaching Assistant Excellence Award Winner, University of Western Ontario, 2020.
- L.G. Soderman Award, Geotechnical Research Center, University of Western Ontario, 2019.

Academic Work Experience

Teaching Assistant
The University of Western Ontario
2018-2022

Teaching Assistant
Ain Shams University
2013-2018

Publications:

- **Embaby K.**, El Naggar H., El Sharnouby M. “Performance of large-span arched soil-steel bridges under soil loading” *Thin-Walled Structures*. Vol. 172 – March 2022
- Ramadan S., El Naggar H., Derbi O., **Embaby K.** “Preliminary Analysis and Instrumentation of Large-Span Three-sided Reinforced Concrete Culverts” *Journal of Bridge Engineering*. Vol. 27, Issue 2 – February 2022
- **Embaby K.**, El Naggar H., El Sharnouby M. “Response Evaluation of Soil-Steel Bridges to Truck Loading” *International Journal of Geomechanics*. Vol. 21, Issue 10 – October 2021.
- Helmy H., Tawfek M., **Embaby K.** “Simulation of Rough Rock Joints under Shear Stress” *International Journal of Engineering Research and Application*. ISSN: 2248-9622, Vol. 8, Issue 7, 2018.
- **Embaby K.**, El Naggar H., El Sharnouby M. Presentation “Three-dimensional Numerical Simulation of Large-Span Soil-Steel Bridges” TAC Conference & Exhibition. 2021